ELECTROMAGNETIC INTERACTION COMPLEXITY REDUCTION USING DEEP LEARNING

A THESIS SUBMITTED TO
THE GRADUATE SCHOOL OF NATURAL AND APPLIED SCIENCES
OF
MIDDLE EAST TECHNICAL UNIVERSITY

BY

BARIŞCAN KARAOSMANOĞLU

IN PARTIAL FULFILLMENT OF THE REQUIREMENTS
FOR
THE DEGREE OF DOCTOR OF PHILOSOPHY
IN
ELECTRICAL AND ELECTRONICS ENGINEERING

DECEMBER 2019

Approval of the thesis:

ELECTROMAGNETIC INTERACTION COMPLEXITY REDUCTION USING DEEP LEARNING

submitted by **BARIŞCAN KARAOSMANOĞLU** in partial fulfillment of the requirements for the degree of **Doctor of Philosophy in Electrical and Electronics Engineering Department, Middle East Technical University** by,

Prof. Dr. Halil Kalıpçılar
Dean, Graduate School of **Natural and Applied Sciences** _____

Prof. Dr. İlkay Ulusoy
Head of Department, **Electrical and Electronics Engineering** _____

Assoc. Prof. Dr. Özgür Ergül
Supervisor, **Electrical and Electronics Engineering, METU** _____

Examining Committee Members:

Prof. Dr. Sencer Koç
Electrical and Electronics Engineering, METU _____

Assoc. Prof. Dr. Özgür Ergül
Electrical and Electronics Engineering, METU _____

Prof. Dr. Özlem Aydın Çivi
Electrical and Electronics Engineering, METU _____

Prof. Dr. Vakur Behçet Ertürk
Electrical and Electronics Engineering, Bilkent University _____

Assoc. Prof. Dr. Fatih Dikmen
Electronics Engineering, Gebze Technical University _____

Date:

I hereby declare that all information in this document has been obtained and presented in accordance with academic rules and ethical conduct. I also declare that, as required by these rules and conduct, I have fully cited and referenced all material and results that are not original to this work.

Name, Surname: Barışcan Karaosmanoğlu

Signature :

ABSTRACT

ELECTROMAGNETIC INTERACTION COMPLEXITY REDUCTION USING DEEP LEARNING

Karaosmanoğlu, Barışcan
Ph.D., Department of Electrical and Electronics Engineering
Supervisor: Assoc. Prof. Dr. Özgür Ergül

December 2019, 125 pages

In this thesis, we present a novel approach to accelerate electromagnetic simulations by the multilevel fast multipole algorithm (MLFMA). The strategy is based on a progressive elimination of electromagnetic interactions, resulting in trimmed tree structures, during iterative solutions. To systematically perform such eliminations, artificial neural network (ANN) models are constructed and trained to estimate errors in updated surface current coefficients. These column eliminations are supported by straightforward row eliminations, leading to increasingly sparse tree structures and matrix equations as iterations continue. We show that the proposed implementation, namely trimmed MLFMA (T-MLFMA), leads to significantly accelerated electromagnetic simulations of large-scale objects, while the accuracy is still much better than the high-frequency techniques. T-MLFMA can be seen as an exemplar of implementations, where machine learning is successfully integrated into an electromagnetic solver for enhanced simulations.

Keywords: Integral equations, machine learning, multilevel fast multipole algorithm (MLFMA)

ÖZ

ELEKTROMANYETİK ETKİLEŞİM KARMAŞIKLIĞININ DERİN ÖĞRENİM KULLANARAK DÜŞÜRÜLMESİ

Karaosmanoğlu, Barışcan
Doktora, Elektrik ve Elektronik Mühendisliği Bölümü
Tez Yöneticisi: Doç. Dr. Özgür Ergül

Aralık 2019, 125 sayfa

Bu tezde, çok seviyeli hızlı çokkutup yöntemi (ÇSHÇY) ile gerçekleştirilen elektromanyetik benzetimlerin hızlandırılması amacıyla yeni bir yaklaşım sunulmuştur. Strateji, iteratif çözümler esnasında elektromanyetik etkileşimlerin aşamalı olarak elenmesine ve kırpılmış ağaç yapılarının oluşturulmasına dayalıdır. Bu tür elemeleri sistematik olarak gerçekleştirmek için, yapay sinir ağı (YSA) modelleri güncellenen yüzey akım katsayılarındaki hataları tahmin etmek için oluşturulmuş ve eğitilmiştir. Bununla ilgili sütun elemelerinin doğrudan satır elemeleri ile de desteklenmesiyle, iterasyonlar devam ettikçe artan seyreklikteki ağaç yapıları ve matris denklemleri elde edilmiştir. Önerilen kırpılmış ÇSHÇY (K-ÇSHÇY) adındaki uygulamanın, büyük ölçekli nesnelerin elektromanyetik simulasyonlarını önemli ölçüde hızlandırdığı, yüksek frekans tekniklerinden de çok daha doğru olduğu gösterilmiştir. K-ÇSHÇY, iyileştirilmiş benzetimler için makine öğreniminin elektromanyetik çözücülere başarılı bir şekilde entegre edildiği bir örnek uygulama olarak görülebilir.

Anahtar Kelimeler: İntegral denklemleri, makine öğrenimi, çok seviyeli hızlı çokkutup yöntemi (ÇSHCY)

To my wife and my brother

ACKNOWLEDGMENTS

Firstly, I would like to express my most profound appreciation to my supervisor, Assoc. Prof. Dr. Özgür Ergül for his invaluable guidance and support during my Ph.D. studies. I am a conscientious scientist, thanks to his assistance and mentorship.

I would like to thank Prof. Dr. Özlem Aydın Çivi and Prof. Dr. Vakur Ertürk for contributing to the quality of my thesis by providing invaluable suggestions. Their constructive and supportive feedbacks have further motivated me to become a determined researcher.

I also would like to thank Prof. Dr. Sencer Koç and Assoc. Prof. Dr. Fatih Dikmen for their participation in the jury and valuable comments.

I want to thank former and current researchers of computational electromagnetics group in Middle East Technical University (CEMMETU), especially to Zeina El Ahdab, Sadri Güler, Hande İbili, Göktuğ Işıklar, Gökhan Karaova, and Özgür Eriş; there are no words to describe their patience and support during my journey from a student to a leader.

I would like to express my deepest gratitude to my beloved wife, my brother, and my parents for encouraging my studies, to my grandmother for continually believing in me, and to Şenay Kurt for giving me that one chance.

Finally, I would like to thank YÖK for the 100/2000 Ph.D. scholarship program for supporting the writing process of this thesis.

TABLE OF CONTENTS

LIST OF TABLES

TABLES

LIST OF FIGURES

FIGURES

LIST OF ABBREVIATIONS

AD	Approximate diagonalization
AMLFMA	Approximate multilevel fast multipole algorithm
ANN	Artificial neural network
BiCGStab	Biconjugate gradient stabilized method
BFEP	Basis function error predictor
CFIE	Combined-field integral equation
CNN	Convolutional neural network
EFIE	Electric-field integral equation
FGMRES	Flexible generalized minimal residual method
FMM	Fast multipole method
GMRES	Generalized minimal residual method
HRE	High residual error
LRE	Low residual error
MAE	Mean absolute error
MCTF	Modified combined tangential formulation
MFIE	Magnetic-field integral equation
ML	Machine learning
MLFMA	Multilevel fast multipole algorithm
MPA	Mixed precision arithmetics
MOM	Method of moments
MVM	Matrix-vector multiplication
SRR	Split-ring resonator
PEC	Perfect electric conductor
PO	Physical optics

ReLU	Rectified linear unit
RWG	Rao-Wilton-Glisson
TFEC	Testing function error calculator
T-MLFMA	Trimmed multilevel fast multipole algorithm

CHAPTER 1

INTRODUCTION

Accurate and efficient methods to solve electromagnetic radiation and scattering problems have extensively been investigated for many years. Among alternatives, the multilevel fast multipole algorithm (MLFMA) [1, 2] is a well-known method to accelerate electromagnetic analysis based on integral equations. Direct computations of electromagnetic interactions in the method of moments (MOM) lead to a large computational burden due to the per-iteration complexity of $\mathcal{O}(N^2)$ for N discretization elements. MLFMA, on the other hand, calculates the interactions in a grouped manner so that this computational complexity can be reduced to $\mathcal{O}(N \log N)$ both in terms of processing time and memory. Its efficiency makes MLFMA a favorable method to perform matrix-vector multiplications (MVM) in iterative solutions of electromagnetic problems. At the same time, iteration counts required for solutions must also be kept at low levels to reach efficient simulations. In this context, selection of the underlying integral-equation formulation is known to have significant impacts on iterative convergence. For example, in the case of perfect electric conductors (PECs), the combined-field integral equation (CFIE) [3] is often preferred to the electric-field integral equation (EFIE) and the magnetic-field integral equation (MFIE), wherever possible (e.g., for closed conductors), although it provides less accurate results in comparison to EFIE with classical discretization schemes [4–7]. However, even when CFIE is used, iteration counts for large-scale problems can be excessively large so that preconditioning techniques [8–10] become inevitable. Recently, parallelization techniques have also been commonly practiced to further accelerate electromagnetic simulations. For MLFMA, an efficient parallelization requires advanced partitioning schemes based on hierarchical strategies [11–13] that can lead to scalable solutions on hundreds of cores.

Despite all efforts, some of which are briefly summarized above, electromagnetic simulations still need to be accelerated to meet challenging requirements in practical applications. While diverse high-frequency techniques are available in the literature, their limited accuracy often makes them impractical in many applications. Therefore, novel strategies are needed to accelerate available methods with minimum losses in their accuracy. In this thesis, we present a new technique based on systematic modifications of tree structures in MLFMA solutions. Specifically, we introduce trimmed tree structures that are obtained by sparsifying full tree structures during iterative solutions carried out via MLFMA. The trimming operations need to be performed carefully to detect and eliminate unnecessary interactions. For this purpose, we employ machine learning (ML), which has recently become popular in the literature thanks to the unique computational opportunities provided by this approach.

Artificial neural networks (ANNs) and their convolutional forms, i.e., convolutional neural networks (CNNs) [14], have been studied for many years in the context of regression and classification applications, especially in the computer-vision area [15, 16]. Recently, researches in electromagnetics, including numerical studies, have also started to benefit from ML techniques. In general, data processes required by electromagnetic simulations can be accelerated by ML techniques, while pre-processing and post-processing stages can be enhanced. As particular examples, such techniques have been used for antenna design and optimization [17,18], visual estimation of scattering solutions [19], and source reconstruction in inverse scattering problems [20]. ML techniques have also been used to accelerate simulations [21], as well as to enhance direct solutions of magnetic problems [22]. In all these works, however, ML techniques are employed as specialized tools and they are not fully integrated into electromagnetic solvers to make them efficient for simulations of arbitrary geometries.

In the main part of this work, as briefly mentioned above, we present a novel approach to accelerate large-scale electromagnetic simulations via MLFMA by systematically trimming tree structures during iterative solutions. For this purpose, ML techniques are fully integrated into the MLFMA solver for rigorous estimations of converged coefficients. Specifically, during an iterative solution, the convergence of the equivalent surface current is examined by an ANN, which decides unneeded interactions

and trims the MLFMA tree structure as the iterations continue. As the tree structure is progressively sparsified, the processing time per iteration decreases, while the iterative convergence is also accelerated. Hence, a remarkable speedup is achieved in comparison to the full MLFMA, with limited deterioration in the accuracy as opposed to high-frequency techniques.

As a separate part of this thesis, we present another application of ML techniques in large-scale electromagnetic simulations of three-dimensional objects [19]. Simulations of electrically large geometries require long solution durations, while meaningful visual results may be obtained at the early stages of a simulation if the available information is intelligently used. Inspired by the ML-aided super-resolution applications, we present CNN structures that can provide visual estimations of accurate solutions, which cannot be obtained otherwise, using approximate and coarse simulations.

Finally, we also present a novel approach of using deep residual CNN structures to predict electromagnetic scattering error levels in iterative solutions of large-scale objects [23]. A CNN structure is trained by using surface current images to predict the error level in the forward scattering. Hence, by using the predicted error in the forward scattering, one can define alternative convergence criteria.

The chapters in this thesis are organized as follows. In Chapter 2, we present surface integral equations for the PEC objects starting from Maxwell's equations. Then, we briefly show the conversion of the physical problem into a mathematical problem by using MOM. The following part briefly explains the addition theorem and the stages of MLFMA. In Chapter 3, we present the trimming scheme and the implementation of the trimmed MLFMA (T-MLFMA). We show the sparsification of MOM matrices and explain the basis and testing function trimming operations in detail. Then, we show the stages of the basis function trimming using ML, starting from generating datasets to training ML models. In Chapter 4, we present various numerical results obtained with the developed T-MLFMA implementations. We start with proof-of-concept simulations and then present various simulations for the performance of T-MLFMA. In Chapter 5, we show the other applications of ML for electromagnetic simulations. Finally, in Chapter 6, we summarize the thesis and provide our conclud-

ing remarks.

CHAPTER 2

SOLUTIONS OF ELECTROMAGNETICS PROBLEMS USING SURFACE INTEGRAL EQUATIONS

2.1 Surface Integral Equations

Maxwell's equations for simple (linear, isotropic, and homogeneous) media and time-harmonic sources (with $\exp(-i\omega t)$ time dependence) can be written in the frequency domain as

$$\nabla \times \boldsymbol{E}(\boldsymbol{r}) = i\omega\mu \boldsymbol{H}(\boldsymbol{r}) \tag{2.1}$$

$$\nabla \times \boldsymbol{H}(\boldsymbol{r}) = -i\omega\epsilon \boldsymbol{E}(\boldsymbol{r}) + \boldsymbol{J}(\boldsymbol{r}) \tag{2.2}$$

$$\nabla \cdot \boldsymbol{E}(\boldsymbol{r}) = \frac{1}{\epsilon}\rho_e(\boldsymbol{r}) \tag{2.3}$$

$$\nabla \cdot \boldsymbol{H}(\boldsymbol{r}) = 0, \tag{2.4}$$

where ω is the angular frequency ($\omega = 2\pi f$), and ϵ and μ represent the permittivity and the permeability (magnetic permittivity). In the above, $\boldsymbol{E}$ and $\boldsymbol{H}$ are the electric and magnetic field intensities, while $\boldsymbol{J}$ and ρ_e are the electric current density and the electric charge density, respectively, which are related to each other via the continuity equation as

$$\nabla \cdot \boldsymbol{J}(\boldsymbol{r}) = i\omega\rho_e. \tag{2.5}$$

In all these expressions, time-harmonic fields and sources depend on the position $\boldsymbol{r} = x\hat{\boldsymbol{x}} + y\hat{\boldsymbol{y}} + z\hat{\boldsymbol{z}}$. The equivalence principle on general (penetrable and impenetrable) objects requires both electric and magnetic sources. In this thesis, we consider only PECs, which require only electric sources.

The Helmholtz equation for the electric field can be obtained directly by evaluating

the curl of Equation (2.1) and using Equations (2.2) and (2.3) with the identity

$$\nabla \times \nabla \times \boldsymbol{f}_v = \nabla\nabla \cdot \boldsymbol{f}_v - \nabla^2 \boldsymbol{f}_v, \tag{2.6}$$

which gives

$$\nabla \times \nabla \times \boldsymbol{E}(\boldsymbol{r}) = i\omega\mu \nabla \times \boldsymbol{H}(\boldsymbol{r}) \tag{2.7}$$

$$\nabla\nabla \cdot \boldsymbol{E}(\boldsymbol{r}) - \nabla^2 \boldsymbol{E}(\boldsymbol{r}) = i\omega\mu\big(- i\omega\epsilon \boldsymbol{E}(\boldsymbol{r}) + \boldsymbol{J}(\boldsymbol{r})\big) \tag{2.8}$$

$$\frac{1}{\epsilon}\nabla\rho_e(\boldsymbol{r}) - \nabla^2 \boldsymbol{E}(\boldsymbol{r}) = \omega^2\mu\epsilon \boldsymbol{E}(\boldsymbol{r}) + i\omega\mu \boldsymbol{J}(\boldsymbol{r}) \tag{2.9}$$

$$\nabla^2 \boldsymbol{E}(\boldsymbol{r}) + k^2 \boldsymbol{E}(\boldsymbol{r}) = -i\omega\mu \boldsymbol{J}(\boldsymbol{r}) + \frac{1}{\epsilon}\nabla\rho_e(\boldsymbol{r}), \tag{2.10}$$

where $k = \omega\sqrt{\mu\epsilon}$ is the wavenumber. Similarly, we evaluate the curl of Equation (2.2) and use Equations (2.1) and (2.4) to obtain the Helmholtz equation for the magnetic field as

$$\nabla \times \nabla \times \boldsymbol{H}(\boldsymbol{r}) = -i\omega\epsilon \nabla \times \boldsymbol{E}(\boldsymbol{r}) + \nabla \times \boldsymbol{J}(\boldsymbol{r}) \tag{2.11}$$

$$\nabla\nabla \cdot \boldsymbol{H}(\boldsymbol{r}) - \nabla^2 \boldsymbol{H}(\boldsymbol{r}) = -i\omega\epsilon\big(i\omega\mu \boldsymbol{H}(\boldsymbol{r})\big) + \nabla \times \boldsymbol{J}(\boldsymbol{r}) \tag{2.12}$$

$$-\nabla^2 \boldsymbol{H}(\boldsymbol{r}) = +\omega^2\mu\epsilon \boldsymbol{H}(\boldsymbol{r}) + \nabla \times \boldsymbol{J}(\boldsymbol{r}) \tag{2.13}$$

$$\nabla^2 \boldsymbol{H}(\boldsymbol{r}) + k^2 \boldsymbol{H}(\boldsymbol{r}) = -\nabla \times \boldsymbol{J}(\boldsymbol{r}). \tag{2.14}$$

The electric and magnetic fields can be written in terms of vector and scalar potentials as

$$\boldsymbol{E}(\boldsymbol{r}) = i\omega \boldsymbol{A}_m(\boldsymbol{r}) - \nabla\phi_e(\boldsymbol{r}) \tag{2.15}$$

$$\boldsymbol{H}(\boldsymbol{r}) = \frac{1}{\mu}\nabla \times \boldsymbol{A}_m(\boldsymbol{r}), \tag{2.16}$$

where $\boldsymbol{A}_m$ is the magnetic vector potential and ϕ_e is the electric scalar potential. By applying the Lorentz gauge

$$\nabla \cdot \boldsymbol{A}_m(\boldsymbol{r}) = i\omega\epsilon\mu\phi_e(\boldsymbol{r}), \tag{2.17}$$

Helmholtz equations for the potentials can be obtained, which can be written as

$$\nabla^2\phi_e(\boldsymbol{r}) + k^2\phi_e(\boldsymbol{r}) = -\frac{1}{\epsilon}\rho_e(\boldsymbol{r}) \tag{2.18}$$

$$\nabla^2 \boldsymbol{A}_m(\boldsymbol{r}) + k^2 \boldsymbol{A}_m(\boldsymbol{r}) = -\mu \boldsymbol{J}(\boldsymbol{r}). \tag{2.19}$$

The point-source response of Equations (2.18) and (2.19), i.e., the free-space Green's function, can be written as

$$g(\boldsymbol{r}, \boldsymbol{r}') = \frac{\exp(ik|\boldsymbol{r} - \boldsymbol{r}'|)}{4\pi|\boldsymbol{r} - \boldsymbol{r}'|}, \tag{2.20}$$

where $\boldsymbol{r}$ is the observation point and $\boldsymbol{r}'$ is the source point. The Helmholtz equations in (2.18) and (2.19) can be solved for arbitrary electric current and charge densities by using the homogeneous-space Green's function. The expression for ϕ_e and $\boldsymbol{A}_m$ for arbitrary sources can be written as

$$\phi_e(\boldsymbol{r}) = \frac{1}{\epsilon} \int d\boldsymbol{r}' g(\boldsymbol{r}, \boldsymbol{r}') \rho_e(\boldsymbol{r}') \tag{2.21}$$

$$\boldsymbol{A}_m(\boldsymbol{r}) = \mu \int d\boldsymbol{r}' g(\boldsymbol{r}, \boldsymbol{r}') \boldsymbol{J}(\boldsymbol{r}'). \tag{2.22}$$

Inserting (2.21) and (2.22) into (2.15) and (2.16) gives the electric field and the magnetic field in terms of the electric current and charge densities as

$$\boldsymbol{E}(\boldsymbol{r}) = ik\eta \int d\boldsymbol{r}' \Big(\boldsymbol{J}(\boldsymbol{r}') + \frac{1}{k^2} \nabla' \cdot \boldsymbol{J}(\boldsymbol{r}') \nabla \Big) g(\boldsymbol{r}, \boldsymbol{r}') \tag{2.23}$$

$$\boldsymbol{H}(\boldsymbol{r}) = \int d\boldsymbol{r}' \nabla g(\boldsymbol{r}, \boldsymbol{r}') \times \boldsymbol{J}(\boldsymbol{r}'), \tag{2.24}$$

where $\eta = \sqrt{\dfrac{\mu}{\epsilon}}$ is the intrinsic impedance of the medium. The electric and magnetic fields can be expressed in terms of integro-differential operators as

$$\boldsymbol{E}(\boldsymbol{r}) = \eta \boldsymbol{\mathcal{T}}\{\boldsymbol{J}\}(\boldsymbol{r}) \tag{2.25}$$

$$\boldsymbol{H}(\boldsymbol{r}) = \boldsymbol{\mathcal{K}}\{\boldsymbol{J}\}(\boldsymbol{r}), \tag{2.26}$$

where

$$\boldsymbol{\mathcal{T}}\{\boldsymbol{X}\}(\boldsymbol{r}) = ik \int d\boldsymbol{r}' \Big(\boldsymbol{X}(\boldsymbol{r}') + \frac{1}{k^2} \nabla' \cdot \boldsymbol{X}(\boldsymbol{r}') \nabla \Big) g(\boldsymbol{r}, \boldsymbol{r}') \tag{2.27}$$

$$\boldsymbol{\mathcal{K}}\{\boldsymbol{X}\}(\boldsymbol{r}) = \int d\boldsymbol{r}' \boldsymbol{X}(\boldsymbol{r}') \times \nabla' g(\boldsymbol{r}, \boldsymbol{r}'). \tag{2.28}$$

The electromagnetics problems involving three-dimensional PEC objects can be formulated by using the equivalence principle, as shown in Figure 2.1. In the equivalent problem, the objects are represented by virtual surfaces and equivalent electric surface current densities, which lead to zero total electromagnetic fields inside the virtual surfaces. The outer region of the virtual surfaces is an unbounded free space, and nonzero electromagnetic fields occur due to incoming and scattered fields. Con-

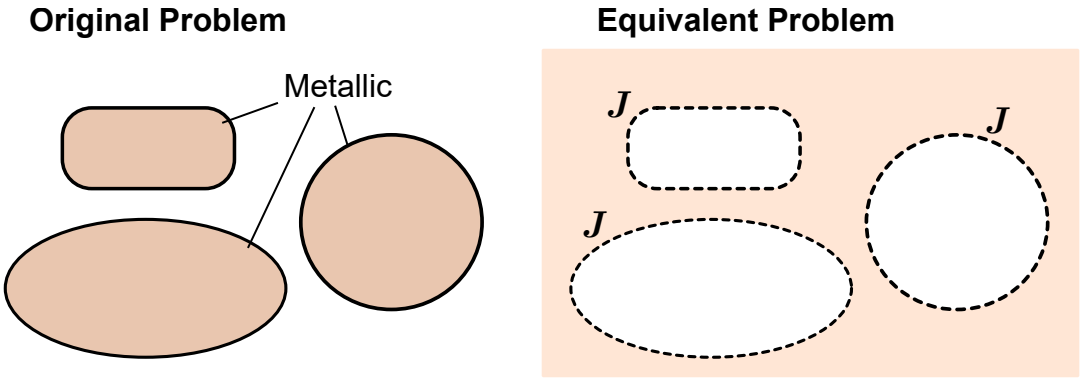

Figure 2.1: Applying the equivalence theorem to an electromagnetics problem involving metallic objects.

sider a metallic region D bounded by a surface S as shown in Figure 2.2, where $\hat{\boldsymbol{n}}$ represents the outward surface normal direction. The equivalent electric surface currents are related to the tangential components of the electric and magnetic fields at the boundary as

$$\boldsymbol{J}(\boldsymbol{r}) = \hat{\boldsymbol{n}} \times \boldsymbol{H}(\boldsymbol{r}) \tag{2.29}$$

$$-\boldsymbol{M}(\boldsymbol{r}) = \hat{\boldsymbol{n}} \times \boldsymbol{E}(\boldsymbol{r}) = 0. \tag{2.30}$$

The scattered electric and magnetic fields due to $\boldsymbol{J}(\boldsymbol{r})$ can be calculated by using (2.25) and (2.26). Using the integro-differential operators, we obtain

$$\hat{\boldsymbol{n}} \times \boldsymbol{H}^{sca}(\boldsymbol{r}) + \hat{\boldsymbol{n}} \times \boldsymbol{H}^{inc}(\boldsymbol{r}) = \boldsymbol{J}(\boldsymbol{r}) \tag{2.31}$$

$$\hat{\boldsymbol{n}} \times \mathcal{K}\{\boldsymbol{J}\}(\boldsymbol{r}) + \hat{\boldsymbol{n}} \times \boldsymbol{H}^{inc}(\boldsymbol{r}) = \boldsymbol{J}(\boldsymbol{r}) \tag{2.32}$$

$$\hat{\boldsymbol{n}} \times \boldsymbol{E}^{sca}(\boldsymbol{r}) + \hat{\boldsymbol{n}} \times \boldsymbol{E}^{inc}(\boldsymbol{r}) = 0 \tag{2.33}$$

$$\eta\hat{\boldsymbol{n}} \times \mathcal{T}\{\boldsymbol{J}\}(\boldsymbol{r}) + \hat{\boldsymbol{n}} \times \boldsymbol{E}^{inc}(\boldsymbol{r}) = 0, \tag{2.34}$$

where $\boldsymbol{H}^{sca}$ and $\boldsymbol{H}^{inc}$ are incident and scattered magnetic fields, while $\boldsymbol{E}^{sca}$ and $\boldsymbol{E}^{inc}$ are incident and scattered electric fields. The operator $\mathcal{K}$ is commonly seperated into principal-value and limit parts as

$$\mathcal{K}\{\boldsymbol{X}\}(\boldsymbol{r}) = \mathcal{K}_{PV}\{\boldsymbol{X}\}(\boldsymbol{r}) - \frac{4\pi - \Omega}{4\pi}\hat{\boldsymbol{n}} \times \boldsymbol{X}(\boldsymbol{r}), \quad 0 \leq \Omega \leq 4\pi \tag{2.35}$$

where $\mathcal{K}_{PV}$ is the principal-value part and Ω is the solid angle at the observation point. Using (2.35) and (2.32), the magnetic-field integral equation (MFIE) can be

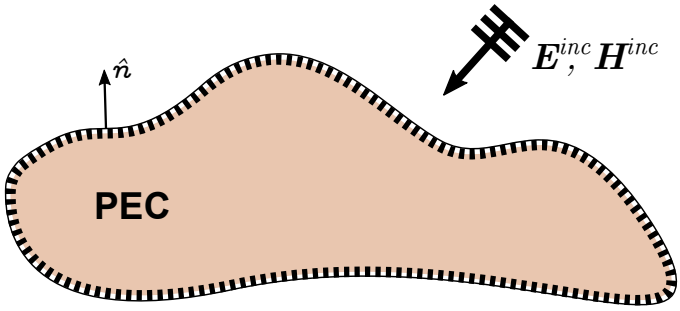

Figure 2.2: Boundary on a PEC surface.

written as

$$\frac{\Omega}{4\pi}\boldsymbol{J}(\boldsymbol{r}) - \hat{\boldsymbol{n}} \times \mathcal{K}_{PV}\{\boldsymbol{J}\}(\boldsymbol{r}) = \hat{\boldsymbol{n}} \times \boldsymbol{H}^{inc}(\boldsymbol{r}). \tag{2.36}$$

Rearranging the terms in Equation (2.34), the electric-field integral equation (EFIE) can be written as

$$-\eta\hat{\boldsymbol{n}} \times \hat{\boldsymbol{n}} \times \mathcal{T}\{\boldsymbol{J}\}(\boldsymbol{r}) = \hat{\boldsymbol{n}} \times \hat{\boldsymbol{n}} \times \boldsymbol{E}^{inc}(\boldsymbol{r}). \tag{2.37}$$

2.2 Method of Moments

Electromagnetics problems can be solved numerically by solving dense matrix equations obtained via MOM [24, 25], which can be generalized as

$$\mathcal{L}\{\boldsymbol{f}\}(\boldsymbol{r}) = \boldsymbol{g}(\boldsymbol{r}), \tag{2.38}$$

where $\mathcal{L}$ represents the linear operator applied on the unknown vector function $\boldsymbol{f}$ to be found and $\boldsymbol{g}$ represents the known vector function. In this work, $\mathcal{L}$ can be considered as linear combinations of $\mathcal{T}$ and $\mathcal{K}$, while $\boldsymbol{g}$ (namely, the right-hand-side vector or the excitation vector) includes incident electric and magnetic fields. The unknown vector function can be expanded as

$$\boldsymbol{f}(\boldsymbol{r}) \approx \sum_{n=1}^{N} \boldsymbol{a}[n]\boldsymbol{b}_n(\boldsymbol{r}), \tag{2.39}$$

where $\boldsymbol{b}_n$ ($n = 1, \ldots, N$) are known basis functions and $\boldsymbol{a}$ represents the unknown coefficient vector to be found. Testing (2.38) by using testing functions $\boldsymbol{t}_m$ ($m = 1, \ldots, N$) gives

$$\int d\boldsymbol{r}\boldsymbol{t}_m(\boldsymbol{r}) \cdot \sum_{n=1}^{N} \boldsymbol{a}[n]\mathcal{L}\{\boldsymbol{b}_n\}(\boldsymbol{r}) = \int d\boldsymbol{r}\boldsymbol{t}_m(\boldsymbol{r}) \cdot \boldsymbol{g}(\boldsymbol{r}). \tag{2.40}$$

Rearranging the terms in (2.40) leads to

$$\sum_{n=1}^{N} \boldsymbol{a}[n] \int d\boldsymbol{r} \boldsymbol{t}_m(\boldsymbol{r}) \cdot \boldsymbol{\mathcal{L}}\{\boldsymbol{b}_n\}(\boldsymbol{r}) = \int d\boldsymbol{r} \boldsymbol{t}_m(\boldsymbol{r}) \cdot \boldsymbol{g}(\boldsymbol{r}), \tag{2.41}$$

which can be rewritten as a matrix equation as

$$\sum_{n=1}^{N} \boldsymbol{a}[n] \bar{\boldsymbol{Z}}[m,n] = \boldsymbol{w}[m], \qquad m = 1, 2, \ldots, N, \tag{2.42}$$

where

$$\bar{\boldsymbol{Z}}[m,n] = \int d\boldsymbol{r} \boldsymbol{t}_m(\boldsymbol{r}) \cdot \boldsymbol{\mathcal{L}}\{\boldsymbol{b}_n\}(\boldsymbol{r}) \tag{2.43}$$

$$\boldsymbol{w}[m] = \int d\boldsymbol{r} \boldsymbol{t}_m(\boldsymbol{r}) \cdot \boldsymbol{g}(\boldsymbol{r}). \tag{2.44}$$

In this study, we apply a Galerkin scheme for the discretization of surface integral equations, i.e., we use $\boldsymbol{t}_m(\boldsymbol{r})$ and $\boldsymbol{b}_n(\boldsymbol{r})$ as the same set of functions.

2.3 Discretization

Triangular discretizations are widely used to model three-dimensional objects due to their flexible geometrical representations. To discretize surface integral equations, we use linear functions, such as the Rao-Wilton-Glisson (RWG) functions [4] that are defined on surface triangulations. An RWG function is defined on two neighbouring triangles with a common edge, as shown in Figure 2.3, and it can be written as

$$\boldsymbol{b}_n^{\text{RWG}}(\boldsymbol{r}) = \begin{cases} \dfrac{l_n}{2A_{n1}}(\boldsymbol{r} - \boldsymbol{r}_{n1}), & \boldsymbol{r} \in S_{n1} \\ \dfrac{l_n}{2A_{n2}}(\boldsymbol{r}_{n2} - \boldsymbol{r}), & \boldsymbol{r} \in S_{n2} \\ 0, & \boldsymbol{r} \in \text{elsewhere}, \end{cases} \tag{2.45}$$

where l_n is the length of the common edge, and A_{n1} and A_{n2} are the surface areas of the first triangle S_{n1} and the second triangle S_{n2}, respectively. In addition, $\boldsymbol{r}_{n1}$ and $\boldsymbol{r}_{n2}$ are the corner points opposite to l_n on S_{n1} and S_{n2}. Besides its simplicity, the RWG functions are divergence-conforming, providing finite charge values everywhere, which can be written as

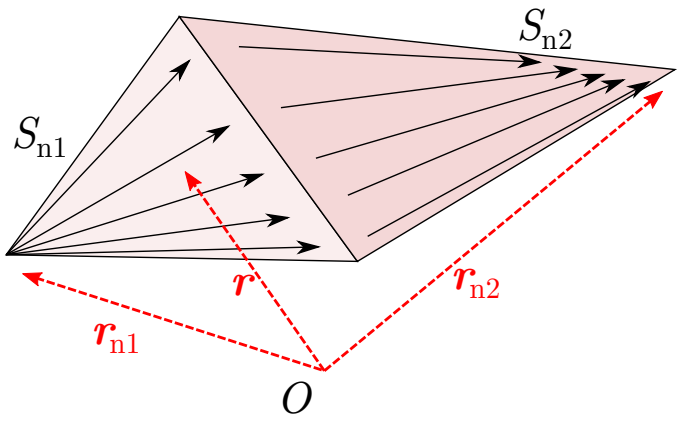

Figure 2.3: Illustration of an RWG function.

$$\nabla \cdot \boldsymbol{b}_n^{\mathrm{RWG}}(\boldsymbol{r}) = \begin{cases} \dfrac{l_n}{A_{n1}}, & \boldsymbol{r} \in S_{n1} \\ -\dfrac{l_n}{A_{n2}}, & \boldsymbol{r} \in S_{n2} \\ 0, & \boldsymbol{r} \in \text{elsewhere.} \end{cases} \tag{2.46}$$

Discretizing integro-differential equations MFIE and EFIE in (2.36) and (2.37) gives $N \times N$ impedance matrices, which can be written as

$$\begin{aligned} \bar{\boldsymbol{Z}}^{\mathrm{EFIE}}[m,n] &= i\omega\mu_0 \int_{S_m} d\boldsymbol{r} \boldsymbol{t}_m(\boldsymbol{r}) \cdot \int_{S_n} d\boldsymbol{r}' \boldsymbol{b}_n(\boldsymbol{r}') g_0(\boldsymbol{r},\boldsymbol{r}') \\ &\quad + \frac{1}{i\omega\epsilon_0} \int_{S_m} d\boldsymbol{r} \nabla \cdot \boldsymbol{t}_m(\boldsymbol{r}) \int_{S_n} d\boldsymbol{r}' g_0(\boldsymbol{r},\boldsymbol{r}') \nabla' \cdot \boldsymbol{b}_n(\boldsymbol{r}') \qquad (2.47) \\ \bar{\boldsymbol{Z}}^{\mathrm{MFIE}}[m,n] &= \frac{1}{2} \int_{S_m} d\boldsymbol{r} \boldsymbol{t}_m(\boldsymbol{r}) \cdot \boldsymbol{b}_n(\boldsymbol{r}) \\ &\quad + \int_{S_m} d\boldsymbol{r} \boldsymbol{t}_m(\boldsymbol{r}) \cdot \hat{\boldsymbol{n}} \times \int_{PV,S_n} d\boldsymbol{r}' \boldsymbol{b}_n(\boldsymbol{r}') \times \nabla' g_0(\boldsymbol{r},\boldsymbol{r}'), \qquad (2.48) \end{aligned}$$

while the right-hand-side vectors can be written as

$$\boldsymbol{w}^{\mathrm{EFIE}}[m] = -\int_{S_m} d\boldsymbol{r} \boldsymbol{t}_m(\boldsymbol{r}) \cdot \boldsymbol{E}^{\mathrm{inc}}(\boldsymbol{r}), \tag{2.49}$$

$$\boldsymbol{w}^{\mathrm{MFIE}}[m] = -\int_{S_m} d\boldsymbol{r} \boldsymbol{t}_m(\boldsymbol{r}) \cdot \hat{\boldsymbol{n}} \times \boldsymbol{H}^{\mathrm{inc}}(\boldsymbol{r}). \tag{2.50}$$

Applying RWG discretization, $\bar{\boldsymbol{Z}}^{\text{EFIE}}$ and $\bar{\boldsymbol{Z}}^{\text{MFIE}}$ in (2.47) and (2.48) can be written as

$$\bar{\boldsymbol{Z}}^{\text{EFIE}}[m,n,a,b] = i\omega\mu_0\mathcal{A}_{ma,nb}\int_{S_{ma}} d\boldsymbol{r}(\boldsymbol{r}-\boldsymbol{r}_{ma})\cdot\int_{S_{nb}} d\boldsymbol{r}'(\boldsymbol{r}'-\boldsymbol{r}_{nb})g_0(\boldsymbol{r},\boldsymbol{r}') + \frac{4}{i\omega\epsilon_0}\mathcal{A}_{ma,nb}\int_{S_{ma}} d\boldsymbol{r}\int_{S_{nb}} d\boldsymbol{r}' g_0(\boldsymbol{r},\boldsymbol{r}') \tag{2.51}$$

$$\bar{\boldsymbol{Z}}^{\text{MFIE}}[m,n,a,b] = -\frac{\mathcal{A}_{ma,nb}\delta_{ma,nb}}{2}\int_{S_{ma}} d\boldsymbol{r}(\boldsymbol{r}-\boldsymbol{r}_{ma})\cdot(\boldsymbol{r}-\boldsymbol{r}_{nb}) + \mathcal{A}_{ma,nb}\int_{S_{ma}} d\boldsymbol{r}(\boldsymbol{r}-\boldsymbol{r}_{ma})\cdot\hat{\boldsymbol{n}}\times\int_{PV,S_{nb}} d\boldsymbol{r}'(\boldsymbol{r}'-\boldsymbol{r}_{nb})\times\nabla' g_0(\boldsymbol{r},\boldsymbol{r}'), \tag{2.52}$$

where

$$\mathcal{A}_{ma,nb} = \frac{l_m l_n}{4A_{ma}A_{nb}}\gamma_{ma}\gamma_{nb}. \tag{2.53}$$

In the above, we have $\gamma_{nb},\gamma_{ma} = \pm 1$, depending on the direction of the basis and testing functions on triangles. Also, $\delta_{ma,nb} = 1$ when the integration is performed on a shared triangle for the basis and testing functions, while $\delta_{ma,nb} = 0$ elsewhere. The integrations in (2.49), (2.50), (2.51), and (2.52) are performed numerically using Gaussian quadratures [26] and the required singularity extractions due to $g_0(\boldsymbol{r},\boldsymbol{r}')$ and $\nabla' g_0(\boldsymbol{r},\boldsymbol{r}')$ are performed according to [27] and [28].

2.4 Multilevel Fast Multipole Algorithm

Applying MOM to surface formulations gives dense matrix equations, which can be written as

$$\bar{\boldsymbol{Z}}\cdot\boldsymbol{a} = \boldsymbol{w}, \tag{2.54}$$

where $\bar{\boldsymbol{Z}}$ is the known $N\times N$ impedance matrix, $\boldsymbol{w}$ is the known RHS vector containing the excitation information created by external sources, and $\boldsymbol{a}$ is the unknown current coefficient vector to be found. The construction of an $N\times N$ matrix has a time and memory complexity of $\mathcal{O}(N^2)$. A direct inversion of such a matrix using the Gaussian elimination method requires $\mathcal{O}(N^3)$ time complexity, which is a computational load that cannot be handled by the state-of-the-art computers for large values of N. Therefore, iterative methods, such as the biconjugate gradient stabilized method (BiCGStab), generalized minimal residual method (GMRES), and flexible-GMRES (FGMRES), are preferred for efficient solutions of matrix equations. These iterative methods are based on Krylov subspace methods, and they require at least one MVM

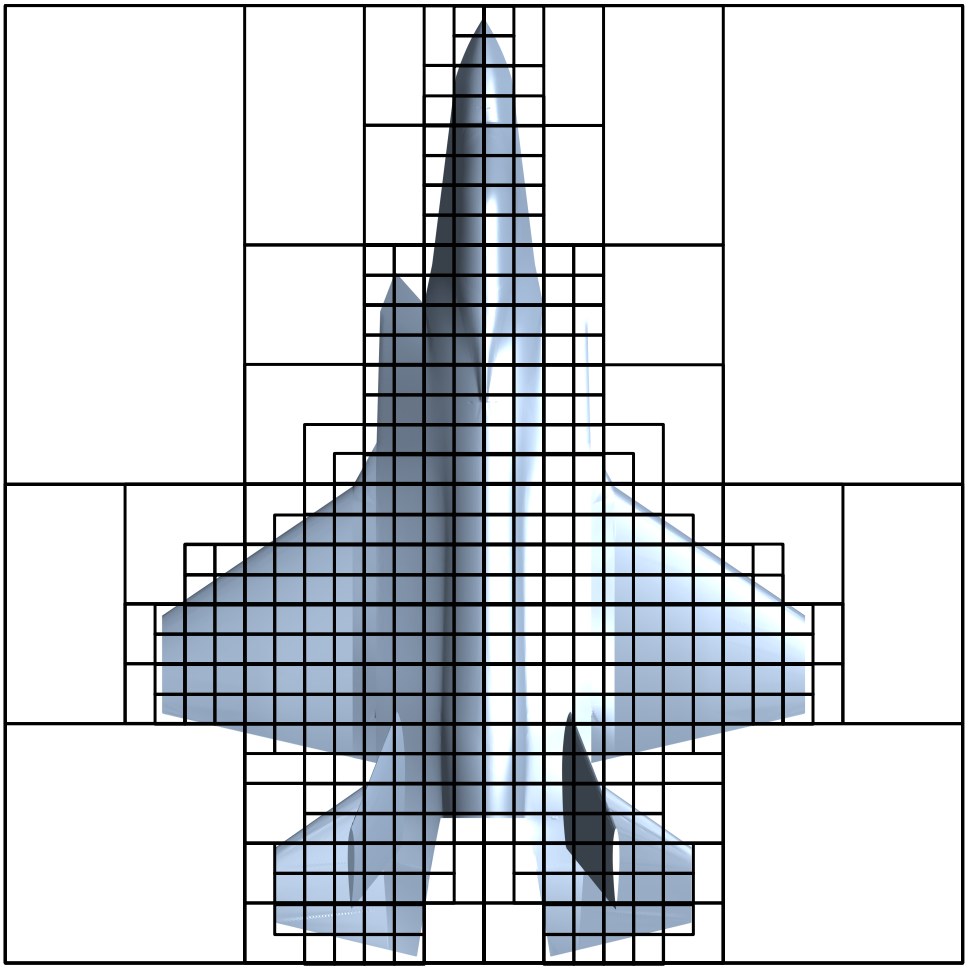

Figure 2.4: Recursive clustering of a target object to construct a tree-structure.

per iteration during an iterative solution. A direct MVM still requires $\mathcal{O}(N^2)$ computational operations, making it difficult to solve large-scale problems. Consequently, the fast multiple method (FMM) was developed for efficient solutions of large-scale radiation and scattering problems [29, 30]. On the other hand, FMM has $\mathcal{O}(N^{3/2})$ memory and time complexity, making this method inapplicable as the problem size grows. A multi-level scheme of FMM, namely the MLFMA [1, 31], fulfills the need for fast interaction calculations in large-scale problems with $\mathcal{O}(N \log N)$ memory and time complexity.

In an MLFMA implementation, a tree-structure is constructed to perform interaction computations in a group-by-group manner. The object is placed into a box, which is recursively divided into sub-boxes considering only non-empty domains, as shown

in Figure 2.4. The recursive division is terminated when the size of the boxes reach around $\lambda/4$ at the lowest level. The constructed tree structure with non-empty boxes determine the rules for near and far interactions, depending on the distance between boxes. Applying a one-box-buffer scheme, near-interactions and far-interactions are determined, which can be shown in a matrix form as

$$\bar{\boldsymbol{Z}}^N \cdot \boldsymbol{a} + \bar{\boldsymbol{Z}}^F \cdot \boldsymbol{a} = \boldsymbol{w}, \tag{2.55}$$

where $\bar{\boldsymbol{Z}}^N$ is the near-interaction matrix that is calculated directly and stored in memory, while $\bar{\boldsymbol{Z}}^F$ is the far-interaction matrix that is calculated on-the-fly.

MLFMA is based on the factorization and diagonalization of the Green's function using the Gegenbauer's addition theorem. Factorization of the Green's function is expressed as an expansion of spherical wave summation, which can be written as

$$\frac{\exp(ik|\boldsymbol{w}+\boldsymbol{v}|)}{4\pi|\boldsymbol{w}+\boldsymbol{v}|} = \frac{ik}{4\pi}\sum_{t=0}^{\infty}(-1)^t(2t+1)j_t(kv)h_t^{(1)}(kw)P_t(\hat{\boldsymbol{w}}\cdot\hat{\boldsymbol{v}}), \tag{2.56}$$

where $\boldsymbol{w}$ and $\boldsymbol{v}$ are vectors in three dimensions and $|\boldsymbol{w}| = w > v = |\boldsymbol{v}|$. In (2.56), j_t is the spherical Bessel function with order t, $h_t^{(1)}$ is the spherical Hankel function of the first kind with order t, and P_t is the Legendre polynomial. Then, diagonalization is applied, where the spherical waves are expressed in terms of plane waves by using the identity

$$j_t(kv)P_t(\hat{\boldsymbol{w}}\cdot\hat{\boldsymbol{v}}) = \frac{1}{4\pi(i)^t}\int d^2\hat{\boldsymbol{k}}\exp(ik\hat{\boldsymbol{k}}\cdot\boldsymbol{v})P_t(\hat{\boldsymbol{k}}\cdot\hat{\boldsymbol{w}}), \tag{2.57}$$

where $d^2\hat{\boldsymbol{k}}$ represents the sampling over the unit sphere and $\hat{\boldsymbol{k}}$ is the radial direction. We express the diagonalized form of the Green's function as

$$\frac{\exp(ik|\boldsymbol{w}+\boldsymbol{v}|)}{4\pi|\boldsymbol{w}+\boldsymbol{v}|} = \frac{ik}{4\pi}\sum_{t=0}^{\infty} i^t(2t+1)h_t^{(1)}(kw)\int d^2\hat{\boldsymbol{k}}\exp(ik\hat{\boldsymbol{k}}\cdot\boldsymbol{v})P_t(\hat{\boldsymbol{k}}\cdot\hat{\boldsymbol{w}}) \tag{2.58}$$

$$= \frac{ik}{4\pi}\int d^2\hat{\boldsymbol{k}}\exp(ik\hat{\boldsymbol{k}}\cdot\boldsymbol{v})\sum_{t=0}^{\infty} i^t(2t+1)h_t^{(1)}(kw)P_t(\hat{\boldsymbol{k}}\cdot\hat{\boldsymbol{w}}). \tag{2.59}$$

Finally, we define shifting and translation operators as

$$\beta(\hat{\boldsymbol{k}},\boldsymbol{v}) = \exp(ik\hat{\boldsymbol{k}}\cdot\boldsymbol{v}) \tag{2.60}$$

$$\alpha(\hat{\boldsymbol{k}},\boldsymbol{w}) = \sum_{t=0}^{\infty} i^t(2t+1)h_t^{(1)}(kw)P_t(\hat{\boldsymbol{k}}\cdot\hat{\boldsymbol{w}}) \tag{2.61}$$

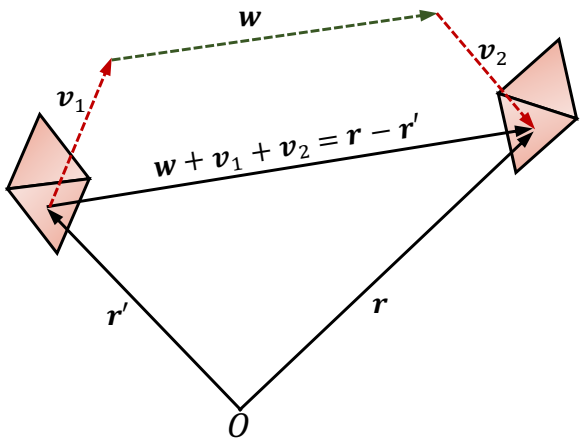

Figure 2.5: Interaction between a basis and a testing function.

to rewrite the diagonalized form of the Green's function as

$$\frac{\exp(ik|\boldsymbol{w}+\boldsymbol{v}|)}{4\pi|\boldsymbol{w}+\boldsymbol{v}|} = \frac{ik}{4\pi}\int d^2\hat{\boldsymbol{k}}\beta(\hat{\boldsymbol{k}},\boldsymbol{v})\alpha(\hat{\boldsymbol{k}},\boldsymbol{w}). \tag{2.62}$$

In practice, the infinite summation in the translation operator is terminated at a finite value [32], which can be written as

$$\tau \approx 1.73ka + 2/15(d_0)^{2/3}(ka)^{1/3}, \tag{2.63}$$

where a is the box size and d_0 is the desired number of accurate digits. The useful property of the diagonalized Green's function is that the shifting operator can easily be decomposed as shown in Figure 2.5, which can be written as

$$\begin{aligned}\frac{\exp(ik|\boldsymbol{w}+\boldsymbol{v}|)}{4\pi|\boldsymbol{w}+\boldsymbol{v}|} &= \frac{\exp(ik|\boldsymbol{w}+\boldsymbol{v}_1+\boldsymbol{v}_2|)}{4\pi|\boldsymbol{w}+\boldsymbol{v}_1+\boldsymbol{v}_2|} \\ &\approx \frac{ik}{4\pi}\int d^2\hat{\boldsymbol{k}}\beta(\hat{\boldsymbol{k}},\boldsymbol{v}_1)\beta(\hat{\boldsymbol{k}},\boldsymbol{v}_2)\alpha_\tau(\hat{\boldsymbol{k}},\boldsymbol{w}).\end{aligned} \tag{2.64}$$

Using the idea of the decomposed shifting operator in (2.64), we can construct a group-by-group calculation in a multi-level scheme. In this scheme, $\beta(\hat{\boldsymbol{k}},\boldsymbol{v}_1)$ and $\beta(\hat{\boldsymbol{k}},\boldsymbol{v}_2)$ represent the aggregation and disaggregation operations. Since the multi-level scheme requires different τ values at each level (box size), sample transformations between levels are performed via interpolation and anterpolation [33] during the aggregation and disaggregation stages.

2.5 Novelties

In this section, we briefly present our works that have build a basis for the main topic considered in this thesis. We categorize these works as formulations, discretizations, kernels, preconditioners, and applications.

In the formulation studies, we consider accurate and efficient solutions for both penetrable and impenetrable (PEC) objects. Using surface formulations, solutions of penetrable objects are sensitive to object shape and electromagnetic characteristics, such as permittivity and permeability. For large negative permittivity values and near-zero permittivity/permeability values, matrix equations obtained by surface formulations typically become ill-conditioned and/or inaccurate. A modified combined-tangential formulation (MCTF) [34–38] is presented for fast and accurate solutions of objects with large negative permittivities. MCTF is compared with the conventional formulations and its superiority is shown in terms of accuracy and iterative convergence. Similarly, a new mixed formulation [39–42] is presented for rigorous solutions of objects with near-zero permittivity and/or permittivity values. Numerical comparisons show that the conventional formulations mostly fail in terms of accuracy and convergence, while the new mixed formulation yields a good accuracy and stability over wide ranges of relative permittivity and permeability values. We also present a hybrid-field integral equation (HFIE) [43–47] to obtain accurate and efficient solutions for PEC objects with fine geometrical details. Electrically small details cause challenges for EFIE in terms of iterative convergence. On the other hand, MFIE and CFIE fail to provide accurate results. In the hybrid formulation, we apply CFIE with different weights over the given object, where the parts of the object with fine details are formulated via higher EFIE weights and the parts with large smooth surfaces are formulated by using higher MFIE weights.

In the context of discretization studies, we present a new approach based on numerical constructions of testing functions [48–51] for improving the accuracy of MFIE and CFIE with low-order discretizations. Considering numerical solutions, testing functions are designed by enforcing the compatibility of the MFIE systems with the accurate coefficients obtained by solving EFIE. We demonstrate accuracy improvements on scattering problems, where the testing functions designed at a single fre-

quency are used in frequency ranges. The proposed approach is easy to implement by using existing codes, while it improves the accuracy of MFIE and CFIE without deteriorating the efficiency of iterative solutions.

In the kernel studies, we eliminate the low-frequency breakdown of the diagonalized Green's function by using approximate diagonalization (AD) [52–62] and by using additional digits via mixed precision arithmetics (MPA) [63–65] instead of hardware-based fixed numbers of digits. We show that AD is stable for arbitrarily short distances with respect to wavelength. The diagonalization is based on scaled spherical functions and plane waves, where a scaling factor is used to stabilize special functions with small arguments. Optimization of the scaling factor leads to accurate diagonalizations, which can be used for efficient simulations of multi-scale objects, multi-level solutions of potential formulations, and multi-level solutions of objects with near-zero-index materials. The conventional diagonalization of the Green's function can also be stabilized by using MPA for accurate computations of subwavelength interactions. MPA provides a direct remedy for the low-frequency breakdown of the standard diagonalization based on plane waves and it enables straightforward implementations for low-frequency problems.

In the preconditioner studies, nested iterative solutions [66, 67] using full and approximate MLFMA are presented for efficient analysis of electromagnetic problems. The developed mechanism is based on preconditioning an iterative solution via another iterative solution, and this way, nesting multiple solutions as layers.

Finally, in application-based studies, we cover a plethora of applications, such as analyzing and optimizing nanowires [68–79], solving complex metallic and penetrable structures at optical frequencies [80–84], designing solar cell structures with high absorption rates [85–88], optimizing photonic crystals [89–92] for beamforming, and modelling surface corrugations [93, 94]. We also focus efficient combinations of MLFMA with heuristic optimization algorithms, such as genetic algorithms [95–99], as well as solutions of large targets [100, 101].

CHAPTER 3

TRIMMED MULTILEVEL FAST MULTIPOLE ALGORITHM

In this chapter, we present the details of T-MLFMA. First, we explain the application of the trimming scheme on MOM matrices. Then, we present the trimming scheme on MLFMA tree structures. Third, we provide the details of trimming testing functions. Finally, we show the details of the basis-function-trimming implementation using ML.

3.1 Trimming Scheme on MOM Matrix

Consider the matrix equation in (2.54), where $\bar{\boldsymbol{Z}}$ is an $N \times N$ matrix. The unknown $\boldsymbol{a}$ can be calculated within a desired error level by using Krylov subspace vectors, which can be written as

$$\boldsymbol{\mathcal{K}}_r(\bar{\boldsymbol{Z}}, \boldsymbol{w}) = \text{span}\{\boldsymbol{w}, \bar{\boldsymbol{Z}} \cdot \boldsymbol{w}, \bar{\boldsymbol{Z}}^2 \cdot \boldsymbol{w}, ..., \bar{\boldsymbol{Z}}^{r-1} \cdot \boldsymbol{w}\}. \tag{3.1}$$

In this expression, r is the order of the subspace, which is smaller than or equal to N. The error of the solution is expected to decrease as the iterations continue, i.e., as the number of Krylov subspace vectors increases. The decreasing error also shows that the contributions of the Krylov subspace vectors become smaller as the iterations continue, although these contributions can be essential to achieve the desired error level. In order to have a better understanding of the Krylov subspace vectors, we investigate the powers of matrix $\bar{\boldsymbol{Z}}$ and the vectors constituting Equation (3.1) for a sample problem. To illustrate the concept and elaborate the proposed strategy, Figure 3.1 depicts pictures of the impedance matrix related to a perfectly conducting sphere of radius 300 mm. The geometry is illuminated by a plane wave at 1 GHz and it is discretized with $\lambda/10$ triangles, leading to a matrix equation involving 4080 unknowns. The powers of matrix $\bar{\boldsymbol{Z}}$ for this problem are shown in Figure 3.1, where

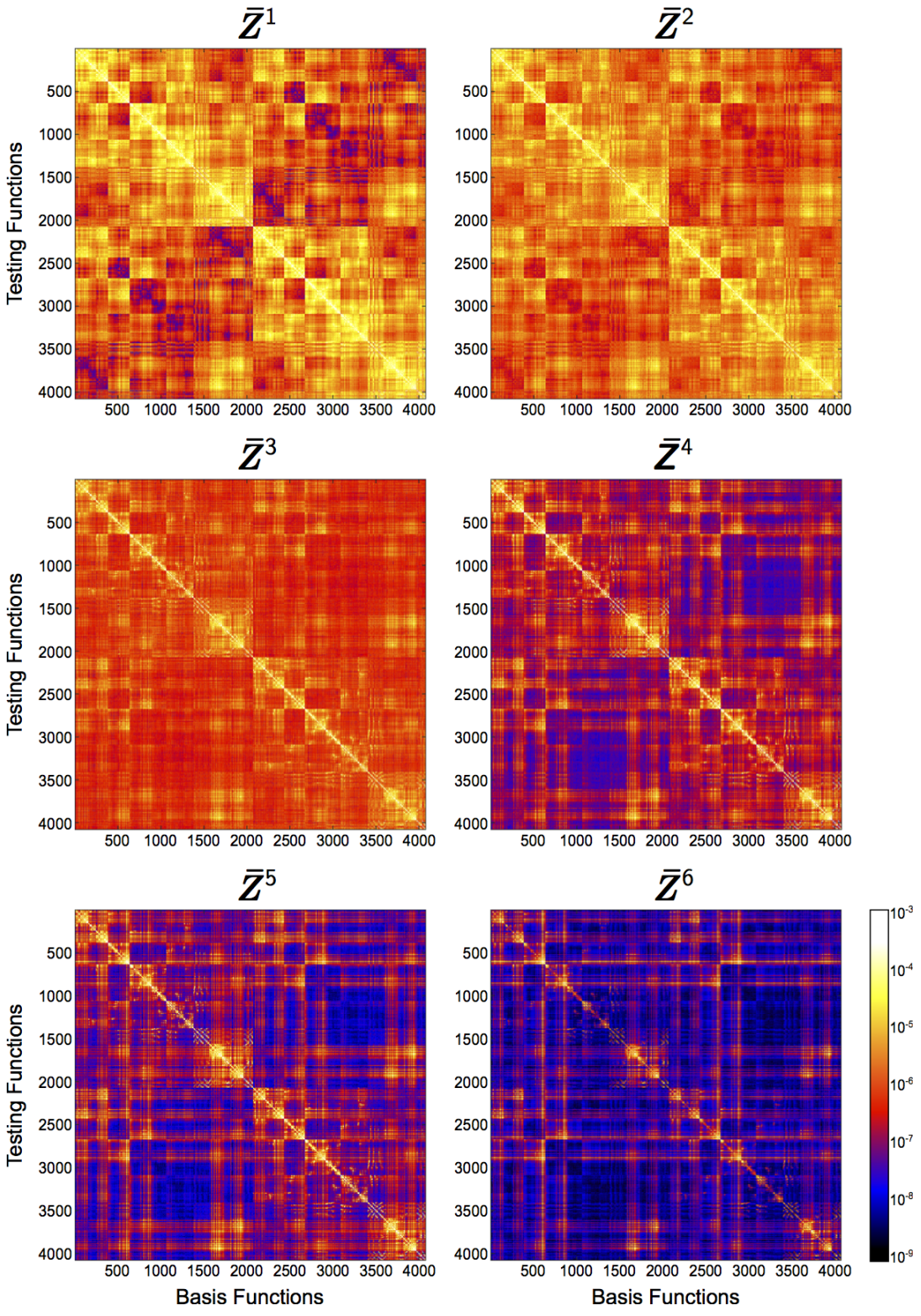

Figure 3.1: Powers of the impedance matrix for a scattering problem involving a 2λ sphere formulated via CFIE.

logarithmic scaling is used as

$$\log_{10}\left(\frac{\bar{\boldsymbol{Z}}^n}{\left|\left|\bar{\boldsymbol{Z}}^n\right|\right|_{fro}}\right), \quad n = 1, 2, 3, 4, 5, 6. \tag{3.2}$$

Specifically, $\bar{\boldsymbol{Z}}^n$ is divided by its Frobenius norm to make clear comparisons between matrix elements. Due to the nature of iterative solvers, unknown equivalent surface currents and the corresponding scattered fields on equivalence surfaces converge to true solutions as iterations proceed. On the other hand, after a number of iterations, some interactions in an MVM provide smaller contributions to the iteration updates. It can be observed that some regions of the matrices in Figure 3.1 are significantly dominant, while the rest become exponentially smaller. Large differences between matrix elements indicate that only a limited region of the matrix effectively represents the overall matrix. The vectors of the Krylov subspace for the same problem are calculated and shown in Figure 3.2. In this plot, the vertical axis indicates the testing functions, while the subspace vectors are shown in the horizontal axis. The subspace vectors are calculated as

$$\log_{10}\left(\frac{\bar{\boldsymbol{Z}}^n \cdot \boldsymbol{w}}{\left|\left|\bar{\boldsymbol{Z}}^n \cdot \boldsymbol{w}\right|\right|_2}\right), \quad n = 1, 2, 3, ...N. \tag{3.3}$$

Most of the subspace vectors converge before $n = 20$, and the changes in the element values between the vectors become insignificant after $n = 40$. Hence, we can omit the interactions of the converged regions since they provide less significant contributions. We also observe converging behavior when the same scattering problem is formulated by using EFIE as well, as depicted in Figure 3.3. In these results, large portions of the vectors converge before $n = 20$. Therefore, independent from the formulation, we observe locally converged regions in MVMs.

The trimming-scheme-integrated iterative solution workflow is shown in Figure 3.4. In a regular iterative solution, at iteration i, the solver gives vector $\boldsymbol{a}_i$ to the MVM operator and takes back the result vector $\boldsymbol{w}_i$, as shown with the solid arrows. The dashed arrows represent the trimming process during the iterative solution. Basis function trimming and testing function trimming processes are performed separately. In an ideal scenario, we could compare the input vector $\boldsymbol{a}_i$ with the final solution $\boldsymbol{a}$ to determine the converged coefficients. But, since we do not have the final result, and interactions cannot be checked one by one (otherwise, the complexity would be

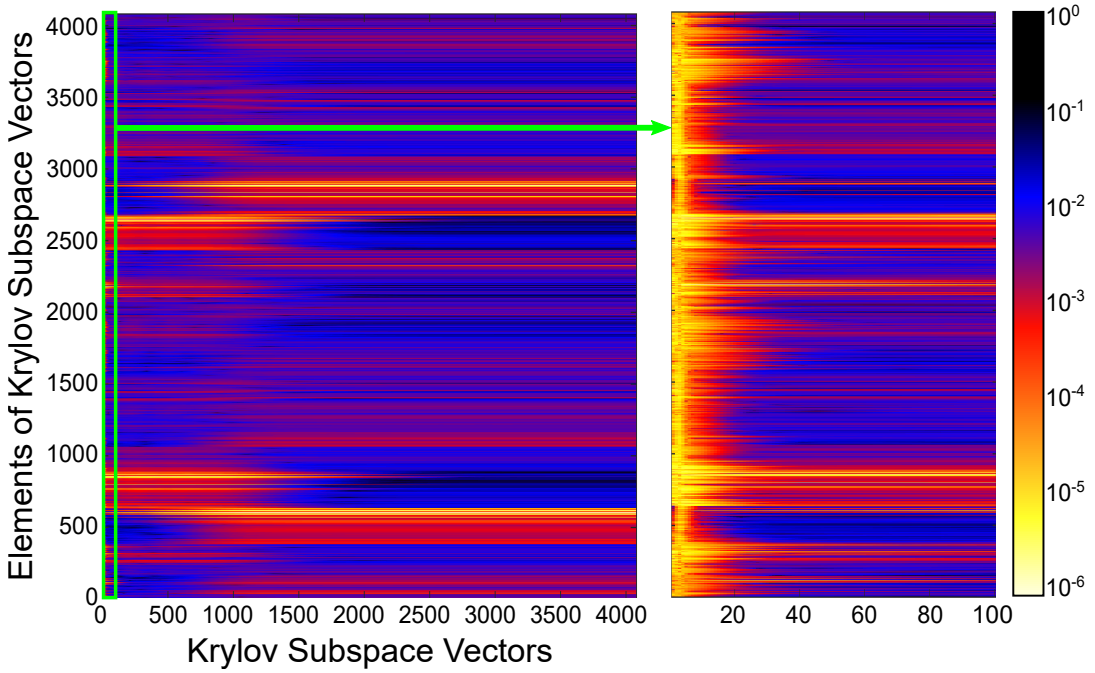

Figure 3.2: Krylov subspace vectors for a scattering problem involving a 2λ sphere formulated via CFIE.

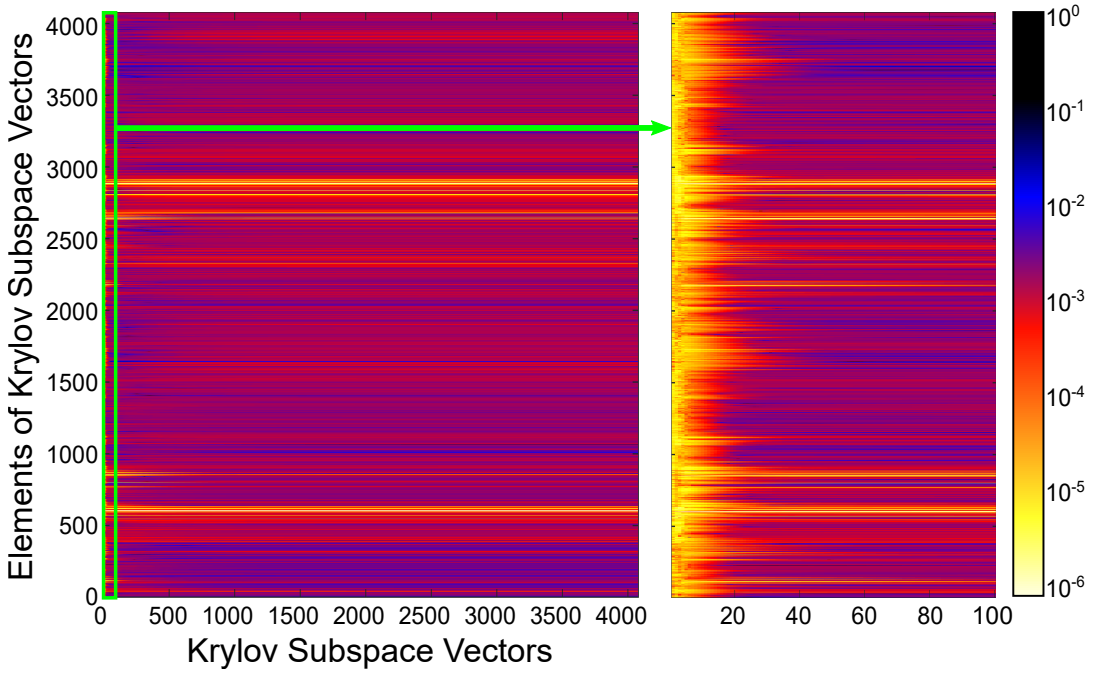

Figure 3.3: Krylov subspace vectors for a scattering problem involving a 2λ sphere formulated via EFIE.

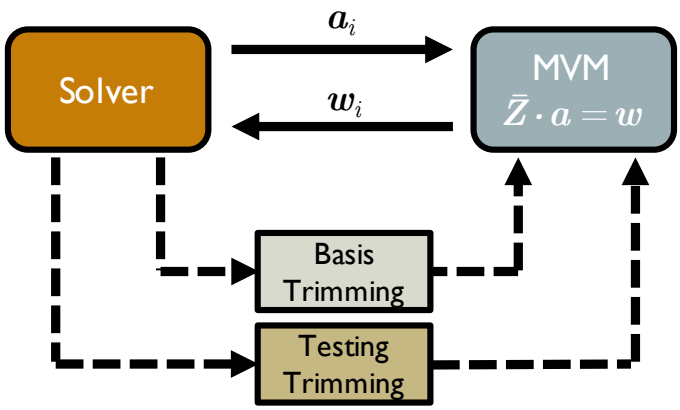

Figure 3.4: Workflow of iterative solutions with trimming method.

$\mathcal{O}(N^2)$), we employ ML to predict which interactions can safely be omitted. Specifically, during an iterative solution, the progress in equivalent surface currents are observed and the corresponding error levels are predicted at each iteration by an ML technique. The ML technique estimates the error in the surface currents so that the converged current coefficients (matrix columns) can be omitted in the far-zone interaction computations, leading to an increasingly sparser matrix as the iterations continue (basis trimming). In a more straightforward manner, the calculated scattered fields are also compared with the given right-hand-side vector and the matrix rows corresponding to sufficiently small error values are omitted (testing trimming). We present the details of the implemented ML-based basis trimming and straightforward testing trimming in the following sections of this chapter.

To illustrate the concept and elaborate the proposed strategy, Figure 3.5 depicts pictures of the impedance matrix related to the above mentioned perfectly conducting sphere of diameter 2λ. The GMRES algorithm is used as the iterative solver. For omitting interactions, the convergence threshold is set to 10%, i.e., a basis/testing function and the related interactions are dropped if the corresponding error (of current/field) is smaller than 10%. Figure 3.5 presents the matrix density with respect to the GMRES iterations and the status of the impedance matrix at the intervals of five iterations. The impedance matrix is decomposed into near-zone and far-zone matrices, while a 4-level MLFMA tree-structure determines near-zone and far-zone interactions. In the figure, white and red regions correspond to near-zone and far-

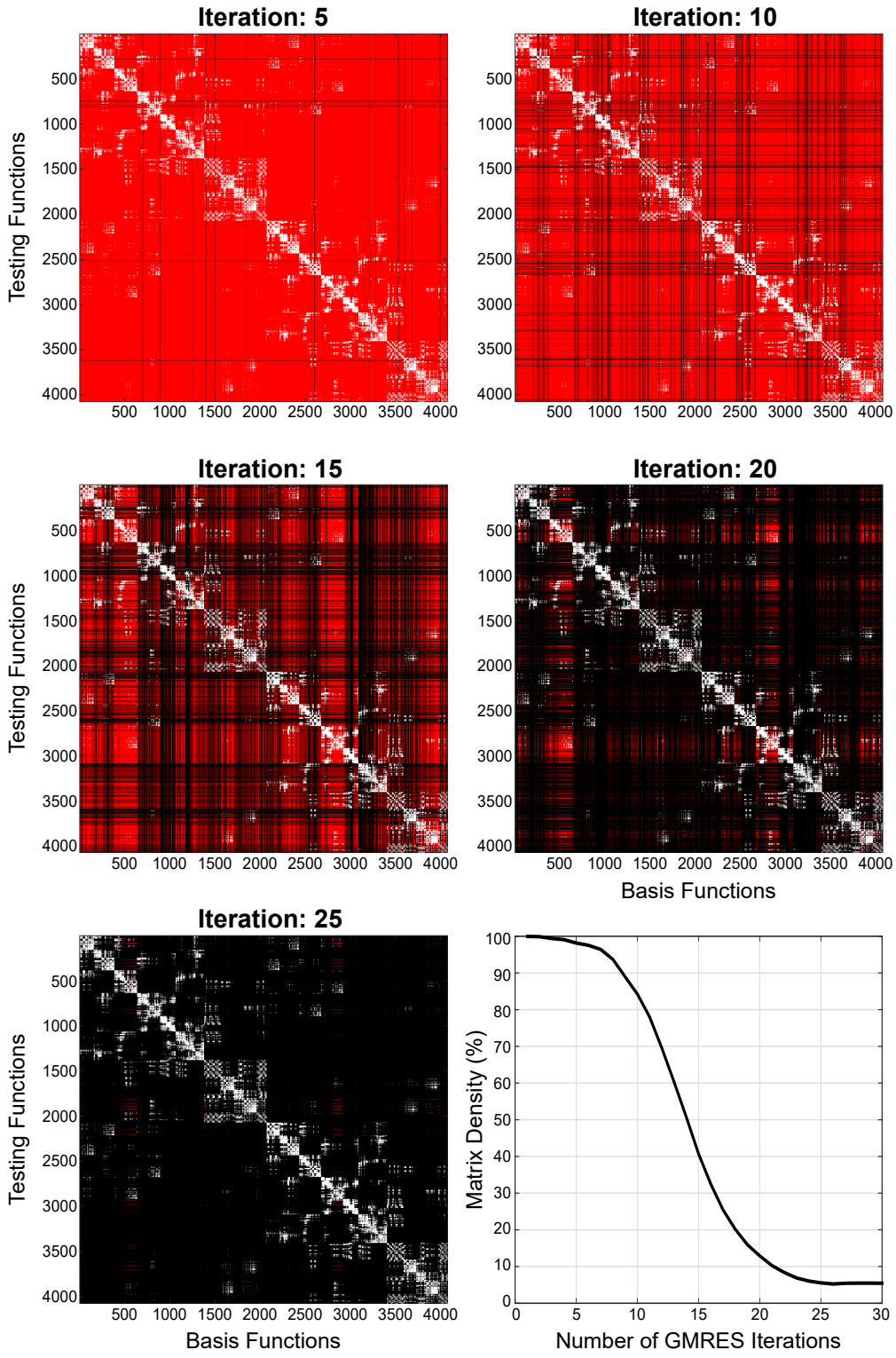

Figure 3.5: Trimmed matrix layout for a 2λ PEC sphere at five different iterations and the corresponding matrix density with respect to iterations.

zone interactions, whereas the black areas (rows and columns) represent the omitted far-zone interactions. We observe that the matrix becomes increasingly sparse with the final density value of 5.45%, which corresponds to the near-zone matrix density value. As the iterations continue, we can reduce the computational complexity of MVM operation from $\mathcal{O}(N \log N)$ to $\mathcal{O}(N)$, which is the computational complexity of the near-zone matrix.

3.2 Trimming Scheme on MLFMA

Now, we discuss the application of the trimming scheme in the context of MLFMA. In a regular MLFMA implementation, aggregation, translation, and disaggregation stages share the same tree-structure at each and every iteration. Aggregation calculations start from the lowest level of the tree-structure, involving the aggregation of fields of smaller clusters into radiated fields of larger clusters until the top level. Translation calculations start after the aggregation, and they occur between clusters at the same level, involving the transfer of radiated fields into incoming fields between far-zone clusters. Disaggregation calculations follow the translation and they are performed in the opposite direction of the aggregation, i.e., starting from the top-level clusters, incoming fields are disaggregated to smaller clusters until the lowest level. These calculations are repeated at each and every iteration, making the MVM time per iteration constant. As shown in the previous section, some portions of a matrix, i.e., converged regions of surface currents and scattered fields, can be omitted. Therefore, we implement an interaction trimming method into MLFMA to obtain a significant acceleration in MVMs at the cost of reduced but controlled accuracy. On the other hand, such a trimming operation is not trivial and it requires significant changes in MLFMA tree structures for all stages of aggregation, translation, and disaggregation. First, MLFMA stages in a trimmed scheme may follow different tree-structures due to non-symmetric convergence behaviors of basis and testing functions. Second, once a trimming is applied, it must propagate to all branches of the tree to obtain maximum efficiency from the trimming process. Third, the elimination process in a tree structure should be formed cumulatively based on the evolution of the tree structure with respect to iterations. Otherwise, the convergence of the iterative solution may deteriorate.

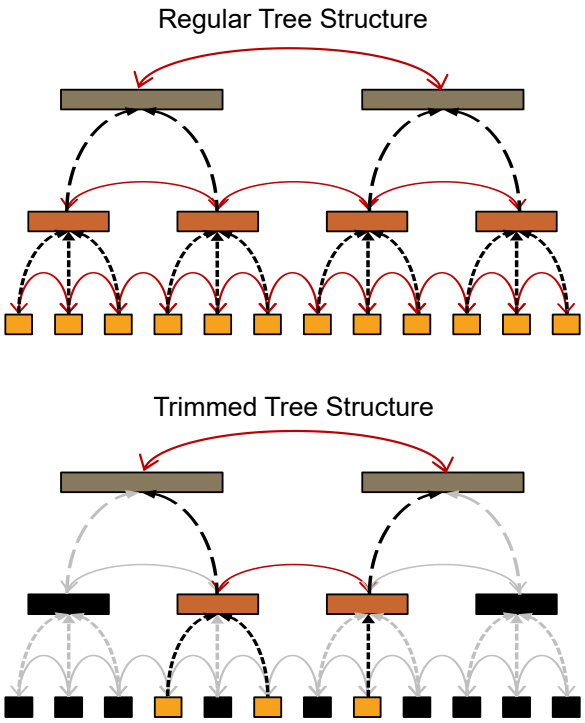

Figure 3.6: The interaction scheme for a regular tree structure and a trimmed tree structure.

We show the difference between a regular tree structure and a trimmed tree structure in Figure 3.6. Colors of the boxes represent clusters at different levels. Red solid arrows show translations, while black dashed arrows represent the aggregation directions (or opposite disaggregation directions). As it is shown, all of the boxes must be involved in the regular calculations. On the other hand, some boxes (black color) are omitted in the trimmed tree. A box is omitted if all contained discretization elements or all sub-boxes are already excluded. An omitted box is not included in aggregation (or disaggregation) and translation operations.

The basis and testing trimming operators in Figure 3.4 update aggregation and disaggregation schemes at the end of each iteration. The steps followed in a trimming operation for testing functions and disaggregation tree branches are given in Algorithm 1. In the first step, the testing function error calculator (TFEC) calculates the errors associated with the testing functions. For such calculations, TFEC uses the latest MVM result vector $\boldsymbol{w}_i$ and the right-hand-side vector $\boldsymbol{w}$, and then returns β as the error value. If β for a testing function is below the given threshold, it is excluded from

Algorithm 1 Trimming Testing Functions and Disaggregation Tree Branches

for $m = 1 : N$ **do**
    $\beta = \text{TFEC}(\boldsymbol{w}[m], \boldsymbol{w}_i[m])$
    if $\beta < threshold$ **then**
        exclude $\boldsymbol{t}_m$
    end if
end for
for $level = L : 3$ **do**
    for $box = 1 : B_{level}$ **do**
        if all testing functions in box are excluded **then**
            exclude box from translation
            exclude box from disaggregation
        end if
    end for
    Update B_{level}
end for

MLFMA calculations for the rest of the solution. In the second step, starting from the bottom level, the disaggregation tree is updated. If all testing functions are excluded for a box at the bottom level, it is excluded from translation and disaggregation calculations. Then, the higher levels are updated with a similar procedure until the whole tree is scanned. The steps followed in trimming operations for basis functions and aggregation tree branches are given in Algorithm 2. The algorithm is similar to Algorithm 1. In the first step, the basis function error predictor (BFEP) estimates the errors associated with all basis functions. BFEP consists of an ML technique to make reliable estimations since the reference (final) values do not exist (and obtaining the final values is the ultimate goal of the iterative solution). The iterative solver provides the latest (e.g., last three) solution vectors to BFEP to obtain the predictions. Then, BFEP provides the error value of α for each basis function. If α for a basis function is below the given threshold, it is excluded from MLFMA calculations for the rest of the solution. In the second step, starting from the bottom level, the aggregation tree is updated. If all basis functions are excluded for a box at the bottom level, it is excluded from aggregation and translation calculations. In a similar fashion, the higher levels

Algorithm 2 Trimming Basis Functions and Aggregation Tree Branches

for $n = 1 : N$ **do**
  $\alpha = \text{BFEP}(\boldsymbol{a}_i[n], \boldsymbol{a}_{i-1}[n], \boldsymbol{a}_{i-2}[n])$
  if $\alpha < threshold$ **then**
    exclude $\boldsymbol{b}_n$
  end if
end for
for $level = L : 3$ **do**
  for $box = 1 : B_{level}$ **do**
    if all basis functions in box are excluded **then**
      exclude box from aggregation
      exclude box from translation
    end if
  end for
  Update B_{level}
end for

are updated considering new empty boxes until the tree is completely scanned. When basis and testing function trimming operations are properly performed, we obtain a new MVM operator, which can perform faster MVMs in comparison to the previous MVM operators. MLFMA that works on such trimmed tree structures, which become increasingly sparser as iterations continue, is called T-MLFMA.

To demonstrate the improved efficiency of T-MLFMA, we consider a scattering problem involving the Flamme geometry with an electrical size of 64λ. Using $\lambda/10$ triangles, the constructed matrix equation involves 811,080 unknowns. The object is illuminated by a horizontally polarized plane wave at 30° angle from the back ($-x$ axis). The convergence thresholds in T-MLFMA are defined as 10% for both surface currents (basis functions) and tested scattered fields (testing functions). Figures 3.7 and 3.8 present the status of the trimmed basis and testing functions on the geometry at the intervals of ten iterations. White regions on the geometries correspond to included basis/testing functions, while yellow, red, and black areas depict triangles with one, two, and three excluded edges, respectively. The white and black regions in the aggregation and disaggregation trees in Figures 3.7 and 3.8 show the included

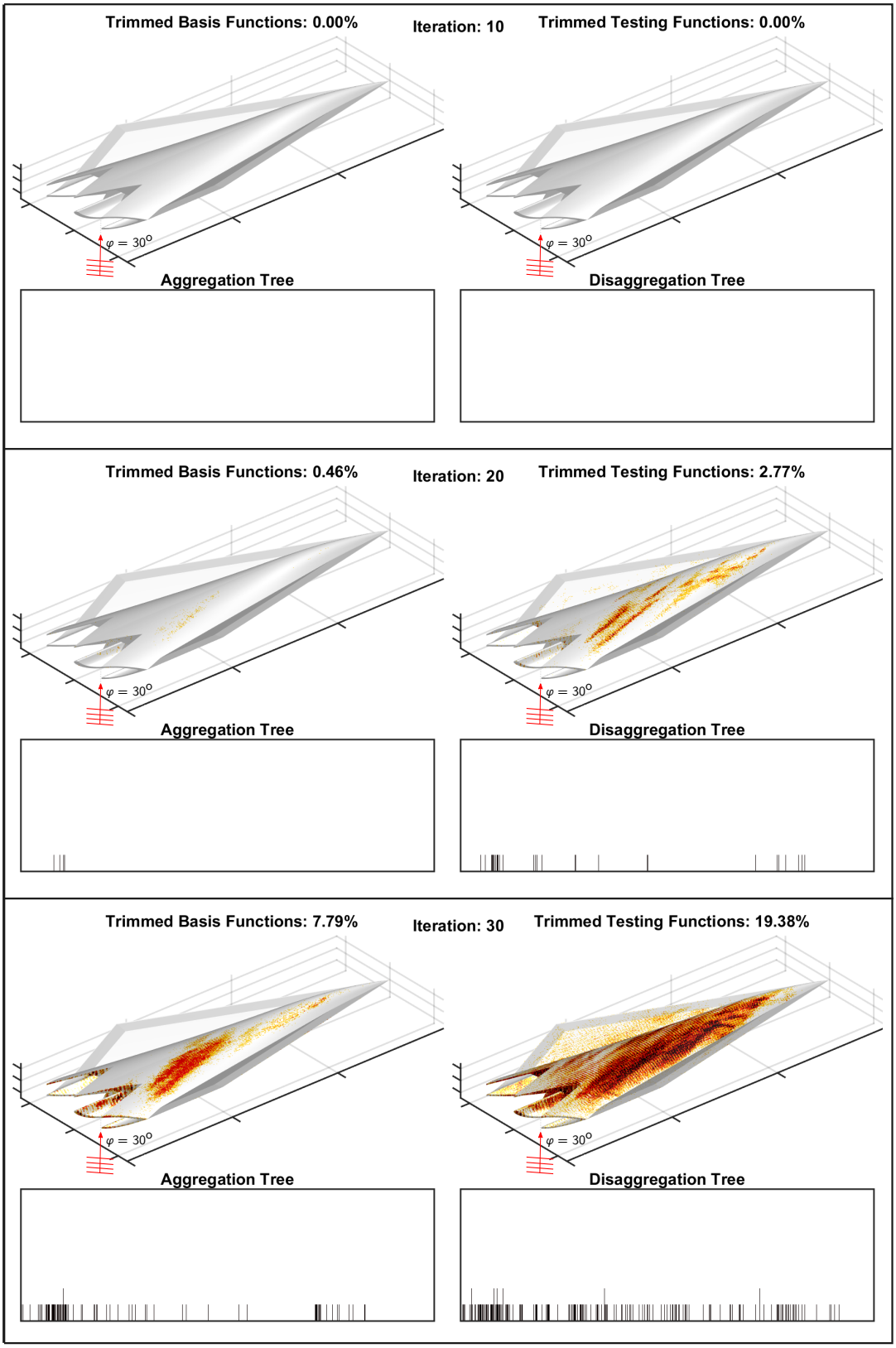

Figure 3.7: Basis/testing function trimming layout for a scattering problem involving the Flamme geometry with an electrical size of 64λ. Results of iterations 10, 20, and 30 are considered.

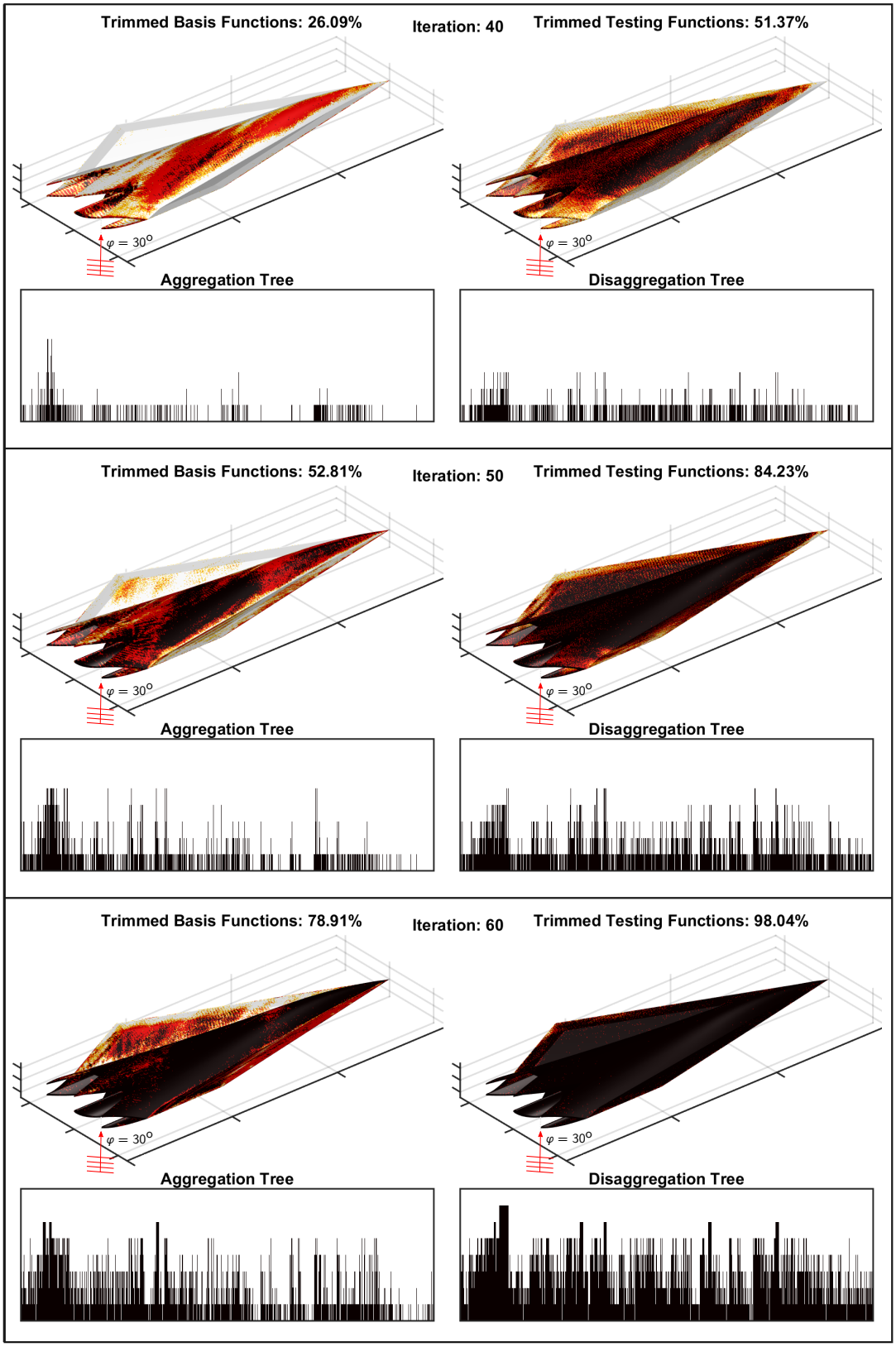

Figure 3.8: Basis/testing function trimming layout for a scattering problem involving the Flamme geometry with an electrical size of 64λ. Results of iterations 40, 50, and 60 are considered.

and excluded boxes. The bottom layers of the tree figures represent the basis/testing functions, while the lowest level boxes reside in the second layer. At the higher levels, the number of boxes decreases, but each box contains significantly large numbers of basis/testing functions. Thus, these larger boxes are represented by wider areas. We observe that the tree branches become increasingly sparser as the iterations proceed. We present further details of this numerical experiment in Chapter 4.

3.3 Testing Function Error Calculation Using Straightforward Check

In order to perform a straightforward calculation, TFEC requires the residual error

$$\boldsymbol{R}_i = \boldsymbol{w} - \bar{\boldsymbol{Z}} \cdot \boldsymbol{a}_i \tag{3.4}$$

at the end of each iteration. The absolute relative residual error, the return value of TFEC, for any testing function m is calculated as

$$\beta = \frac{|\boldsymbol{R}_i[m]|}{|\boldsymbol{w}[m]|}. \tag{3.5}$$

The value of β also has a physical meaning in terms of scattered fields. An MVM result gives scattered fields on the tested regions. Then, the residual error represents the difference of incident fields and calculated scattered fields. Therefore, β in Equation (3.5) corresponds to the error of T-MLFMA when satisfying boundary conditions on the tested regions.

3.4 Trimming Basis Functions Using ML

ML techniques are based on learning specific tasks from the given information. There are three main learning approaches in ML, i.e., supervised learning, unsupervised learning, and reinforcement learning. A supervised learning is based on a given dataset, where the input data and the output data are labeled. The training algorithm forces the ML model to make a correlation between the input and output data. Therefore, the success of the ML model depends on the comprehensiveness of the dataset. In the unsupervised learning approach, the training algorithm shares only the input data with the ML model. In this case, the ML model should discover the correlation in the dataset. The reinforcement learning approach uses both supervised and unsupervised techniques. The dataset contains labeled input and outputs. However, the

learning algorithm does not directly share the output reference with the ML model, while it states whether the model gives a correct or an incorrect answer. In this study, we prefer the supervised learning approach on the artificial neural networks (ANN) based on the structure of our data type.

In the following part, we explain the steps that we follow to construct an ML-based BFEP. First, we present the details of the dataset content. Then, we explain the ML model parameters of the error predictor, as well as the training details.

3.4.1 Details of Dataset

We consider geometries with various types and sizes in our dataset since it is essential to construct a comprehensive dataset to train a successful ML model. In the constructed raw dataset, NASA Almond geometry [102] ($16\lambda \times 128$, $32\lambda \times 64$, $64\lambda \times 64$), Flamme geometry [103] ($16\lambda \times 128$, $32\lambda \times 64$, $64\lambda \times 64$), cube geometry ($16\lambda \times 8$, $32\lambda \times 8$), and sphere geometry ($16\lambda \times 1$, $32\lambda \times 1$, $64\lambda \times 1$) are considered. Therefore, the raw dataset consists of $256 + 256 + 16 + 3 = 531$ full-wave simulations. The total number of iterations for each model are shown in Table 3.1.

Table 3.1: The models used in the raw dataset

Model	**Size** λ	**Number of Solutions**	**Total Number of Iterations**
Sphere	16	1	27
Sphere	32	1	31
Sphere	64	1	38
Cube	16	8	196
Cube	32	8	225
Almond	16	128	2615
Almond	32	64	1470
Almond	64	64	1817
Flamme	16	128	11040
Flamme	32	64	7508
Flamme	64	64	6534

The electromagnetic scattering problems are formulated by using CFIE and discretized with $\lambda/10$ RWG functions. The solutions are obtained by using GMRES, where the required MVMs are accelerated via MLFMA with 1% maximum error. In each solution, the geometry is illuminated via a plane wave with random propagation and polarization, while surface current coefficients are saved in each iteration. This way, various surface current distributions are obtained.

The inputs of the ML structure represent a history of surface current coefficients for every iteration. Coefficients of the most recent three iterations, i.e., $\boldsymbol{a}_i$, $\boldsymbol{a}_{i-1}$, and $\boldsymbol{a}_{i-2}$, are selected. Before using as inputs, these coefficients are divided element-wise by using coefficients of another iteration. In this study, we use $\boldsymbol{a}_{i-3}$ for the division process, while the average of $\boldsymbol{a}_i$, $\boldsymbol{a}_{i-1}$, and $\boldsymbol{a}_{i-2}$ works as well. The division process is required for the generalization of the current-coefficient behavior over iterations. Finally, the coefficients are separated into their real and imaginary parts, which are set as inputs of the constructed ML structure, while the element-wise relative errors in $\boldsymbol{a}_i$ with respect to the final result are set as outputs.

3.4.2 Details of Error Predictor Model and Training Results

In the last decade, ANNs and convolutional neural networks have been shown in the literature with their detection, classifications, and prediction capabilities. Therefore, ANN structures are perfect candidates for the error estimation operation in this study. The main purpose of the ANN model in our work is to provide error predictions of given current coefficients as accurate and as fast as possible. We can achieve fast predictions by using compact structures involving small numbers of layers and small numbers of neurons on each layer. The accuracy performance of an ANN model depends on the quality and size of the provided dataset, while there is always a minimum size for an ANN to learn the given data. In this work, we are able to construct a relatively small ANN for the target task. We show the layout of the ANN model in Figure 3.9. Our model consists of four-layers $(10 + 8 + 5 + 1 = 24$ neurons$)$. We feed the input layer with the normalized coefficients, which are fully connected to the first-layer neurons. Then, the activation functions use the weighted sum on the neurons. This procedure is followed by the second, third, and output layers, while the output layer provides the predicted error. The first, second, and third layers use

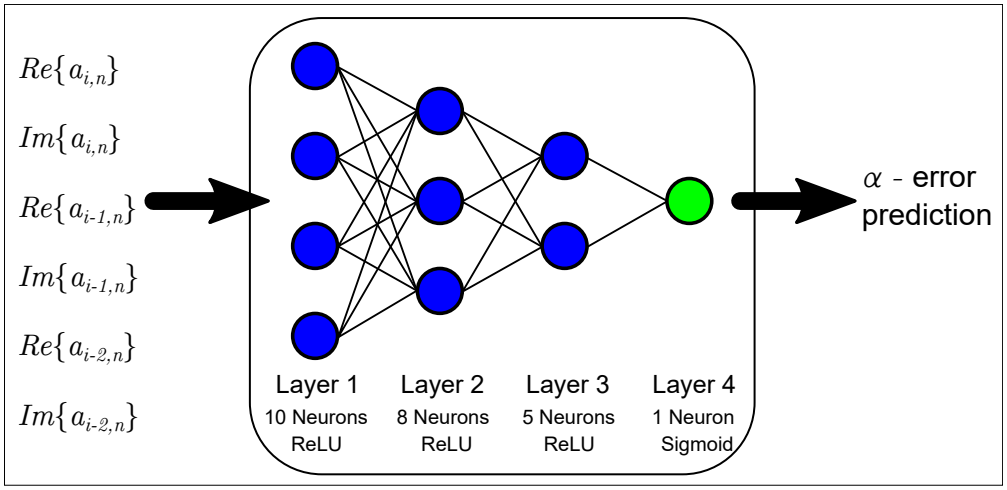

Figure 3.9: The layout of the four-layered ANN error predictor model.

rectified linear units as their activation functions, and the last layer uses the sigmoid function. The sigmoid function at the output has a crucial role since error values can be extremely large and it trims large input values to one. This property brings additional simplicity to the predicted large values. Constructed ANN model is trained via Adam optimizer [104] by using mean-absolute-error (MAE) loss function for 2000 epochs. MAE gives the current coefficient error in the prediction. Hence, minimizing MAE implies having a better preciseness on the error predictions. During the training, 95% of the complete dataset is used as the training dataset, while the rest is used for validation. The training stage requires approximately 2 hours on Google Colaboratory servers with NVidia Tesla K80 GPUs. Hence, we can reach 1 million predictions per second with the proposed ANN model on one CPU core.

We train the above mentioned ANN model on different datasets, which consist of the problems in the raw dataset. To make a wider comparison, each trained ANN using a dataset is tested on all other datasets. The MAE values obtained in these tests are shown in Figure 3.10. At first glance, we expect each ANN model to perform the most accurate result on the trained dataset. However, we observe otherwise due to the small number of layers of the ANN model. Also, the models trained with the cube and sphere datasets have the widest coverage; but they fail for the Flamme datasets as well as for the largest sphere. Such an error variation is strongly undesirable for our applications, i.e., the trained ANN should work consistently for a variety of data. The

models trained with the Flamme datasets, on the other hand, lead to a higher average MAE, but they provide more stable performances for different datasets.

As a successful dataset, we consider the results of 16λ NASA Almond and Flamme geometries together. These geometries are discretized with 55,545 and 51,669 unknowns, respectively. We randomly pick five solutions for each geometry to construct the dataset. The total processing times for the NASA Almond and Flamme solutions to build the final dataset are 50.62 minutes and 158.62 minutes, respectively. Only the first 45 iterations of each simulation are used since the most vital convergence behaviors occur at the beginning of iterative solutions. To finalize the dataset, we omit samples with current errors larger than 100%, leading to 15,303,079 current samples in the final dataset. As also shown in Figure 3.10, this set provides the best MAE levels, i.e., approximately 0.06 MAE, with a considerably small variation among datasets, in comparison to the other attempts.

3.5 Performance Comparison of ML and Manual Error Predictions

We also consider an alternative approach to predict the error in current coefficients by using a manually defined function

$$\alpha = \frac{|\boldsymbol{a}_i[n] - \boldsymbol{a}_{i-2}[n]|}{|\boldsymbol{a}_{i-2}[n]|}. \tag{3.6}$$

Manual error prediction function is compared with the ML approach on the raw dataset of the 64λ Flamme geometry. Predictors are expected to pick which basis functions reach the set error level, while the current error detection level is set to 10%. Here, we analyze the error in three different categories, i.e., total error, overestimation, and underestimation. The total errors are combinations of overestimation and underestimation errors. Overestimation of an error means that the real error value is lower than the predicted error, while underestimation means otherwise. In an overestimated error case, the predictor misses the currents to be trimmed; hence, the accuracy is not affected. In an underestimated error case, however, the predictor trims currents that are not converged yet during the iterative solution. Consequently, the main error sources in the trimming mechanism are the underestimated errors.

As shown in Figure 3.11, the ML-based error prediction is superior to the manual error prediction with a huge difference in terms of total error. The ML-based prediction

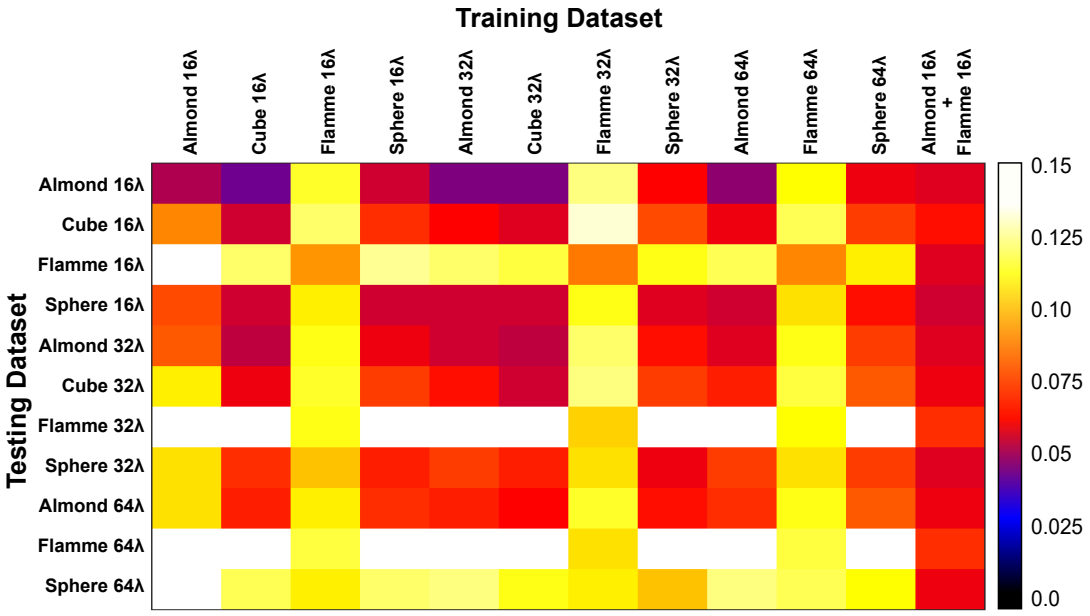

Figure 3.10: Prediction performance of the trained ANN model for different datasets. MAE values are shown as the error criteria.

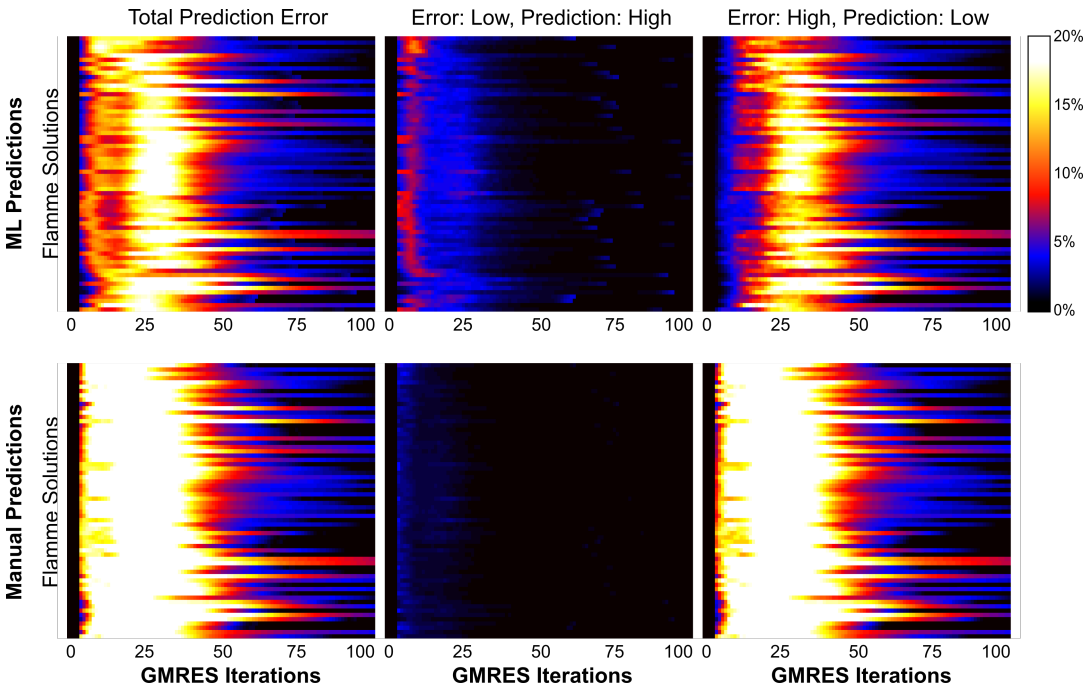

Figure 3.11: Total error, overestimated error, and underestimated error for ML-based and manual error predictions.

gives a peak error at around 15%, while the manual prediction provides more than 20% error in most of the region. Also, we note that the main error contributions of the manual prediction are from underestimated errors, which can lead to uncontrollable accuracy in the developed T-MLFMA. The errors for the ML-based prediction are of both underestimated and overestimated types. As a matter of fact, overestimated errors are mainly localized at the beginning of the iterative solutions, and they slightly reduce the efficiency of T-MLFMA.

To sum up, T-MLFMA requires an error predictor, which should be working with an error level as low as possible to accurately trim basis function. As shown in this chapter, ML-based predictors outperforms manually defined error prediction functions for trimming basis functions. Further examples on the comparison of ML-based and manual error prediction approaches are presented in the next chapter.

CHAPTER 4

NUMERICAL RESULTS

In this chapter, we present numerical simulation results using T-MLFMA for various cases. We start with the proof-of-concept simulations involving geometries with various sizes. Then, we show trimming threshold analysis and trimming counter analysis for basis and testing functions in T-MLFMA. In the fourth and fifth sections, we discuss trimming operation on near-zone interactions and the reusability of trimmed tree-structures of T-MLFMA. In the sixth section, we consider an illumination sweep for various geometries. The seventh section discusses various solutions involving different geometries and formulations. In the last section, we show the performance of T-MLFMA as a preconditioner.

4.1 Proof-of-Concept Simulations

This section covers initial simulation results for T-MLFMA as a proof-of-concept. The simulations are first performed using MLFMA to obtain reference results. Then, we use T-MLFMA for the same simulations and compare the results in terms of accuracy of surface current coefficients and far-zone scattered electric fields, as well as number of iterations, total solution time, and the last MVM time. In these simulations, we select the Flamme geometry as the target model, considering various electrical sizes of 16λ, 32λ, and 64λ. The model of the Flamme geometry is shown in Figure 4.1. The model is illuminated via a plane wave with $\theta = 90^{\circ}$, $\phi = 30^{\circ}$ propagation direction and horizontal polarization. Electromagnetic scattering problems are formulated by using CFIE (with equally weighted EFIE and MFIE) and discretized with $\lambda/10$ triangles. The numbers of unknowns are 51,669 for the 16λ problem, 202,863 for the 32λ problem, and 811,080 for the 64λ problem. The problems with

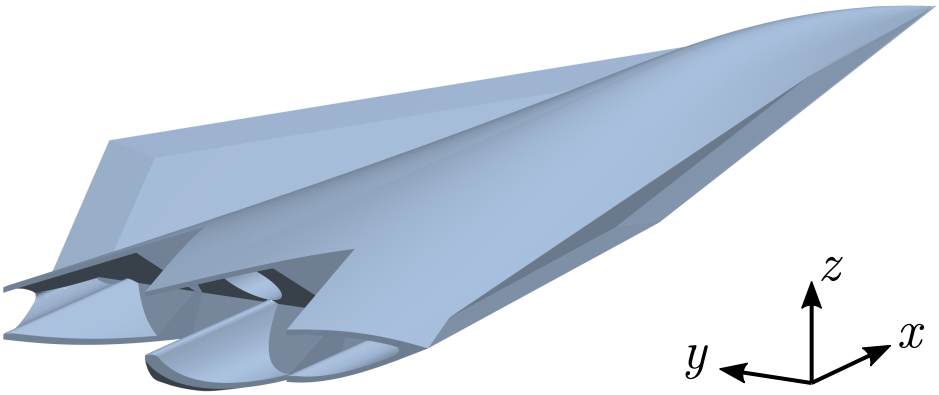

Figure 4.1: Model of the Flamme geometry.

sizes 16λ, 32λ, and 64λ are solved by using seven MLFMA levels, eight MLFMA levels, and nine MLFMA levels, respectively. The T-MLFMA simulations are performed in three different ways for each Flamme size; only basis function trimming, only testing function trimming, and both basis and testing function trimming. We also obtain trials with different trimming threshold factors, i.e., 0.1, 0.01, and 0.001. Each problem is solved both without any preconditioner and with a block-diagonal preconditioner (BDP).

The solutions in this section include two adjustments in terms of the application of T-MLFMA. The first adjustment is using the reference surface current coefficients for the basis function trimming to show the concept of T-MLFMA. In this context, the BFEP operator given in the previous chapter is altered as

$$\alpha = \frac{\left| \boldsymbol{a}_i^{ref}[n] - \boldsymbol{a}_i[n] \right|}{\left| \boldsymbol{a}_i^{ref}[n] \right|}. \tag{4.1}$$

The second adjustment is that the trimming operators count the numbers of below-threshold-error states for each basis or testing function. Specifically, the trimming operators omit basis and testing functions after the fifth below-threshold-error state. We note that this adjustment brings additional stability in T-MLFMA simulations.

Simulation results involving the Flamme geometry are listed in Table 4.1, Table 4.2, and Table 4.3 for electrical sizes of 16λ, 32λ, and 64λ, respectively. Results in the tables include surface current coefficient errors (called current error), far-zone scat-

tered electric field errors (called field error), numbers of iterations, and total solution times. Surface current coefficient errors are calculated as

$$\text{Current Error}(\%) = \frac{\left\|\boldsymbol{a}^{ref} - \boldsymbol{a}\right\|_2}{\left\|\boldsymbol{a}^{ref}\right\|_2} \times 100, \tag{4.2}$$

where $\boldsymbol{a}^{ref}$ and $\boldsymbol{a}$ are the reference and target current coefficient vectors. In this expression, $\|\cdot\|_2$ represents the L^2-norm (Euclidean distance). Far-zone scattered electric field errors are calculated as

$$\text{Farfield error}(\%) = \frac{\sqrt{\sum_{s=1}^{3600} \left\|\boldsymbol{E}_s^{ref} - \boldsymbol{E}_s\right\|_2^2}}{\sqrt{\sum_{s=1}^{3600} \left\|\boldsymbol{E}_s^{ref}\right\|_2^2}} \times 100, \tag{4.3}$$

where $\boldsymbol{E}_s^{ref}$ and $\boldsymbol{E}_s$ are reference and target far-zone scattered electric field vectors sampled at 0.1° steps in azimuth. The results show that the field errors always remain below the threshold factor. Besides, we can reduce the field errors and surface current errors by decreasing the threshold factor, which shows the error controllability of the trimming approach. Additionally, T-MLFMA becomes MLFMA for very small values of the trimming threshold factor, such as 0.0001. The results for the number of iterations show impressive acceleration, i.e., the number of iterations is reduced by 2.48 times for the 16λ problem (2.28 times when BDP is used), 4.80 times for the 32λ problem (3.85 times when BDP is used), and 5.56 times for the 64λ problem (4.25 times when BDP is used). Hence, the reduction in the number of iterations is higher for electrically large problems. Using T-MLFMA, the solution time is reduced by 2.86 times for the 16λ problem (2.89 times when BDP is used), 6.43 times for the 32λ problem (5.44 times when BDP is used), and 7.29 times for the 64λ problem (5.17 times when BDP is used), compared to the reference MLFMA simulations. The reduction in the overall solution time is higher than the reduction in the number of iterations since the trimming process reduces the MVM time per iteration as the solution continues.

Figures 4.2, 4.3, 4.4, 4.5, 4.6, and 4.7 present the bistatic far-zone electric field intensity on the x-y plane (see Figure 4.1 for the coordinates) obtained by using the conventional MLFMA and the proposed T-MLFMA with basis and testing function trimming. The far-zone electric field intensity plots show good consistency between T-MLFMA and MLFMA. These figures also depict the iterative solutions (residual errors with respect to flexible GMRES iterations), where the faster convergence of

T-MLFMA is remarkable. The figures further illustrate the ratios of the included basis/testing functions in MVMs by T-MLFMA (dropping as the iterations continue), as well as the processing times per MVM. We observe that the MVM time from the first iteration to the last iteration clearly decreases as the residual error drops to below 0.001.

Table 4.1: Simulation results for a scattering problem involving the Flamme geometry with an electrical size of 16λ.

Method	**Trimming Error**	**PC**	**Current Error (%)**	**Far-Field Error (%)**	**Number of Iter.**	**Solution Time (h)**
Ref.	-	-	-	-	221	0.86
Ref.	-	BDP	-	-	151	0.55
Basis T.	0.001	-	0.06	0.04	220	0.89
Basis T.	0.01	-	1.34	0.79	202	0.79
Basis T.	0.1	-	10.4	4.46	153	0.55
Basis T.	0.001	BDP	0.00	0.00	151	0.62
Basis T.	0.01	BDP	0.93	0.49	145	0.59
Basis T.	0.1	BDP	9.20	4.08	108	0.40
Test T.	0.001	-	0.11	0.04	219	0.86
Test T.	0.01	-	6.24	0.66	177	0.67
Test T.	0.1	-	42.1	4.73	93	0.32
Test T.	0.001	BDP	0.02	0.01	151	0.56
Test T.	0.01	BDP	5.27	0.66	116	0.43
Test T.	0.1	BDP	40.1	4.66	67	0.21
B+T T.	0.001	-	0.16	0.04	218	0.90
B+T T.	0.01	-	5.95	0.68	175	0.69
B+T T.	0.1	-	42.1	4.88	89	0.30
B+T T.	0.001	BDP	0.02	0.01	151	0.56
B+T T.	0.01	BDP	5.27	0.67	115	0.42
B+T T.	0.1	BDP	40.1	4.81	66	0.19

Table 4.2: Simulation results for a scattering problem involving the Flamme geometry with an electrical size of 32λ.

Method	**Trimming Error**	**PC**	**Current Error (%)**	**Far-Field Error (%)**	**Number of Iter.**	**Solution Time (h)**
Ref.	-	-	-	-	389	6.89
Ref.	-	BDP	-	-	274	4.90
Basis T.	0.001	-	0.07	0.04	388	6.49
Basis T.	0.01	-	2.37	0.82	351	5.77
Basis T.	0.1	-	14.4	2.39	217	2.97
Basis T.	0.001	BDP	0.04	0.02	274	4.51
Basis T.	0.01	BDP	3.19	0.48	262	4.22
Basis T.	0.1	BDP	14.9	2.61	175	2.44
Test T.	0.001	-	0.32	0.04	386	6.81
Test T.	0.01	-	19.3	1.46	234	4.00
Test T.	0.1	-	31.3	2.60	85	1.26
Test T.	0.001	BDP	0.07	0.02	274	4.89
Test T.	0.01	BDP	15.0	1.00	202	3.53
Test T.	0.1	BDP	29.0	2.41	71	1.06
B+T T.	0.001	-	0.33	0.04	385	6.02
B+T T.	0.01	-	19.4	1.49	231	3.61
B+T T.	0.1	-	31.3	2.62	81	1.07
B+T T.	0.001	BDP	0.08	0.03	274	4.39
B+T T.	0.01	BDP	15.4	1.09	199	3.17
B+T T.	0.1	BDP	29.0	2.75	71	0.90

Table 4.3: Simulation results for a scattering problem involving the Flamme geometry with an electrical size of 64λ.

Method	**Trimming Error**	**PC**	**Current Error (%)**	**Far-Field Error (%)**	**Number of Iter.**	**Solution Time (h)**
Ref.	-	-	-	-	434	31.9
Ref.	-	BDP	-	-	289	20.4
Basis T.	0.001	-	0.29	0.06	431	28.9
Basis T.	0.01	-	1.71	0.38	333	21.9
Basis T.	0.1	-	6.70	2.16	199	11.4
Basis T.	0.001	BDP	0.37	0.23	288	19.9
Basis T.	0.01	BDP	1.21	0.35	229	15.9
Basis T.	0.1	BDP	6.94	2.08	144	8.86
Test T.	0.001	-	1.00	0.08	381	27.9
Test T.	0.01	-	8.87	0.84	220	15.2
Test T.	0.1	-	32.9	3.16	82	5.10
Test T.	0.001	BDP	0.83	0.25	257	18.8
Test T.	0.01	BDP	7.17	0.77	171	12.1
Test T.	0.1	BDP	26.2	2.09	69	4.30
B+T T.	0.001	-	0.92	0.09	382	25.0
B+T T.	0.01	-	9.00	0.85	217	14.2
B+T T.	0.1	-	32.9	3.09	78	4.40
B+T T.	0.001	BDP	0.89	0.29	256	18.0
B+T T.	0.01	BDP	7.15	0.80	169	11.5
B+T T.	0.1	BDP	26.2	2.32	68	3.90

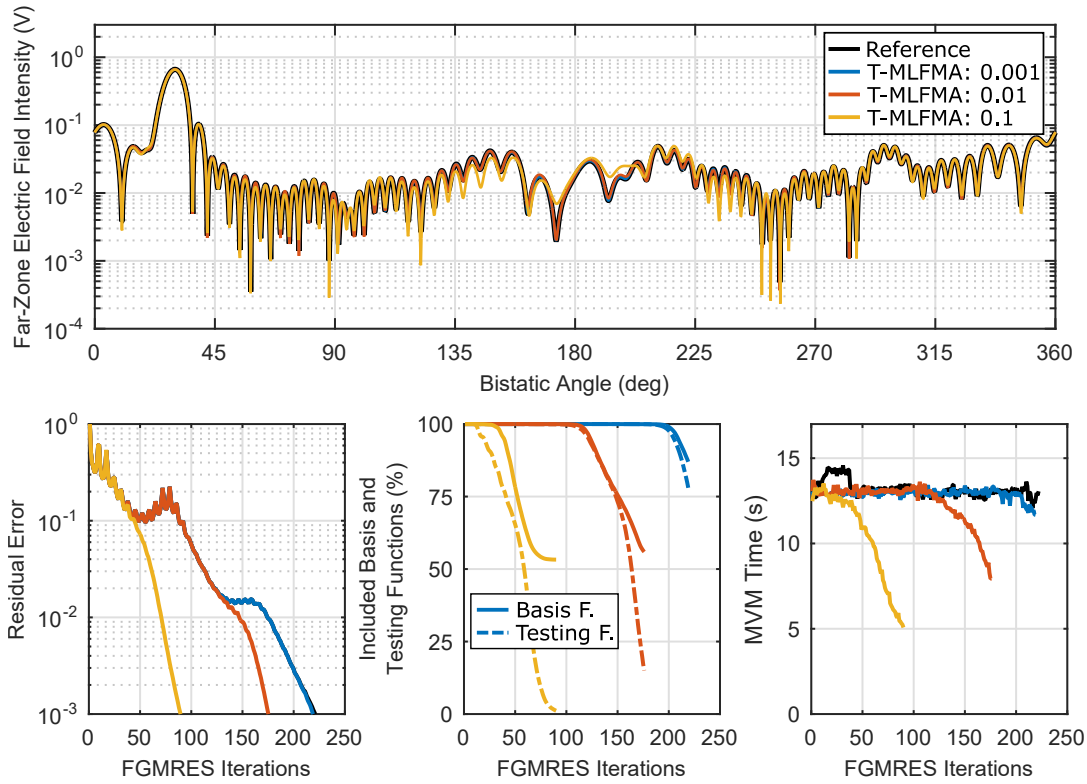

Figure 4.2: Solutions of a scattering problem involving the Flamme geometry with an electrical size of 16λ. Solutions are not accelerated with any preconditioner.

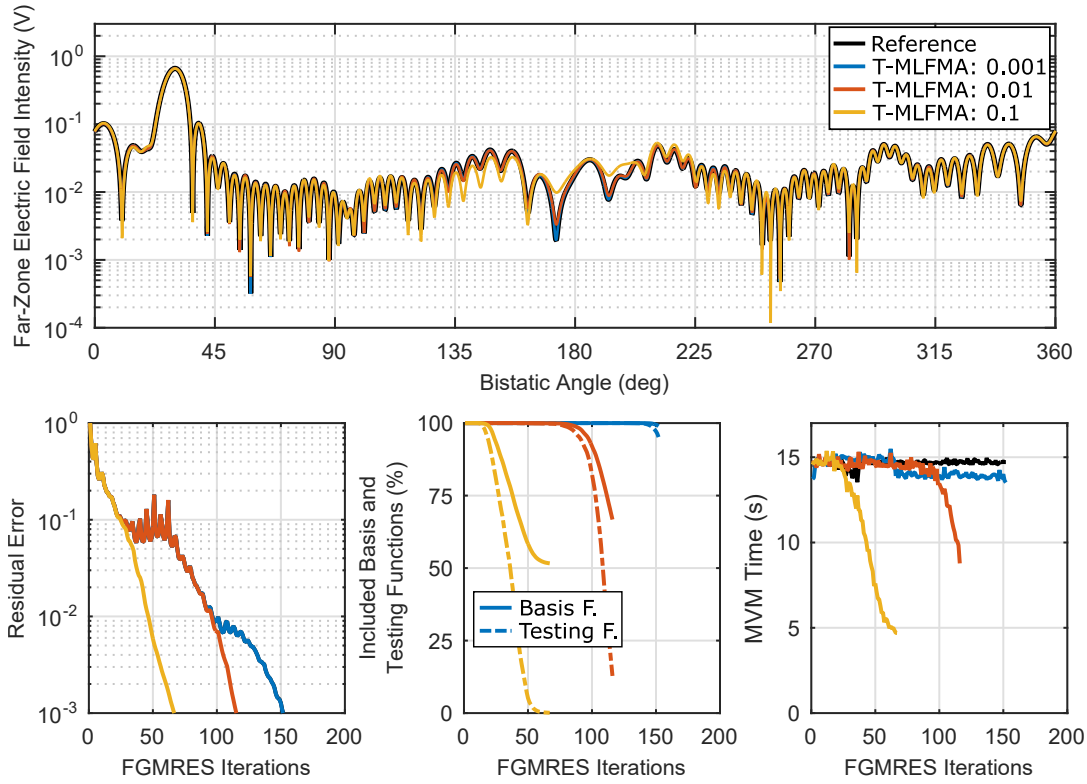

Figure 4.3: Solutions of a scattering problem involving the Flamme geometry with an electrical size of 16λ. Solutions are accelerated with the BDP preconditioner.

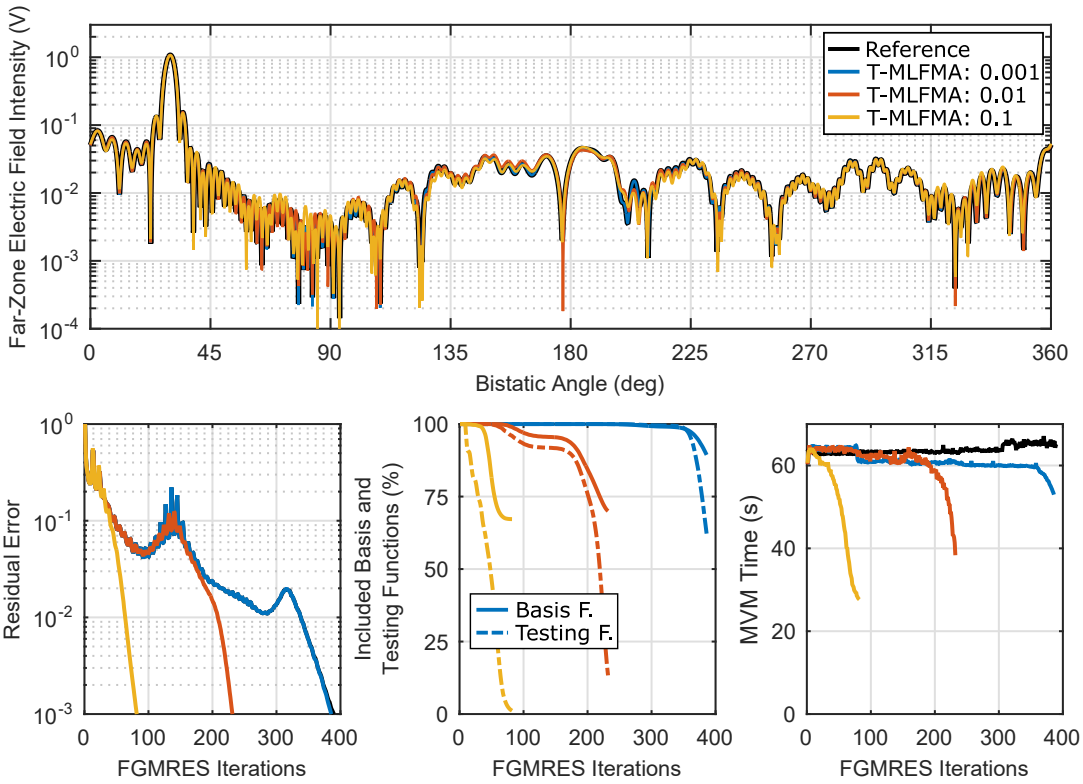

Figure 4.4: Solutions of a scattering problem involving the Flamme geometry with an electrical size of 32λ. Solutions are not accelerated with any preconditioner.

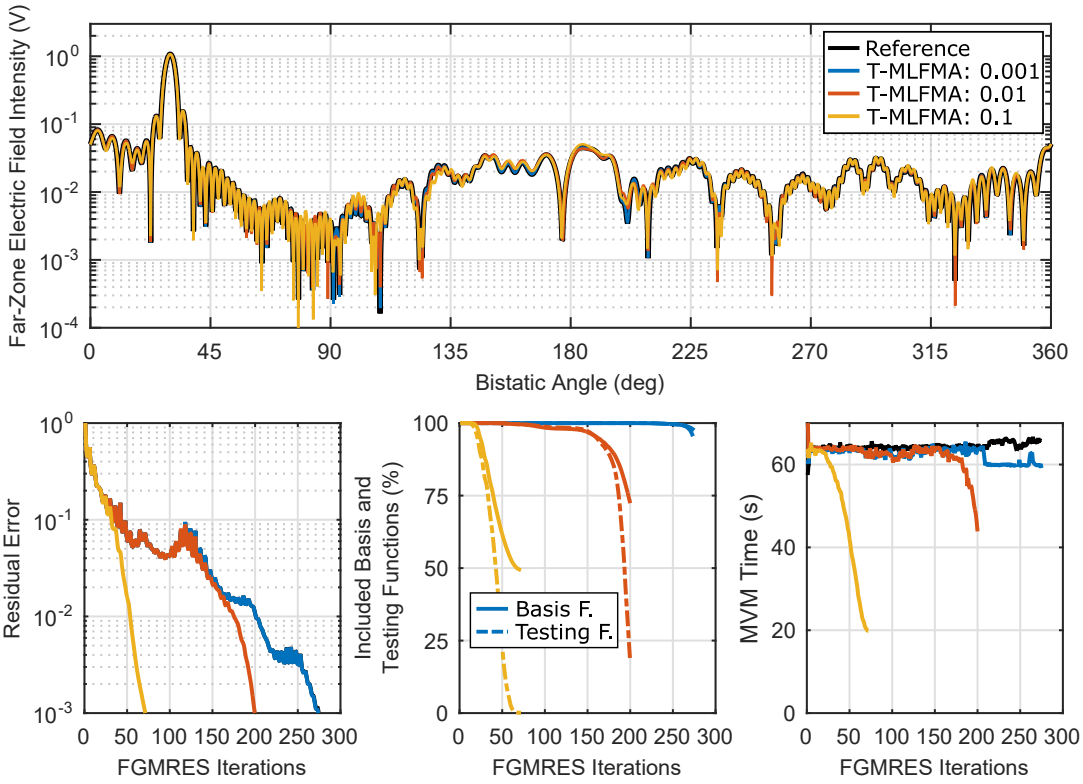

Figure 4.5: Solutions of a scattering problem involving the Flamme geometry with an electrical size of 32λ. Solutions are accelerated with the BDP preconditioner.

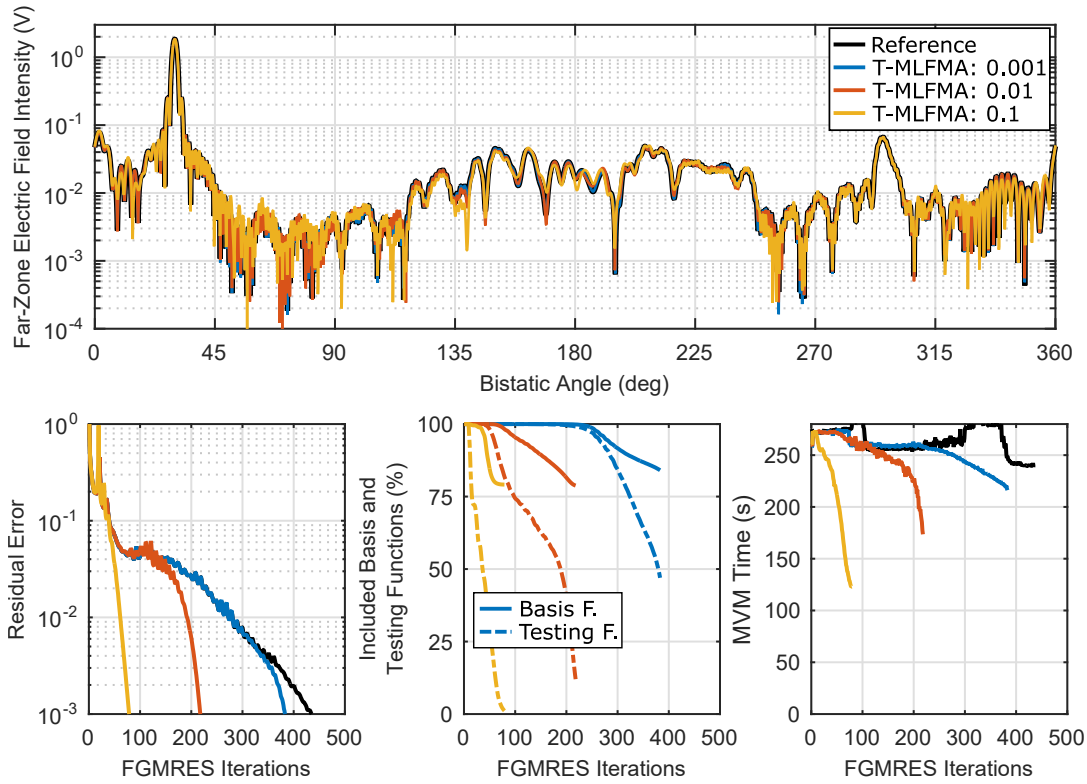

Figure 4.6: Solutions of a scattering problem involving the Flamme geometry with an electrical size of 64λ. Solutions are not accelerated with any preconditioner.

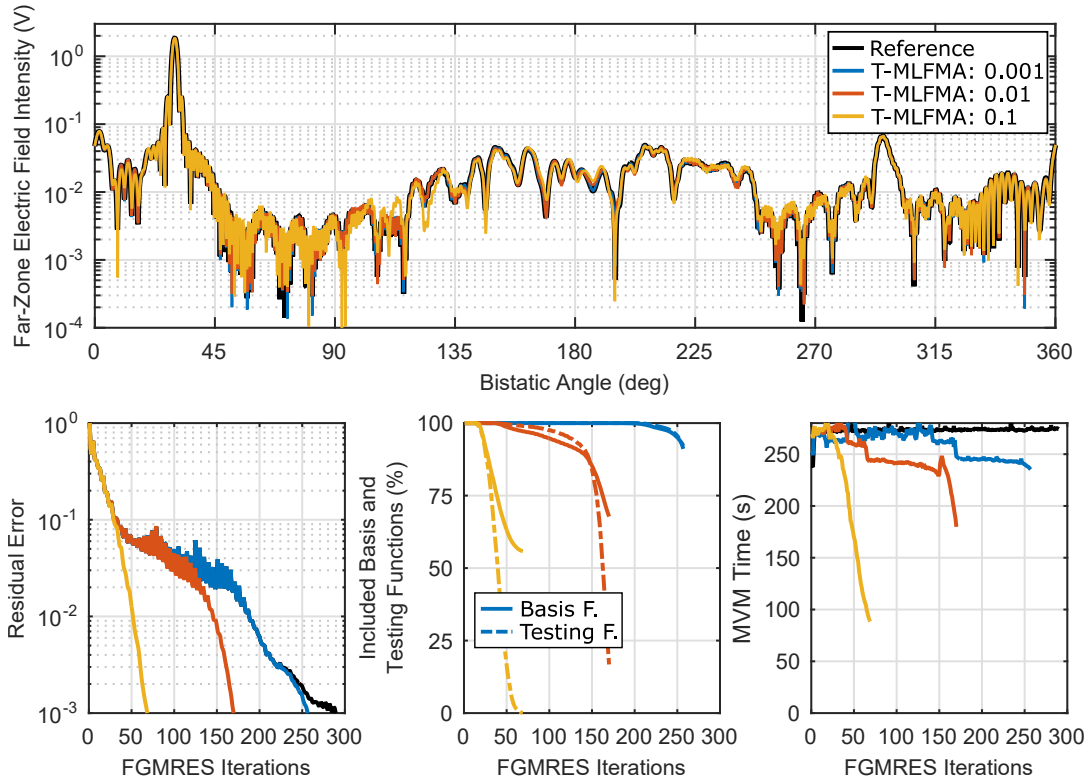

Figure 4.7: Solutions of a scattering problem involving the Flamme geometry with an electrical size of 64λ. Solutions are accelerated with the BDP preconditioner.

4.2 Trimming Threshold Analysis

In this section, simulations with T-MLFMA for different trimming threshold levels (0.2, 0.1, 0.05, and 0.01) are presented. Basis function and testing function trimming operators are separately applied with a counter value of 1, where BFEP is applied with both ML and manual approaches. The Flamme geometry with an the electrical size of 64λ is used as the target, where the geometry is illuminated by a plane wave with propagation direction $\theta = 90^\circ$ and $\phi = 30^\circ$, and with horizontal polarization. Backscattering errors shown in this section are calculated as in Equation 4.3 by considering $\pm 10^\circ$ range at around the backscattering angle.

The simulation results obtained by T-MLFMA using basis function trimming with the ML approach are shown in Table 4.4. Surface current errors, far-zone electric field errors, and backscattering field errors are consistently reduced as the trimming threshold is decreased. The far-zone electric field errors are considerably below the threshold values, while the backscattering errors can be reduced in a controllable manner. Using T-MLFMA can also reduce the number of iterations as we increase the trimming threshold, while multiple times of speedup can be achieved in terms of the solution time. In Figure 4.8, we show the far-zone scattered electric field values with respect to the bistatic angle in the azimuth plane. In general, the fields obtained with T-MLFMA match well with the reference fields obtained with MLFMA. We obtain a decent match in the backscattering range, even with high trimming thresholds, such as 0.2. Figure 4.8 also depicts the iterative solutions (residual errors with respect to flexible GMRES iterations), where the faster convergence of T-MLFMA is remarkable. Figure 4.8 further illustrates the ratios of the included basis/testing functions in the MVMs by T-MLFMA, which are dropping as the iterations continue, as well as the processing times per MVM. T-MLFMA effectively reduces the number of active basis functions such that the MVM time per iteration at the end of the solution reaches the half of a full MVM time (for the trimming threshold values of 0.2 and 0.1).

The solution details of simulation results obtained by T-MLFMA using basis function trimming with the manual approach are shown in Table 4.5. We observe that the surface current errors, far-zone electric field errors, and backscattering field errors

Table 4.4: Details of the simulation results obtained by T-MLFMA with the ML-based basis function trimming for a scattering problem involving the Flamme geometry (64λ).

Method	**Trimming Error**	**Current Error (%)**	**Far-Field Error (%)**	**Backsca. Error (%)**	**Number of Iter.**	**Solution Time (h)**
Ref.	-	-	-	-	289	21.9
Basis (ML)	0.01	7.49	0.89	7.57	171	12.7
Basis (ML)	0.05	22.8	2.01	10.7	89	6.02
Basis (ML)	0.1	25.8	3.10	15.6	77	4.92
Basis (ML)	0.2	30.8	5.69	35.5	68	4.09

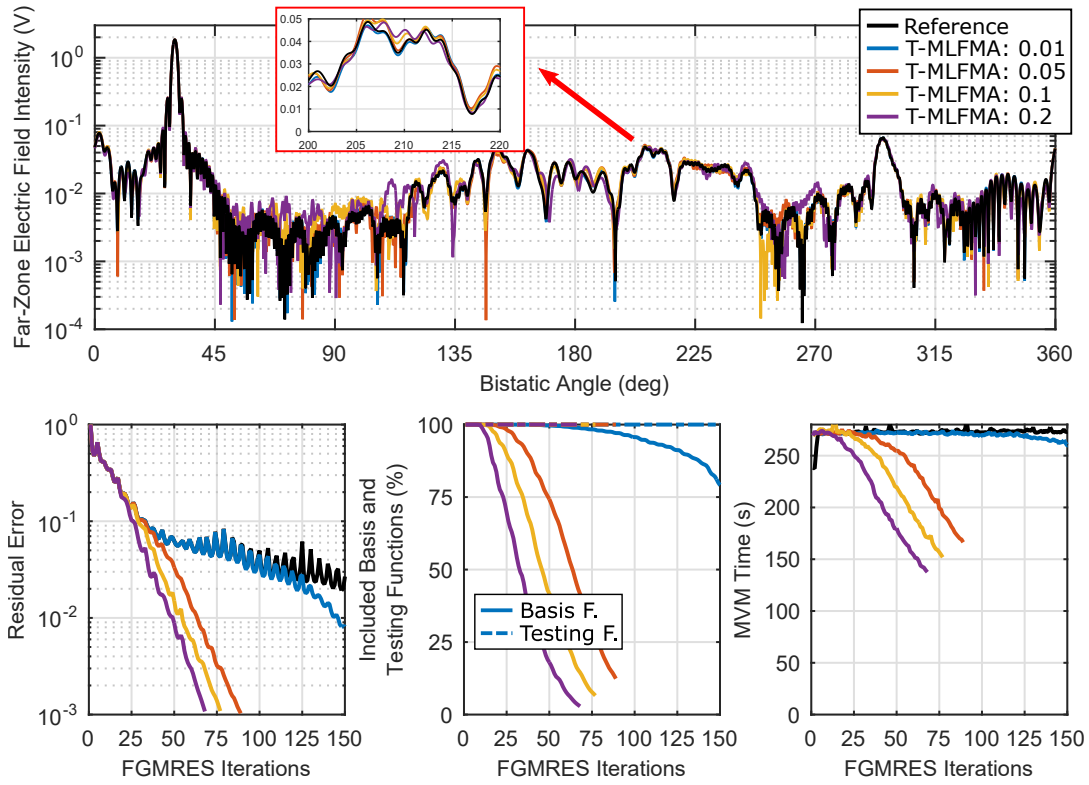

Figure 4.8: Solutions of a scattering problem involving the Flamme geometry with an electrical size of 64λ. Basis function trimming with the ML approach is applied.

Table 4.5: Details of the simulation results obtained by T-MLFMA with the manual basis function trimming for a scattering problem involving the Flamme geometry (64λ).

Method	**Trimming Error**	**Current Error (%)**	**Far-Field Error (%)**	**Backsca. Error (%)**	**Number of Iter.**	**Solution Time (h)**
Ref.	-	-	-	-	289	21.9
Basis (Man)	0.01	23.2	1.98	11.0	87	5.84
Basis (Man)	0.05	30.4	4.84	28.1	66	3.99
Basis (Man)	0.1	35.9	7.43	49.2	59	3.34
Basis (Man)	0.2	42.9	10.3	69.0	55	2.85

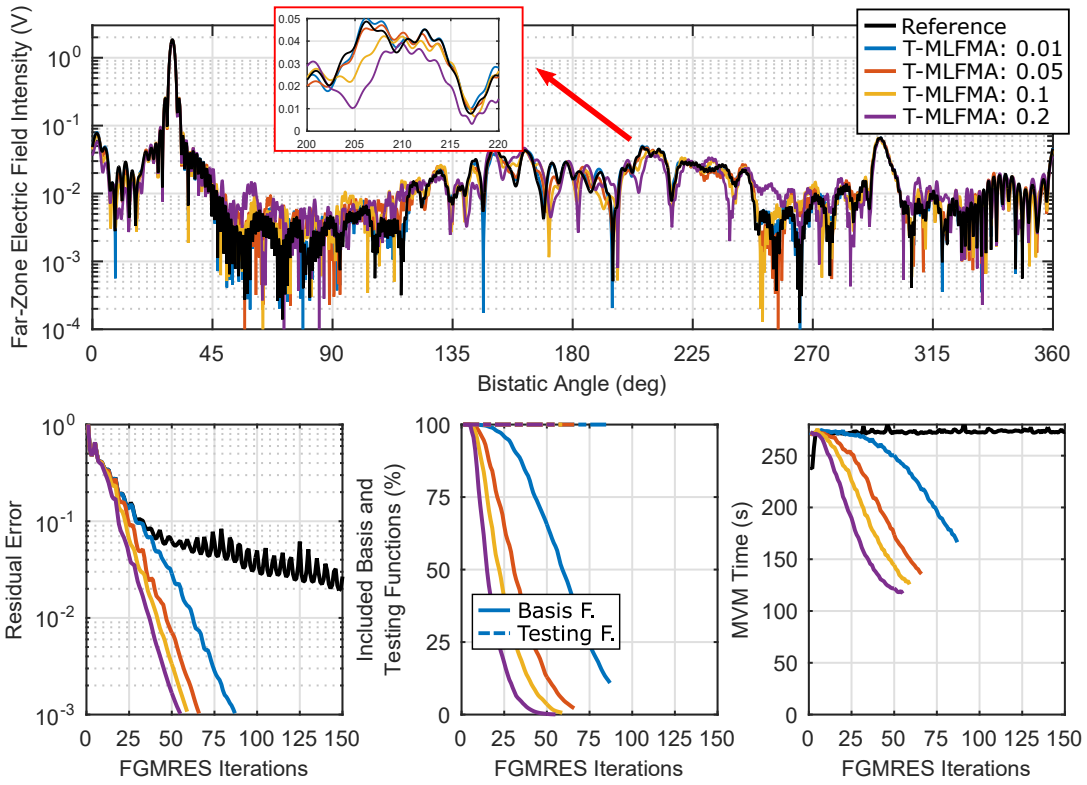

Figure 4.9: Solutions of a scattering problem involving the Flamme geometry with an electrical size of 64λ. Basis function trimming with the manual approach is applied.

are reduced as the trimming threshold is decreased, while the reduction values are significantly worse than those obtained with the ML-based approach. The far-zone electric field errors and the backscattering errors are almost twice as the corresponding results of the ML-based approach. In addition, the error does not seem to be controllable with the manual approach. In Figure 4.9, we show the far-zone scattered electric field values with respect to the bistatic angle in the azimuth plane. Figure 4.9 further illustrates the ratios of the included basis/testing functions in the MVMs by T-MLFMA, as well as the processing times per MVM. The basis function elimination in T-MLFMA for this solution set is even faster than that of the previous set, while the MVM time at the end of the solution reaches below the half of the full MVM time. On the other hand, although the speedup levels are promising, T-MLFMA with manual trimming requires at least 0.05 threshold level (equivalent to 0.2 threshold level with the ML-based trimming) for an acceptable accuracy.

The simulation results obtained by T-MLFMA using testing function trimming are shown in Table 4.6. The surface current errors, far-zone electric field errors, and backscattering field errors, which consistently drop with the trimming threshold, are similar to the results obtained by using the ML-based basis function trimming. The far-zone electric field errors are considerably below the given threshold values, while the backscattering errors are observed to be reduced in a controllable manner. Using T-MLFMA can also reduce the number of iterations as we increase the trimming threshold, while multiple times of speedup can be achieved in terms of the solution time. In Figure 4.10, we show the far-zone scattered electric field values with respect to the bistatic angle in the azimuth plane. The fields obtained with T-MLFMA match well with the reference fields obtained with MLFMA, where its stability is even better than the previous two sets of solutions (basis function trimming). To obtain an acceptable accuracy in the backscattering range, we need to use at least a trimming threshold of 0.1. Figure 4.10 also depicts the iterative solutions, ratios of the included basis/testing functions in MVMs, and processing times per MVM. The MVM time per iteration can be lowered to less than 50% of the full MVM time at the late stages of the solution.

Table 4.6: Details of the simulation results obtained by T-MLFMA with testing function trimming for a scattering problem involving the Flamme geometry (64λ).

Method	**Trimming Error**	**Current Error (%)**	**Far-Field Error (%)**	**Backsca. Error (%)**	**Number of Iter.**	**Solution Time (h)**
Ref.	-	-	-	-	289	21.9
Testing	0.01	16.5	1.27	7.95	114	8.28
Testing	0.05	26.9	2.19	14.9	68	4.28
Testing	0.1	32.0	4.20	33.3	62	3.57
Testing	0.2	40.4	7.79	67.6	55	2.98

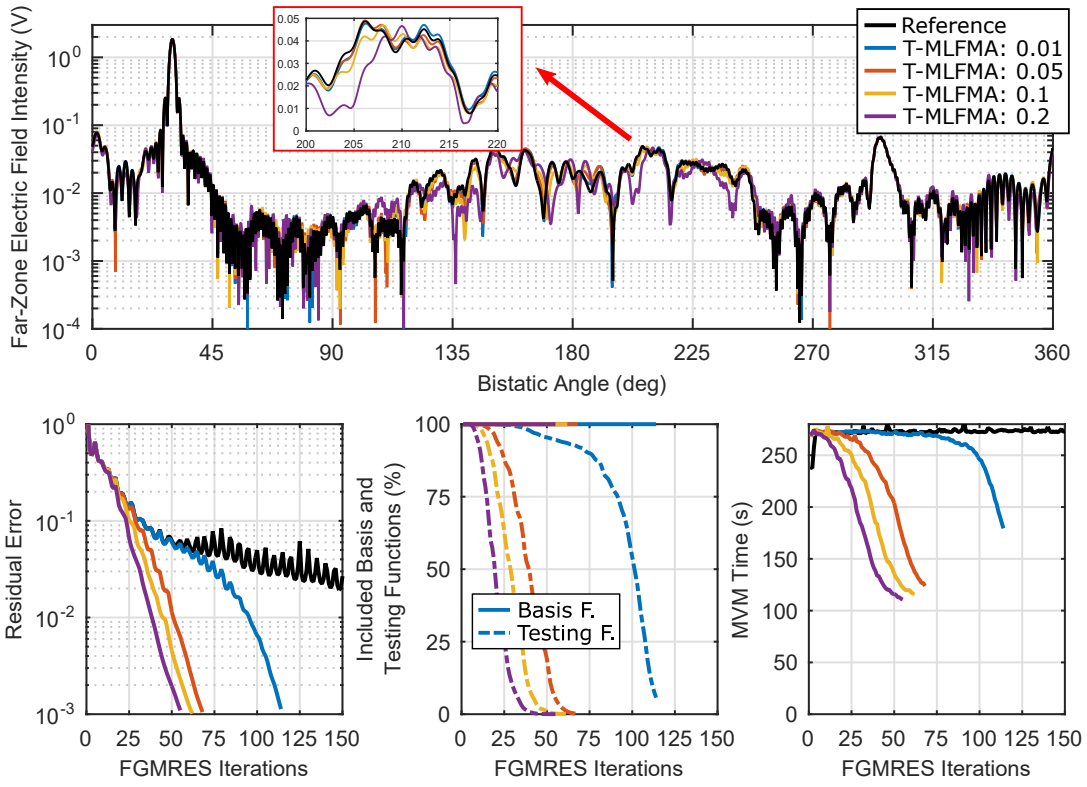

Figure 4.10: Solutions of a scattering problem involving the Flamme geometry with an electrical size of 64λ. Testing function trimming is applied.

4.3 Trimming Counter Analysis

The trimming process affects the accuracy of MVMs as it is based on omitting basis and/or testing functions. Trimming basis and testing functions, performed via estimators, cause errors due to mispredictions. The effect of these mispredictions can be reduced by allowing the basis and/or testing functions to continue interacting for a certain number of iterations after a trimming decision. The number of iterations after a trimming decision can be determined by a counter. In this section, we present simulation results obtained with this kind of a counter applied in the trimming operation. We particularly consider results by using T-MLFMA with basis function trimming and testing function trimming separately for various counter values, while we apply both ML-based and manual-based approaches for BFEP. The trimming error threshold is set as 0.1 for both basis and testing functions. The Flamme geometry with an electrical size of 64λ is used as the target, while the geometry is illuminated by a plane wave with propagation direction $\theta = 90^\circ$ and $\phi = 30^\circ$, and with horizontal polarization.

The simulation results obtained by T-MLFMA using basis function trimming with the ML approach are shown in Table 4.7. The surface current errors, far-zone electric field errors, and backscattering field errors are consistently reduced as the trimming counter is decreased. The far-zone electric field errors are considerably below the threshold values, and the results are noticeably stable. Note that, the limit case of the increased counter size is the full MLFMA, and we can observe that the convergence behavior shows this characteristics. T-MLFMA still provides multiple times of speedup in terms of the solution time, even for a counter value of five. We also observe that the total solution time increases by approximately 13% for the trimming counter value of five in comparison to the trimming counter value of one, while the backscattering error improves by almost 20%. In Figure 4.11, we show the far-zone scattered electric field values with respect to the bistatic angle in the azimuth plane. The field values obtained with T-MLFMA demonstrate converging behavior towards the reference field values. We obtain a decent match in the backscattering range, even with a base trimming counter value of zero. Figure 4.11 also depicts the iterative solutions (residual errors with respect to the flexible GMRES iterations), where

Table 4.7: Details of the simulation results obtained by T-MLFMA with the ML-based basis function trimming using different trimming counter values for a scattering problem involving the Flamme geometry (64λ).

Method	**Counter**	**Current Error (%)**	**Far-Field Error (%)**	**Backsca. Error (%)**	**Number of Iter.**	**Solution Time (h)**
Ref.	-	-	-	-	289	21.9
Basis (ML)	0	27.5	3.92	19.8	74	4.64
Basis (ML)	1	25.8	3.10	15.6	77	4.99
Basis (ML)	2	25.0	2.76	14.1	80	5.22
Basis (ML)	3	24.5	2.53	13.6	82	5.38
Basis (ML)	4	24.0	2.46	13.7	84	5.55
Basis (ML)	5	23.6	2.36	12.9	84	5.68

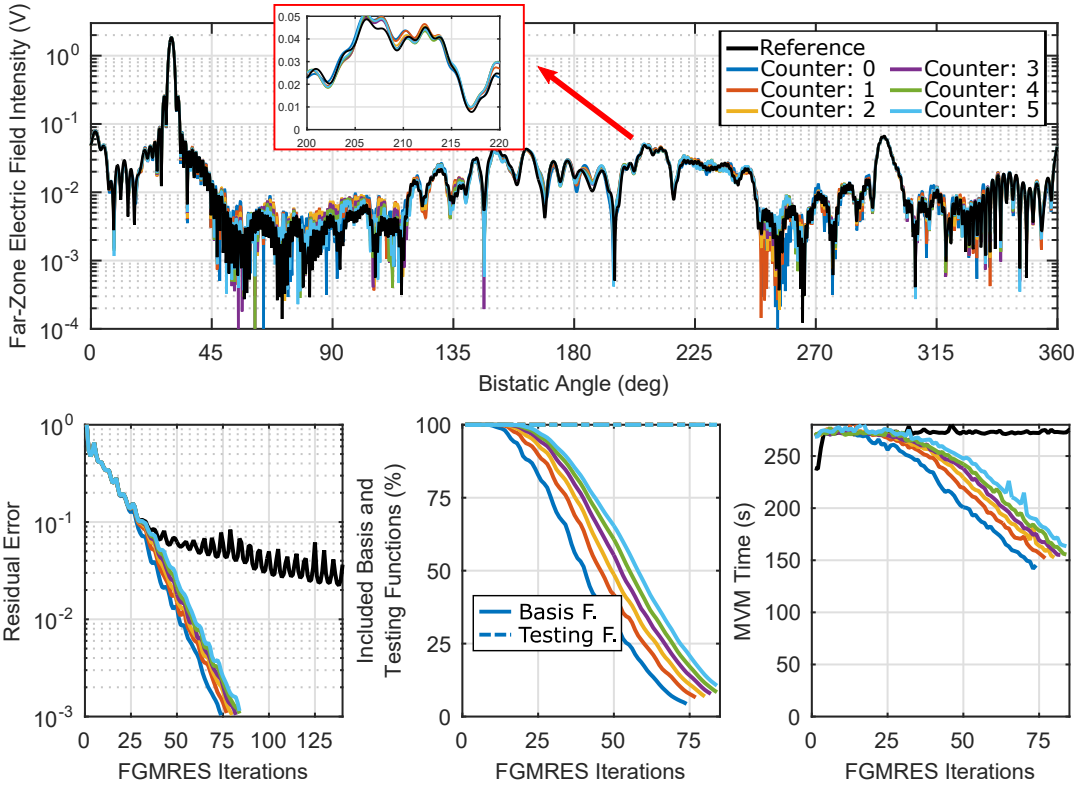

Figure 4.11: Solutions of a scattering problem involving the Flamme geometry with an electrical size of 64λ. ML-based basis function trimming with different trimming counter values is applied.

the convergence of T-MLFMA is clearly faster than the convergence of the reference MLFMA. Figure 4.11 further illustrates the ratios of the included basis/testing functions in the MVMs by T-MLFMA, which clearly reach below the 10% level as the iterations continue. T-MLFMA effectively reduces the number of active basis functions such that the MVM time per iteration at the end of the solution reaches the half of a full MVM time (for the trimming counter values of 0 and 1).

The simulation results obtained by T-MLFMA using basis function trimming with the manual approach are shown in Table 4.8. The surface current errors, far-zone electric field errors, and backscattering field errors, which are generally high for low values of the trimming counter, can gradually be reduced as the trimming counter is decreased. The far-zone electric field errors and backscattering errors are clearly higher than the values obtained with the ML-based approach. Although the manual-based approach follows the limit case (becoming the regular MLFMA for sufficiently large trimming counter values), this approach does not provide a reliable operation since its stability is not predictable. The base limit value of zero for this approach fails since all basis functions are omitted in a few iterations, which clearly shows the lack of controllability for the manual basis function trimming approach. In Figure 4.12, we show the far-zone scattered electric field values with respect to the bistatic angle in the azimuth plane. The fields obtained with T-MLFMA present a slowly converging behavior with respect to the reference fields obtained with MLFMA after the third trimming counter. Figure 4.12 also depicts the iterative solutions (residual errors for flexible GMRES iterations), where the T-MLFMA convergence is clearly faster than the convergence of the reference solution. Figure 4.12 further illustrates the ratios of the included basis/testing functions in MVMs by T-MLFMA, which are reaching below the 3% level as the iterations continue. The basis function elimination of T-MLFMA for this solution set is even faster than elimination in the previous set and the MVM time at the end of the solution reaches below the half of the MVM time of the reference solution.

The simulation results obtained by T-MLFMA using testing function trimming are shown in Table 4.9. The surface current errors, far-zone electric field errors, and backscattering field errors are consistently reduced as the trimming counter is increased. The far-zone electric field error is a bit high for the base counter value of

Table 4.8: Details of the simulation results obtained by T-MLFMA with the manual basis function trimming using different trimming counter values for a scattering problem involving the Flamme geometry (64λ).

Method	**Counter**	**Current Error (%)**	**Far-Field Error (%)**	**Backsca. Error (%)**	**Number of Iter.**	**Solution Time (h)**
Ref.	-	-	-	-	289	21.9
Basis (Man)	0	76.1	61.9	120	42	1.44
Basis (Man)	1	35.9	7.43	49.2	59	3.36
Basis (Man)	2	31.5	5.84	38.5	65	3.83
Basis (Man)	3	29.7	4.88	28.8	68	4.09
Basis (Man)	4	28.5	4.22	23.7	69	4.23
Basis (Man)	5	27.6	3.71	19.7	71	4.36

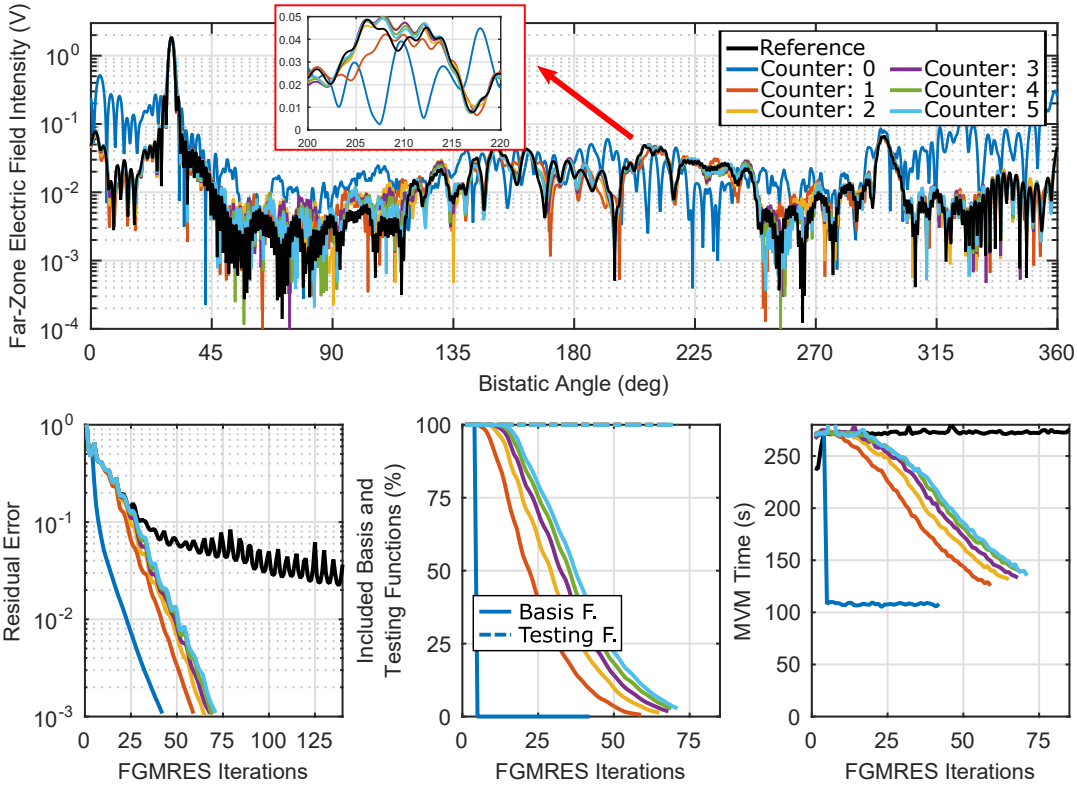

Figure 4.12: Solutions of a scattering problem involving the Flamme geometry with an electrical size of 64λ. Manual basis function trimming with different trimming counter values is applied.

Table 4.9: Details of the simulation results obtained by T-MLFMA with testing function trimming using different trimming counter values for a scattering problem involving the Flamme geometry (64λ).

Method	**Counter**	**Current Error (%)**	**Far-Field Error (%)**	**Backsca. Error (%)**	**Number of Iter.**	**Solution Time (h)**
Ref.	-	-	-	-	289	21.9
Testing	0	40.2	7.17	62.0	56	3.10
Testing	1	32.0	4.20	33.3	62	3.59
Testing	2	29.3	3.03	22.9	64	3.83
Testing	3	27.9	2.55	18.0	66	4.08
Testing	4	26.9	2.28	15.3	67	4.18
Testing	5	26.2	2.09	13.2	69	4.40

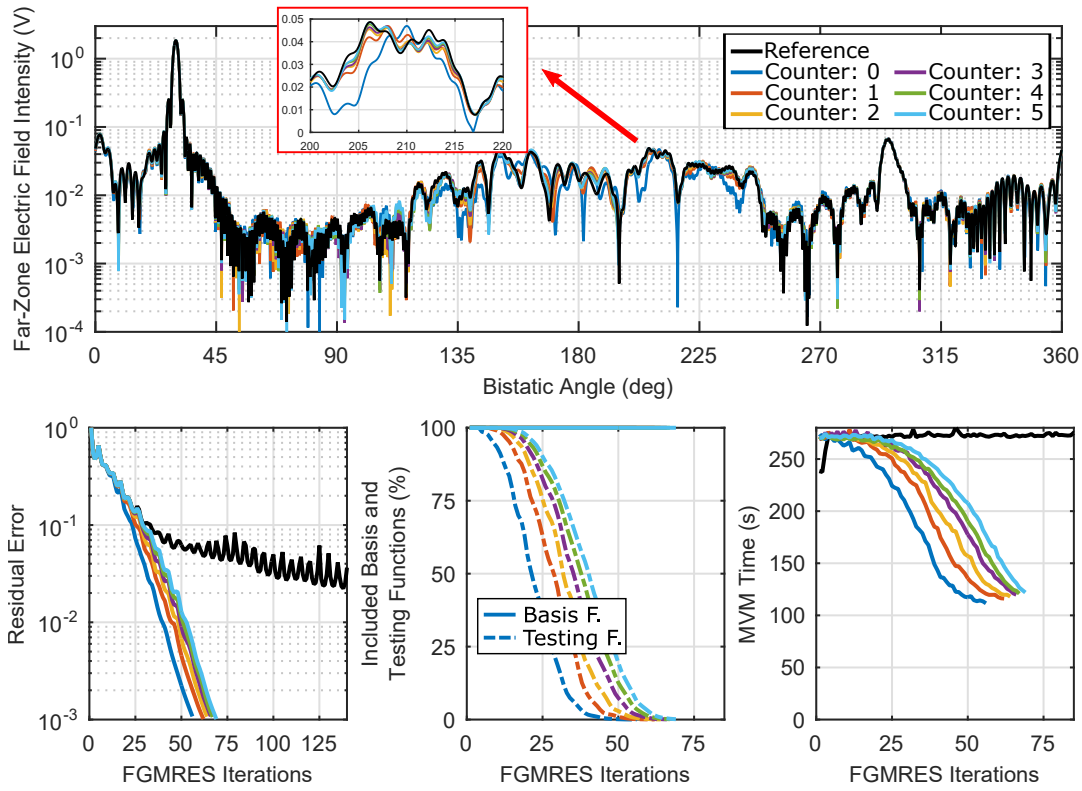

Figure 4.13: Solutions of a scattering problem involving the Flamme geometry with an electrical size of 64λ. Testing function trimming with different trimming counter values is applied.

zero (but still below the threshold), but it gets improved rapidly, and the solutions show noticeably stable results. T-MLFMA for testing function presents a faster convergence behavior than the previous solution sets. T-MLFMA still provides multiple times of speedup in terms of solution time, while its acceleration is better than the basis function trimming. However, we note that basis and testing function trimming must be implemented together to obtain the peak level of acceleration. We also observe that the total solution time increases by around 12% for the trimming counter value of five compared to the trimming counter value of one, while the backscattering error improves by almost 60%. ML-based basis function trimming and testing function trimming procedures become compatible for the counter value of five since their error levels coincide. In Figure 4.13, we show the far-zone scattered electric field values with respect to the bistatic angle in the azimuth plane. The field values obtained with T-MLFMA present a rapidly converging behavior with respect to the reference fields obtained with MLFMA. We obtain a decent match in the backscattering range, starting from the trimming counter value of one. Figure 4.13 also depicts the iterative solutions (residual errors for flexible GMRES iterations), where the T-MLFMA convergence is straight and sharp for all values of the counter. Figure 4.13 further illustrates the ratios of the included basis/testing functions in MVMs by T-MLFMA, which reach the bottom level after the second half of the iterative solution. T-MLFMA reduces the basis functions such that the MVM time per iteration is lowered to less than the half of the full MVM time at the late stages of the solutions.

4.4 Trimming Near-Zone Interactions

In this section, we show the simulation results for an extended trimming process, which also omits near-zone interactions, in addition to far-zone interactions. During iterative solutions, as the excluded basis and testing functions are selected, the corresponding columns and rows of the near-zone interaction matrix are omitted, while the diagonal elements are always kept. The physical interpretation of this approach is extending the trimming operation to short-distance interactions.

This section includes the solution of two geometries, the NASA Almond and the Flamme, each with 64λ electrical size. Model of the NASA Almond geometry is shown in Figure 4.14. The models are discretized with $\lambda/10$ triangles, leading to

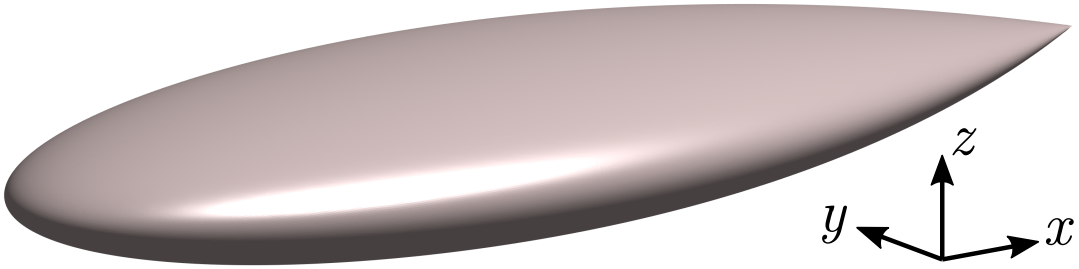

Figure 4.14: Model of the NASA Almond geometry.

893,727 and 811,080 unknowns for the NASA Almond and the Flamme, respectively. We obtain simulation results by using T-MLFMA with both basis function and testing function trimming operations, while we consider the ML-based approach for BFEP. The results are obtained for different error thresholds, while the trimming counter value is set to one.

We illuminate the NASA Almond geometry by a plane wave from two different angles, i.e., ($\theta = 90°$, $\phi = 30°$) and ($\theta = 90°$, $\phi = 210°$). The corresponding simulation results are shown in Figure 4.15a and Figure 4.15b, respectively. The figures depict the iterative solutions for different error threshold values, where the iterative convergence fails for high error threshold values in T-MLFMA. We are unable to make a comparison with the reference MLFMA result due to the non-convergent behavior of the T-MLFMA solutions. The figures also show the ratios of the included basis/testing functions in MVMs by T-MLFMA. A stable elimination is observed for the basis function. Nevertheless, the elimination of the testing functions starts to stagnate after a sharp drop, which triggers a divergence or stagnation of the iterative solution.

We illuminate the Flamme geometry by a plane wave from two different angles, i.e., ($\theta = 90°$, $\phi = 30°$) and ($\theta = 90°$, $\phi = 210°$), while the corresponding simulation results are shown in Figure 4.16a and Figure 4.16b, respectively. The iterative solution behavior for the Flamme geometry is the same as the one in the previous solution set, i.e., we cannot obtain an iterative convergence to the desired residual error for both illuminations. In each case, the residual error drops until a point, then it diverges and stagnates. The breakdown point can be shifted by using lower threshold error values in T-MLFMA, but the iterative solution eventually degenerates. In Figure 4.16, we

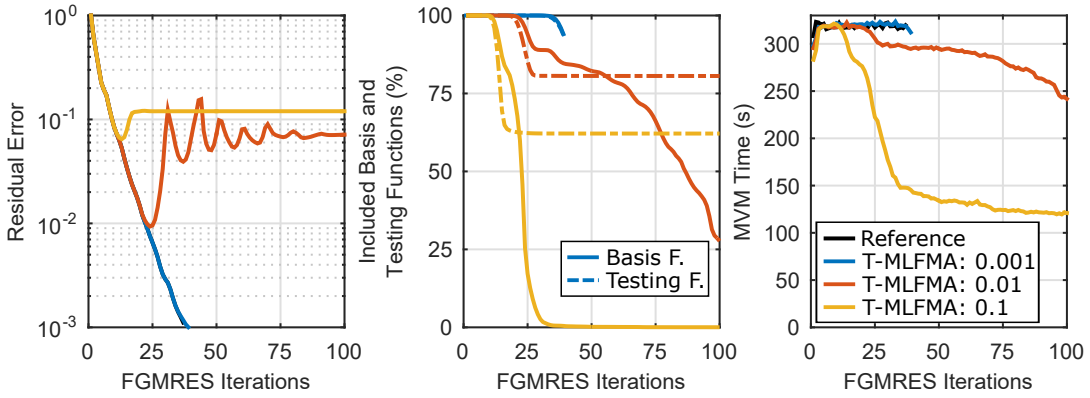

(a)

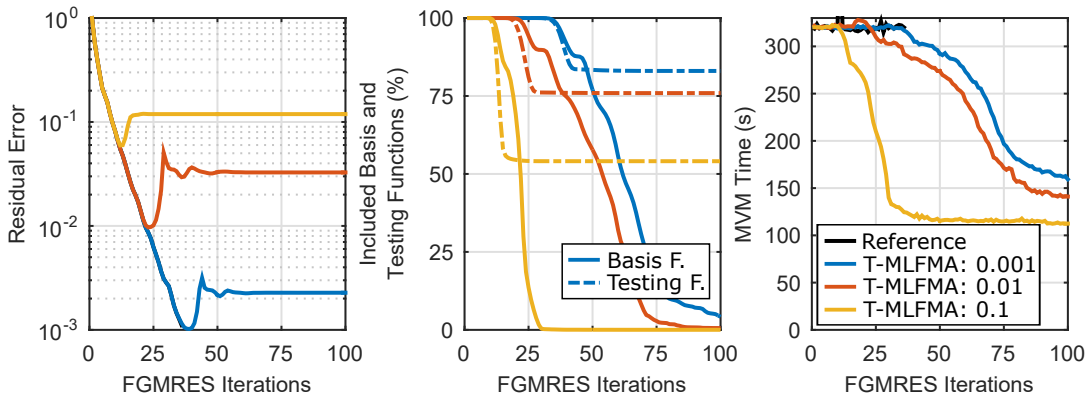

(b)

Figure 4.15: Solutions of scattering problems involving the NASA Almond geometry with an electrical size of 64λ using T-MLFMA with an extended trimming scheme. (a) Illumination from ($\theta = 90°$, $\phi = 30°$) and (b) illumination from ($\theta = 90°$, $\phi = 210°$).

also show the ratios of the included basis/testing functions in MVMs by T-MLFMA. BFEP trims the basis functions rapidly, while the testing function trimming stops and stagnates. Although the MVM time per iteration is reduced as a result of the eliminated basis/testing functions, the overall iterative solutions deteriorate and we cannot obtain a reasonable solution at the end.

The results shown in this section clearly shows that near-zone interactions should not be included in the trimming process.

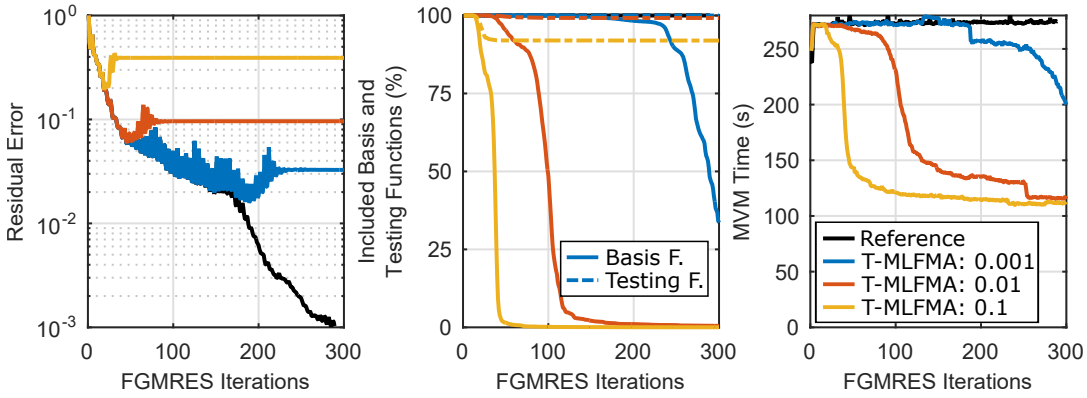

(a)

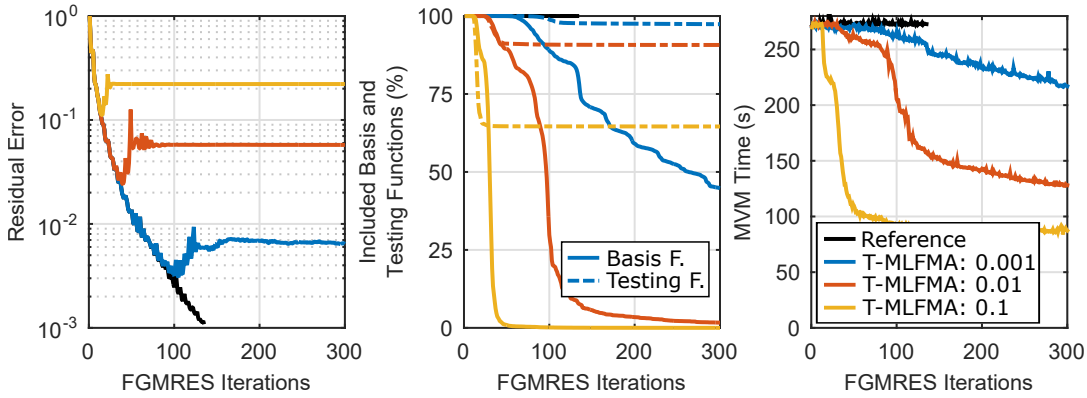

(b)

Figure 4.16: Solutions of scattering problems involving the Flamme geometry with an electrical size of 64λ using T-MLFMA with an extended trimming scheme. (a) Illumination from ($\theta = 90°$, $\phi = 30°$) and (b) illumination from ($\theta = 90°$, $\phi = 210°$).

4.5 Reusing Tree Structures

In this section, the reusability of T-MLFMA tree-structures is investigated. We first perform T-MLFMA simulations for the NASA Almond and the Flamme with electrical sizes of 64λ. The geometries are illuminated via plane waves with two different propagation angles, i.e., ($\theta = 90°$, $\phi = 30°$) and ($\theta = 90°$, $\phi = 210°$), and with horizontal polarization. The trimming error is selected as 0.1 for both basis and testing functions using a trimming counter value of one. We save the state of the tree-structure (kept boxes) at iterations with residual errors of 0.1, 0.05, and 0.01. Then, we directly use the tree-structures obtained for these residual errors in T-MLFMA so-

lutions (with static tree structures), without applying further trimming. Note that the tree-structures corresponding to higher residual errors are sparser. In these numerical examples, our aim is to understand if we can reuse a tree structure designed by T-MLFMA.

The simulation results obtained for the NASA Almond geometry with both illuminations are given in Table 4.10. T-MLFMA solutions with low reuse errors (residual errors of the original T-MLFMA) give extremely high error values for both surface currents and far-zone scattered fields. These are obviously due to the elimination of highly critical interactions. As we expect, the current and far-zone error values become lower for the simulations obtained with higher reuse error values. The tree-structures obtained at the early stages of the iterations include only small numbers of trimmed basis and testing functions. Therefore, the number of iterations and solution time results do not represent any improvement. The far-zone scattered electric field values with respect to the bistatic angle, given in Figure 4.17, support the comments above; solutions with sparser tree structures do not show any resemblance with the reference solutions.

The simulation results obtained for the Flamme geometry with both illuminations are given in Table 4.11. We observe results that are similar to those in the previous solution set. On the other hand, T-MLFMA solutions with low reuse errors give even higher errors for both surface currents and far-zone scattered fields. It seems that the discarded interactions are even more critical for the Flamme geometry. Although the iteration counts and solution times are lower than those of the reference simulation, we cannot obtain a reliable static T-MLFMA with an acceptable error level. The far-zone scattered electric field values with respect to the bistatic angle, given in Figure 4.18, agree with the comments above; solutions with sparser tree structures are significantly different from the reference solutions.

These results described above show that iteration-dependent dynamic tree structures obtained with T-MLFMA are unique for each geometry and illumination. Static tree structures cause uncontrollable errors, which lead to significantly inaccurate simulations. Therefore, T-MLFMA should be used with dynamic tree structures, which evolve as iterative solutions are performed.

Table 4.10: Details of the simulation results obtained by T-MLFMA for a scattering problem involving the NASA Almond geometry (64λ) with previously obtained tree structures.

Method	ϕ **(deg)**	**Reuse Error**	**Current Error (%)**	**Far-Field Error (%)**	**Number of Iter.**	**Solution Time (h)**
Ref.	30	-	-	-	37	3.27
Reuse	30	0.01	118	250	31	2.74
Reuse	30	0.05	72.2	48.9	36	3.17
Reuse	30	0.1	2.90	0.14	37	3.26
Ref.	210	-	-	-	36	3.20
Reuse	210	0.01	129	254	32	2.85
Reuse	210	0.05	71.2	39.5	36	3.20
Reuse	210	0.1	0.00	0.00	36	3.20

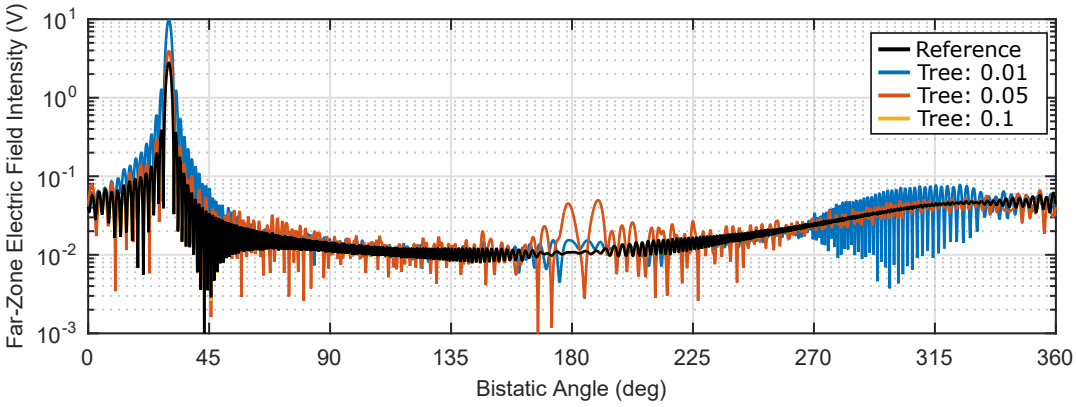

(a)

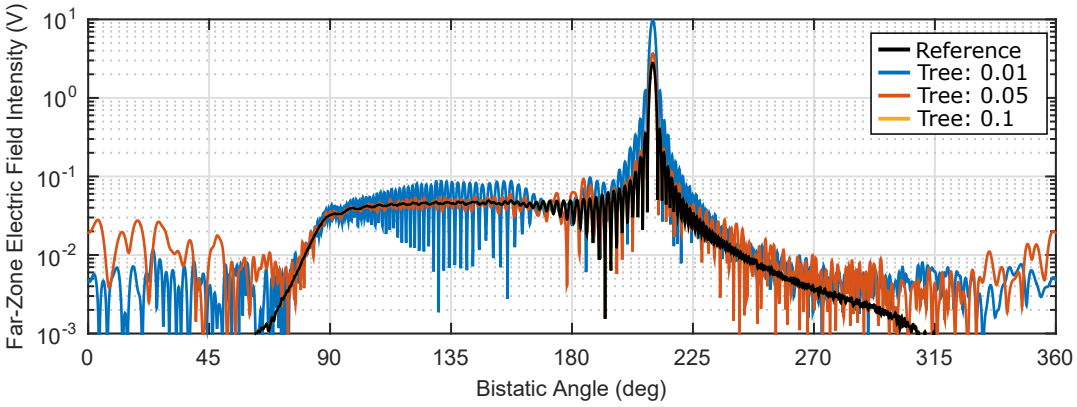

(b)

Figure 4.17: Solutions of scattering problems involving the NASA Almond geometry with an electrical size of 64λ using T-MLFMA with previously obtained tree structures. (a) Illumination from ($\theta = 90°$, $\phi = 30°$) and (b) illumination from ($\theta = 90°$, $\phi = 210°$).

Table 4.11: Details of the simulation results obtained by T-MLFMA for a scattering problem involving the Flamme geometry (64λ) with previously obtained tree structures.

Method	ϕ **(deg)**	**Reuse Error**	**Current Error (%)**	**Far-Field Error (%)**	**Number of Iter.**	**Solution Time (h)**
Ref.	30	-	-	-	289	21.9
Reuse	30	0.01	121	372	57	4.27
Reuse	30	0.05	113	237	88	6.64
Reuse	30	0.1	96.6	121	96	7.19
Ref.	210	-	-	-	289	21.9
Reuse	210	0.01	176	355	58	4.39
Reuse	210	0.05	167	248	100	7.56
Reuse	210	0.1	116	55.3	110	8.33

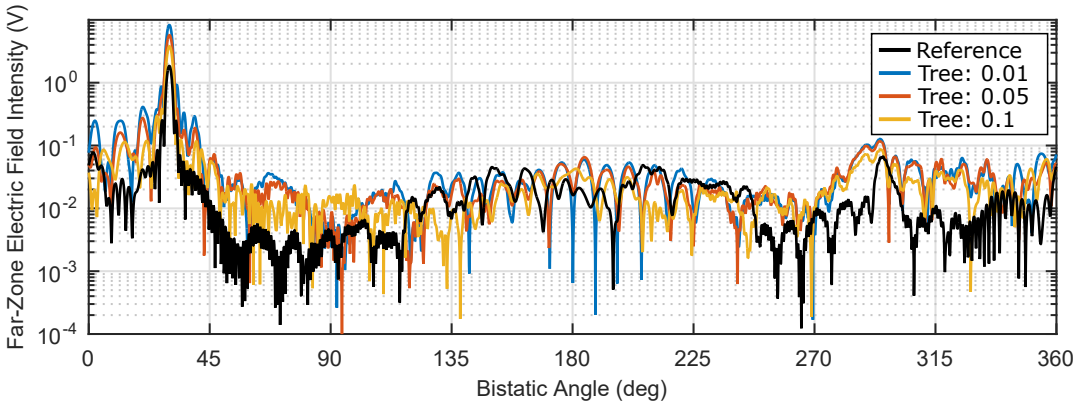

(a)

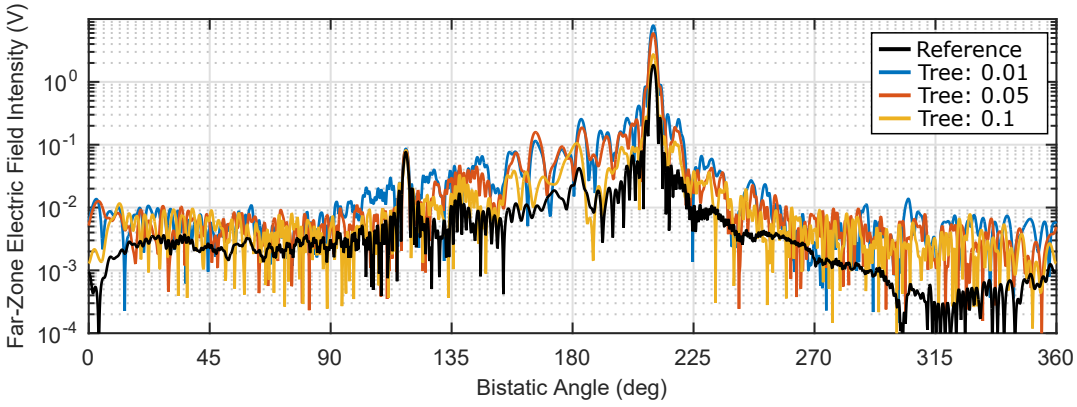

(b)

Figure 4.18: Solutions of scattering problems involving the Flamme geometry with an electrical size of 64λ using T-MLFMA with previously obtained tree structures. (a) Illumination from ($\theta = 90°$, $\phi = 30°$) and (b) illumination from ($\theta = 90°$, $\phi = 210°$).

4.6 Simulation Results For Various Illuminations

Electromagnetic scattering problems possess different numerical solution characteristics for different illuminations, although the target geometry and the impedance matrix remain the same. This section presents solutions of scattering problems involving the Flamme and an aircraft geometry illuminated by plane waves with various propagation angles. Considering these examples, we can further observe the capabilities and limitations of T-MLFMA simulations extensively. We fix the illuminations on the x-y plane, where ϕ changes from 0 to 180° with $10°$ discrete steps. The starting illumination angle of $\phi = 0$ corresponds to illuminating the back sides of the geometries (nozzles), while $\phi = 180°$ corresponds to illuminating the front sides of them (corresponding to the inlet of the aircraft).

The model of the aircraft geometry is presented in Figure 4.19. The aircraft is 15.58 m long and geometrically simplified. We terminate the inlet after it penetrates into the main body by approximately 3.4 m. The nozzle, on the other hand, is closed directly by a plate. The model is excited at 1 GHz; hence, it has an electrical size of 51.9λ. The surface current density on the aircraft geometry is expanded via 776,049 RWG functions. The Flamme geometry, considered in this section, has an electrical size of 64λ, as in the previous examples.

Similar to the earlier results, the electromagnetic scattering problems are formulated by using CFIE and solved iteratively via flexible GMRES. We further accelerate the iterative solutions by applying a block-diagonal preconditioner. The simulations are performed via T-MLFMA by using a trimming counter value of five and with relatively high error thresholds, i.e., 0.1, 0.2, and 0.3. We also consider PO results for these geometries to make extensive comparisons including a high-frequency technique.

In Figure 4.20, we show the far-zone scattered electric field values with respect to the bistatic angle in the azimuth plane for the Flamme geometry. We can observe a good match between the T-MLFMA and reference solutions. The scattering levels obtained with T-MLFMA follow the reference scattering levels consistently for the whole axis, including the forward-scattering and reflection directions. On the other hand, the PO

results mostly underestimate the scattering levels or miss strong scattering directions. Figure 4.20 also shows the focused views of the backscattering ranges for all illuminations. T-MLFMA simulations provide reliable scattering values that are consistent with the reference values, even for weak backscattering responses. In Tables 4.12 and 4.13, quantitative results for this solution set is presented. The surface current errors and far-zone scattered electric field errors are consistently low, similar to the results in the previous sections. The backscattering errors are relatively higher for low scattering levels, while convergence can still be satisfied with smaller trimming threshold errors. In terms of the solution time, the reference solutions require 190 iterations and 12.72 hours in average. In comparison to these, the T-MLFMA solutions with 0.3 trimming error require 55 iterations and 2.43 hours in average. Therefore, we obtain 70% iteration reduction and more than 80% solution-time reduction using T-MLFMA.

The simulation results for the aircraft geometry are similar to the results of the previous solution set. In Figure 4.21, we show the far-zone scattered electric field values with respect to the bistatic angle in the azimuth plane for the aircraft geometry. In scattering results, we observe a good match between the T-MLFMA and reference solutions. In addition, the scattering levels are consistent for the whole bistatic range. On the other hand, the PO results overestimate the field values at around the forward-scattering direction and underestimate in the backscattering range. Figure 4.21 also shows the focused views of the backscattering ranges for all illuminations. The T-MLFMA simulations provide accurate scattering values that match with the reference values, while they also show converging behavior. In the regions with weak backscattering responses, T-MLFMA provides consistently oscillating fields with small shifts. In addition, we can reduce the shifts easily by using lower trimming threshold values. In Tables 4.14 and 4.15, quantitative simulation results for the aircraft geometry are presented. The surface current errors are consistently low, while the far-zone scattered electric field errors are considerably below the threshold values. In terms of the solution time, the reference solutions require 384 iterations and 25.74 hours in average. On the other side, the T-MLFMA solutions with 0.3 trimming errors require 66 iterations and 2.69 hours in average. Therefore, we obtain more than 80% iteration reduction and 90% solution-time reduction.

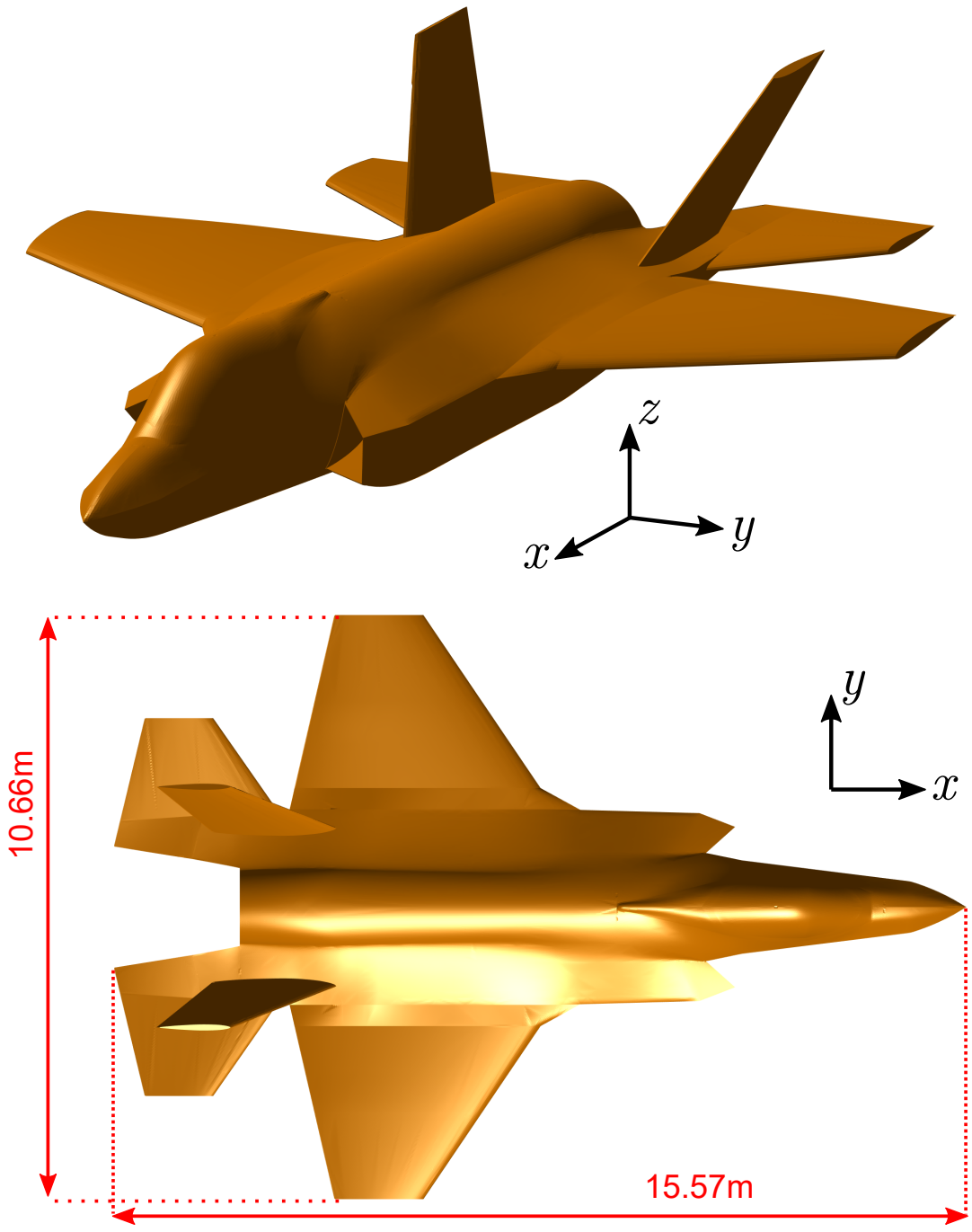

Figure 4.19: Model of a fighter aircraft geometry.

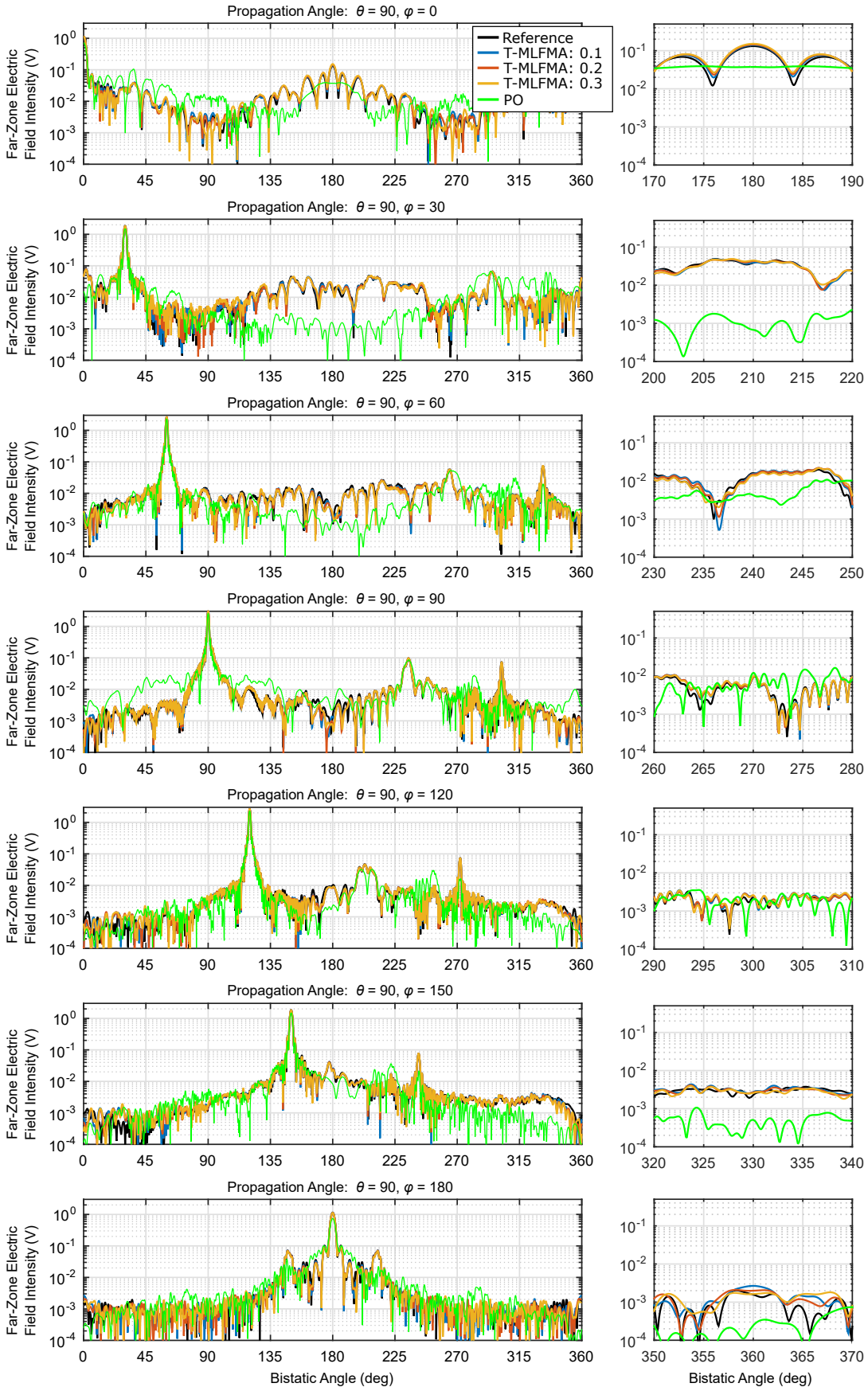

Figure 4.20: Solutions of scattering problems involving the Flamme geometry (64λ) with different illuminations.

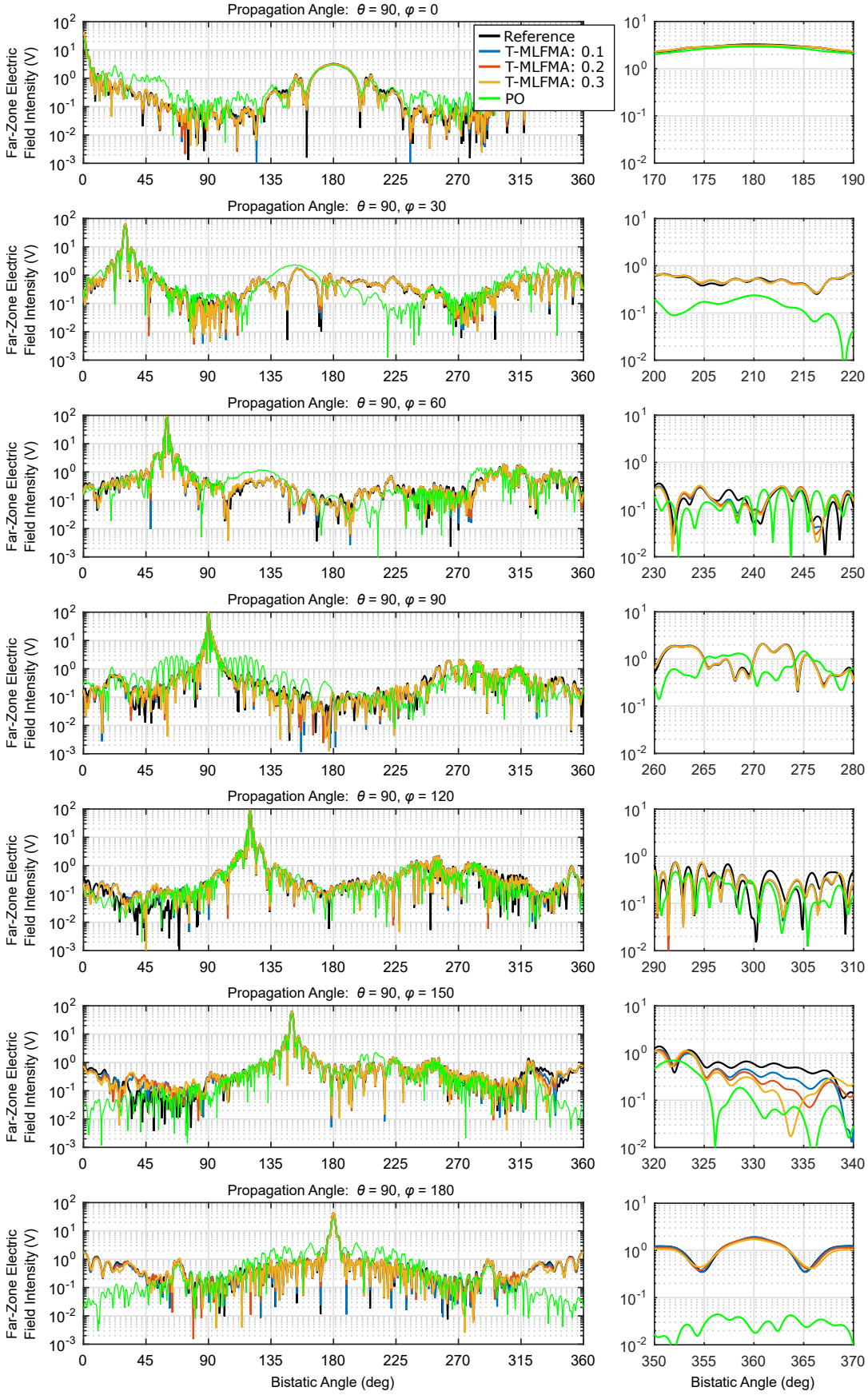

Figure 4.21: Solutions of scattering problems involving the aircraft geometry (51.9λ) with different illuminations.

Table 4.12: Details of the simulation results obtained by T-MLFMA for a scattering problem involving the Flamme geometry (64λ).

Method	**Basis Error**	ϕ **(deg)**	**Current Error (%)**	**Far-Field Error (%)**	**Backsca. Error (%)**	**Number of Iter.**	**Solution Time (h)**
Ref.	-	0	-	-	-	221	14.8
TMLFMA	0.1	0	15.6	3.18	12.5	70	3.36
TMLFMA	0.2	0	17.9	4.78	19.6	65	3.21
TMLFMA	0.3	0	21.6	7.03	29.0	63	2.76
PO	-	0	97.3	59.4	121	-	0.29
Ref.	-	30	-	-	-	289	20.0
TMLFMA	0.1	30	26.5	2.28	14.8	68	3.38
TMLFMA	0.2	30	28.0	3.38	20.0	65	3.24
TMLFMA	0.3	30	30.3	4.79	30.8	63	2.82
PO	-	30	89.8	35.1	101	-	0.27
Ref.	-	60	-	-	-	254	16.8
TMLFMA	0.1	60	25.2	1.45	24.4	58	2.90
TMLFMA	0.2	60	25.3	1.62	26.0	57	2.75
TMLFMA	0.3	60	26.3	2.01	27.9	56	2.60
PO	-	60	84.1	23.9	73.3	-	0.22
Ref.	-	90	-	-	-	185	12.2
TMLFMA	0.1	90	9.50	0.83	16.0	46	2.28
TMLFMA	0.2	90	9.51	0.98	15.9	45	2.15
TMLFMA	0.3	90	9.60	1.24	16.9	45	2.06
PO	-	90	72.5	24.5	152	-	0.22
Ref.	-	120	-	-	-	105	7.20
TMLFMA	0.1	120	7.31	0.65	18.3	48	2.29
TMLFMA	0.2	120	7.42	0.80	18.9	49	2.19
TMLFMA	0.3	120	7.63	1.08	19.5	50	2.11
PO	-	120	63.4	23.0	136	-	0.22

Table 4.13: Details of the simulation results obtained by T-MLFMA for a scattering problem involving the Flamme geometry (64λ).

Method	**Basis Error**	ϕ **(deg)**	**Current Error (%)**	**Far-Field Error (%)**	**Backsca. Error (%)**	**Number of Iter.**	**Solution Time (h)**
Ref.	-	150	-	-	-	137	9.05
TMLFMA	0.1	150	13.0	2.06	40.4	57	2.61
TMLFMA	0.2	150	13.5	2.13	44.9	56	2.43
TMLFMA	0.3	150	14.5	2.27	50.1	54	2.28
PO	-	150	73.7	31.0	102	-	0.27
Ref.	-	180	-	-	-	137	9.05
TMLFMA	0.1	180	10.7	2.87	78.7	63	2.98
TMLFMA	0.2	180	12.4	4.03	76.1	59	2.62
TMLFMA	0.3	180	15.0	4.50	88.0	56	2.40
PO	-	180	80.4	47.5	94.4	-	0.36

Table 4.14: Details of the simulation results obtained by T-MLFMA for a scattering problem involving the aircraft geometry (51.9λ).

Method	**Basis Error**	ϕ **(deg)**	**Current Error (%)**	**Far-Field Error (%)**	**Backsca. Error (%)**	**Number of Iter.**	**Solution Time (h)**
Ref.	-	0	-	-	-	283	19.0
TMLFMA	0.1	0	7.73	2.15	3.42	69	2.93
TMLFMA	0.2	0	8.29	2.40	3.81	67	2.58
TMLFMA	0.3	0	9.22	2.70	4.25	66	2.46
PO	-	0	95.5	52.5	14.4	-	0.35
Ref.	-	30	-	-	-	310	20.8
TMLFMA	0.1	30	7.49	1.07	7.17	67	3.00
TMLFMA	0.2	30	7.94	1.22	7.66	67	2.73
TMLFMA	0.3	30	8.61	1.47	7.97	65	2.48
PO	-	30	85.3	28.7	91.4	-	0.24

Table 4.15: Details of the simulation results obtained by T-MLFMA for a scattering problem involving the aircraft geometry (51.9λ).

Method	**Basis Error**	ϕ **(deg)**	**Current Error (%)**	**Far-Field Error (%)**	**Backsca. Error (%)**	**Number of Iter.**	**Solution Time (h)**
Ref.	-	60	-	-	-	349	23.4
TMLFMA	0.1	60	13.3	1.46	34.2	74	3.32
TMLFMA	0.2	60	14.1	1.60	36.8	72	2.91
TMLFMA	0.3	60	15.3	1.88	40.7	69	2.72
PO	-	60	76.5	17.5	101	-	0.24
Ref.	-	90	-	-	-	392	26.3
TMLFMA	0.1	90	20.0	2.02	6.34	78	3.50
TMLFMA	0.2	90	20.4	1.93	6.48	75	3.33
TMLFMA	0.3	90	21.1	1.99	6.76	73	2.93
PO	-	90	74.6	25.9	105	-	0.22
Ref.	-	120	-	-	-	438	29.4
TMLFMA	0.1	120	29.4	1.92	47.1	69	3.05
TMLFMA	0.2	120	29.6	1.93	47.2	66	2.80
TMLFMA	0.3	120	29.9	2.03	48.4	64	2.68
PO	-	120	75.7	16.2	69.5	-	0.20
Ref.	-	150	-	-	-	468	31.4
TMLFMA	0.1	150	25.6	2.18	29.8	74	3.70
TMLFMA	0.2	150	27.2	2.97	40.3	71	3.34
TMLFMA	0.3	150	30.0	3.73	55.5	68	3.00
PO	-	150	78.5	27.0	81.8	-	0.19
Ref.	-	180	-	-	-	448	30.0
TMLFMA	0.1	180	24.0	1.96	4.76	64	3.06
TMLFMA	0.2	180	25.8	2.67	8.21	59	2.72
TMLFMA	0.3	180	27.9	4.04	14.2	57	2.56
PO	-	180	88.6	55.5	100	-	0.27

4.7 Numerical Results for Various Electromagnetic Problems

In this section, we present simulation results for different electromagnetic problems, such as scattering, radiation, and transmission problems. The scattering problems include the NASA Almond, the Flamme, and an aircraft geometry. In the radiation problem, we discuss the results of simulations of a patch array antenna. Finally, in the transmission problem, simulations of an array of split-ring resonators (SRR) in resonance and off-resonance frequencies are shown.

4.7.1 Scattering Problems

In this part, we present analyses of different types of geometries. The NASA Almond is considered as a canonical geometry, while the Flamme and an aircraft geometry are considered as real-life applications. We model all geometries as PEC solid bodies, which are formulated with CFIE. The surface current densities on the geometries are expanded with the RWG functions on $\lambda/10$ triangles, while the Galerkin scheme is used to select the testing functions. We consider plane wave illumination and solve the corresponding matrix equations iteratively by using flexible GMRES. Also, the iterative solutions are accelerated via the block-diagonal preconditioner. We obtain the solutions by using regular MLFMA as the reference, T-MLFMA with ML-based BFEP, T-MLFMA with manual-based BFEP, and PO. In the following simulation results of this subsection, the trimming threshold of the basis functions (α) is set as 0.1. The trimming threshold of the testing functions (β) is set as 0.05 to obtain less than 5% error in the overall scattered fields. We compare the results of the simulations in five categories; surface current error, far-zone scattered electric field error, backscattering error, number of iterations, and solution time.

The first problem involves the NASA Almond geometry. The model is 600 mm long and excited at 32 GHz, which corresponds to an electrical length of 64λ. The number of unknowns for this problem is 893,727. The geometry is illuminated by a plane wave with propagation direction $\theta = 90^\circ$ and $\phi = 30^\circ$, and with horizontal polarization. Figure 4.22 presents the bistatic far-zone electric field intensity on the x-y plane obtained by using the conventional MLFMA and the proposed T-MLFMA, as well as with the PO using the same discretization. The far-zone electric field intensity plots

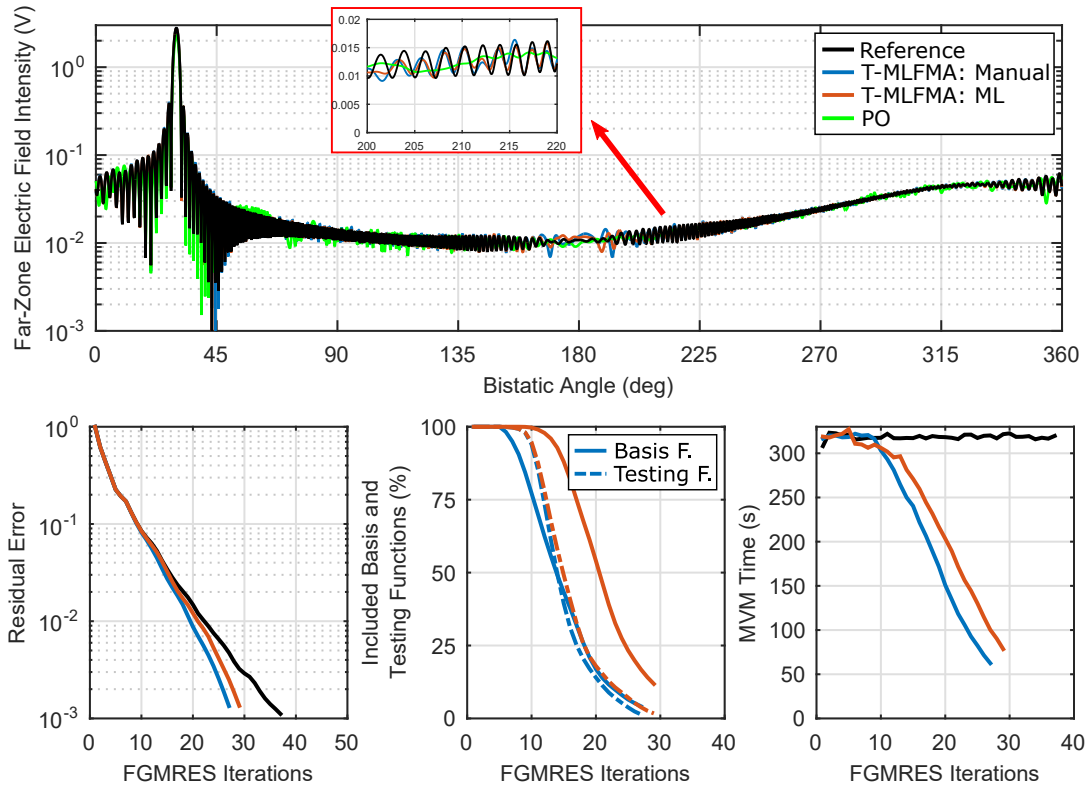

Figure 4.22: Solutions of a scattering problem involving the NASA Almond geometry with an electrical size of 64λ using T-MLFMA.

show a good match between T-MLFMA and MLFMA, while the PO values surprisingly agree with the MLFMA values. The reasonably accurate far-zone results of PO are due to the simplicity of the geometry, while we note that it still does not provide the oscillatory behavior at around the backscattering direction. Figure 4.22 also depicts the residual errors with respect to FGMRES iterations, where it is apparent that the iterations are reduced with T-MLFMA. Figure 4.22 further shows the ratio of the included basis/testing functions, as well as the MVM time per iteration for FGMRES iterations. The trimming process starts after the fifth iteration and continues until the end of the solution, while the MVM time is reduced from 320 s (first iteration) to 78 s (last iteration) for T-MLFMA with ML-based BFEP. In Table 4.16, we present further details of the analysis of the NASA Almond geometry. PO provides visually consistent far-zone results, but it gives more than 25% far-field error. T-MLFMA, on the other hand, provides quite small surface current errors and far-zone electric field errors, while the overall far-zone errors are below 5% as targeted. Another important

Table 4.16: Details of the Simulation Results for 64λ NASA Almond

Method	**Current Error (%)**	**Far-Field Error (%)**	**Backsca. Error (%)**	**Number of Iter.**	**Solution Time (h)**
Ref.	-	-	-	37	3.27
Manual	4.54	2.04	19.5	27	1.69
ML	4.04	1.12	13.4	29	1.93
PO	53.2	27.7	22.6	-	0.28

detail is that the manual-based approach doubles the far-zone and backscattering error values in comparison to the ML-based method. Overall, T-MLFMA reduces the number of iterations by 12% and reduces the solution time by 40%.

The second scattering problem involves of the Flamme geometry. The model is 600 mm long and excited at 32 GHz, which corresponds to an electrical length of 64λ. The surface current density on the geometry is expanded with 811,080 RWG functions. The geometry is illuminated by a plane wave with propagation direction $\theta = 90^\circ$ and $\phi = 30^\circ$, and with horizontal polarization, i.e., the incident wave propagates towards the nozzle. This illumination direction is selected due to the difficulty of the scattering problem, which involves strong multiple reflections and diffractions. Figure 4.23 presents the bistatic far-zone electric field intensity on the x-y plane obtained by using the conventional MLFMA and the proposed T-MLFMA, as well as with PO using the same discretization. The far-zone electric field intensity results show a good match between T-MLFMA and MLFMA in terms of field levels and oscillations. The PO values, however, significantly deviate from the MLFMA values, generally underestimating field levels, especially in the backscattering (210°) direction due to the multiple reflections and diffractions from the geometry. Figure 4.23 also depicts the residual errors with respect to FGMRES iterations, where it is apparent that the iterations are reduced with T-MLFMA. Figure 4.23 further shows the ratio of the included basis/testing functions, as well as the MVM time per iteration. The trimming process starts after the fifth iteration and continues until the end of the solution, while the MVM time is reduced from 275 s (first iteration) to 32 s (last iteration) for T-MLFMA with ML-based BFEP. In Table 4.17, we present further details of the

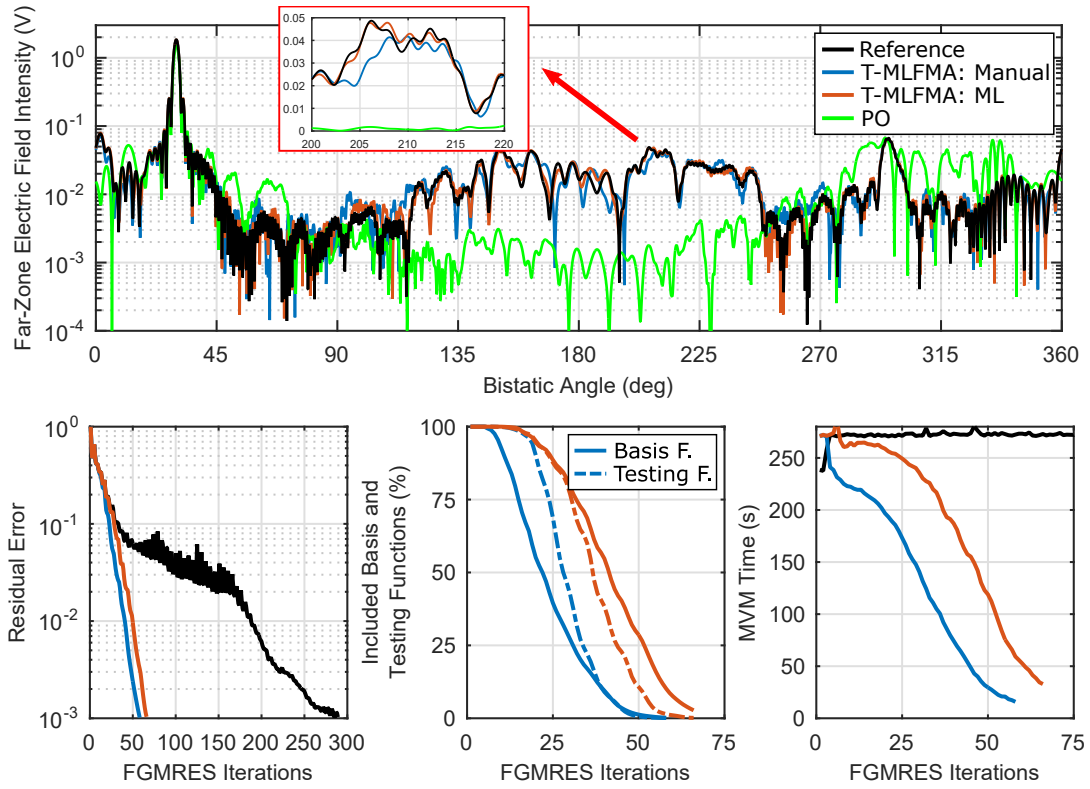

Figure 4.23: Solutions of a scattering problem involving the Flamme geometry with an electrical size of 64λ using T-MLFMA.

analysis of the Flamme geometry. PO leads to more than 35% far-zone error, and it gives more than 100% backscattering error. T-MLFMA, especially using the ML-based approach, provides small far-zone electric field error. Specifically, the overall far-zone errors are below 5%, almost half of the target error. In addition, T-MLFMA provides accurate and consistent results in the backscattering region. The manual-based approach yields more than twice far-zone and backscattering errors compared to the ML-based method, showing the issues in this approach in terms of error controllability. Overall, T-MLFMA reduces the number of iterations by 77% and reduces the solution time by 84%. T-MLFMA gives a solution time reduction higher than the reduction in the number of iterations due to the accelerated MVMs as the iterations continue.

At the third and final scattering problem, we consider a fighter aircraft geometry. The model, shown in Figure 4.19, is 15.58 m long and excited at 1 GHz, which corre-

Table 4.17: Details of the Simulation Results for the 64λ Flamme

Method	**Current Error (%)**	**Far-Field Error (%)**	**Backsca. Error (%)**	**Number of Iter.**	**Solution Time (h)**
Ref.	-	-	-	289	21.9
Manual	36.3	7.28	50.3	58	2.53
ML	28.0	3.11	19.0	66	3.41
PO	89.8	35.1	101	-	0.23

sponds to an electrical length of 51.9λ. The surface of the target is discretized with 517,366 triangles, which leads to 776,049 RWG functions. The target is illuminated by a plane wave with propagation direction $\theta = 90^\circ$ and $\phi = 180^\circ$, and with horizontal polarization, i.e., the incident wave propagates towards the inlet. Low-detectability of the fighter aircraft from the nose is crucial, hence this is a critical illumination angle for radar-cross-section analysis. Illumination from the nose is also a problematic numerical problem since the inlets of the aircraft involve strong resonances and cause high backscattering values. Therefore, obtaining accurate results with efficient simulations is very important. Figure 4.24 presents the bistatic far-zone electric field intensity on the x-y plane obtained by using the conventional MLFMA and the proposed T-MLFMA, as well as with the PO using the same discretization. The far-zone electric field intensity results show a remarkable match between T-MLFMA and MLFMA, although the aircraft geometry is not included in the dataset to train the ML model. The T-MLFMA results successfully show the dips and peaks of the field oscillations. The PO values, however, completely deviate from the MLFMA values with underestimation of scattering. Specifically, PO underestimates the backscattering (0°) value by almost two orders of magnitude. Figure 4.24 also depicts the residual errors with respect to FGMRES iterations, where it is apparent that the iterations are reduced with T-MLFMA. Figure 4.24 further shows the ratio of the included basis/testing functions, as well as MVM time per iteration. The trimming process rapidly starts and continues until all basis/testing functions are omitted at the end of the solution, while the MVM time is reduced from 225 s (first iteration) to only 21 s (last iteration) for T-MLFMA with ML-based BFEP. In Table 4.18, we present further details of the analysis of the aircraft geometry. PO leads to more than 55% far-zone

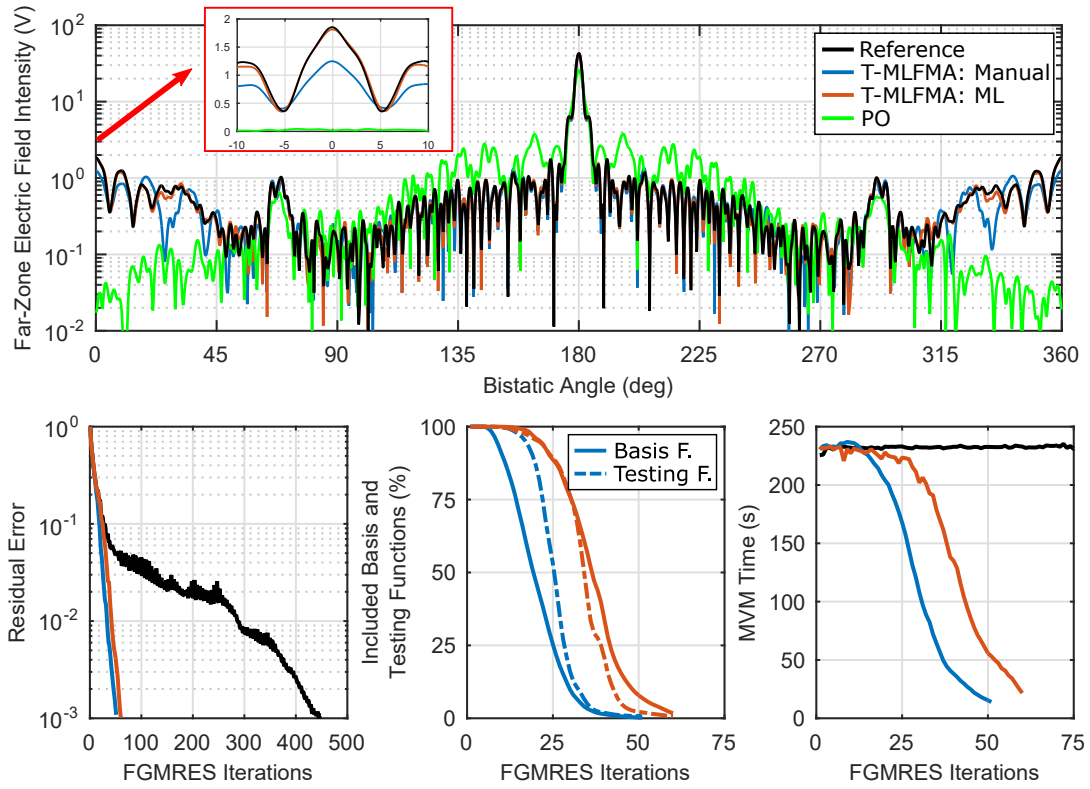

Figure 4.24: Solutions of a scattering problem involving the aircraft geometry with an electrical size of 51.9λ using T-MLFMA.

error, and it gives more than 100% backscattering error. T-MLFMA, especially using the ML-based approach, gives small far-zone electric field error, i.e., the overall far-zone error is only 2.6% (5% is the target error). The backscattering value obtained by using T-MLFMA agrees very well with the reference solution by an error of 6.7%. The manual-based approach yields more than three times far-zone error and more than five times backscattering error in comparison to the ML-based method. These error levels clearly demonstrate that the manual-based approach should not be used in critical simulations, where error controllability is required. Overall, T-MLFMA with ML-based BFEP reduces the number of iterations by 86% and the solution time by 90%.

Table 4.18: Details of the Simulation Results for the 51.9λ Aircraft

Method	**Current Error (%)**	**Far-Field Error (%)**	**Backsca. Error (%)**	**Number of Iter.**	**Solution Time (h)**
Ref.	-	-	-	448	28.6
Manual	34.7	7.81	35.2	51	1.94
ML	25.8	2.61	6.72	60	2.70
PO	88.6	55.5	100	-	0.27

4.7.2 Radiation Problems

Next, we consider a radiation pattern calculation involving a free-standing patch array. The geometry used is inspired by the 5×5 patch antenna array presented in [105], where the current phases of the elements are optimized to obtain a directive radiation pattern. The primary 5×5 array is repeated four times in both x and y directions with changing excitation values, leading to a larger array that consists of 20×20 patch antennas. Each element is a 3×3 mm square PEC plate with zero thickness, and they are placed periodically with 3 mm gaps between them. We also note that each patch is excited from its bottom by using a current source (1 A and optimized phase) at 24.5 GHz. Uisng a discretization with 0.6 mm triangles ($\sim \lambda/20$), a total of 34,400 RWG functions are defined for the whole array. The array model and the phase values of the excitations are shown in Figure 4.25a.

Since the surfaces have zero thickness, we formulate the electromagnetic radiation problem by using EFIE. Figure 4.25b presents the normalized radiation patterns on the z-x plane obtained by using the conventional MLFMA and the proposed T-MLFMA. The radiation patterns are normalized with the maximum field value of the reference result. In T-MLFMA, we set the basis function trimming threshold α as 0.01 considering the electrically small size of the discretization. We also set the testing function trimming threshold β as 0.05 to keep the overall far-zone electric field error below 5%. The radiation pattern results show a remarkable match between T-MLFMA and MLFMA, although the ML dataset includes only CFIE solutions without any antenna geometry. In Table 4.19, we present further details of the radiation simulations. Sur-

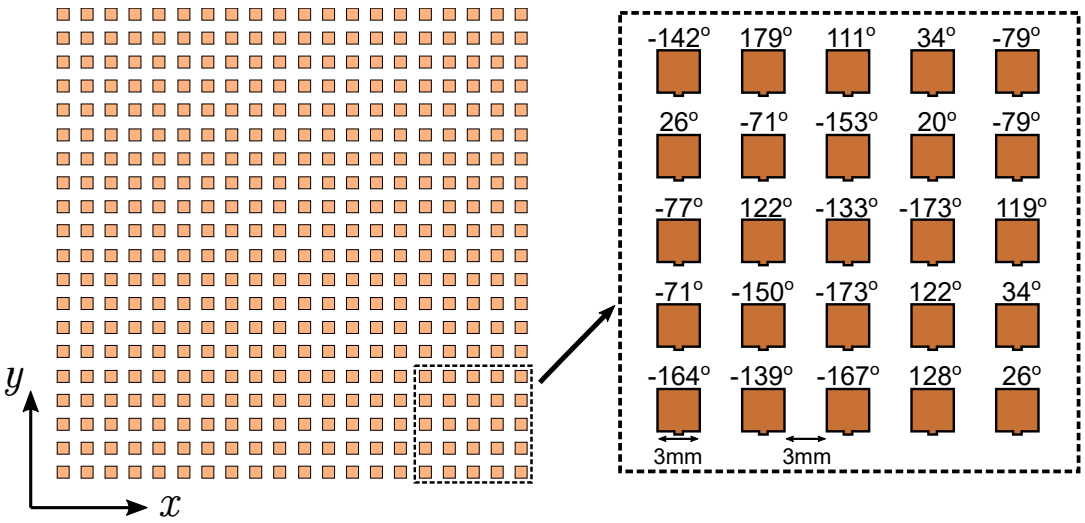

(a)

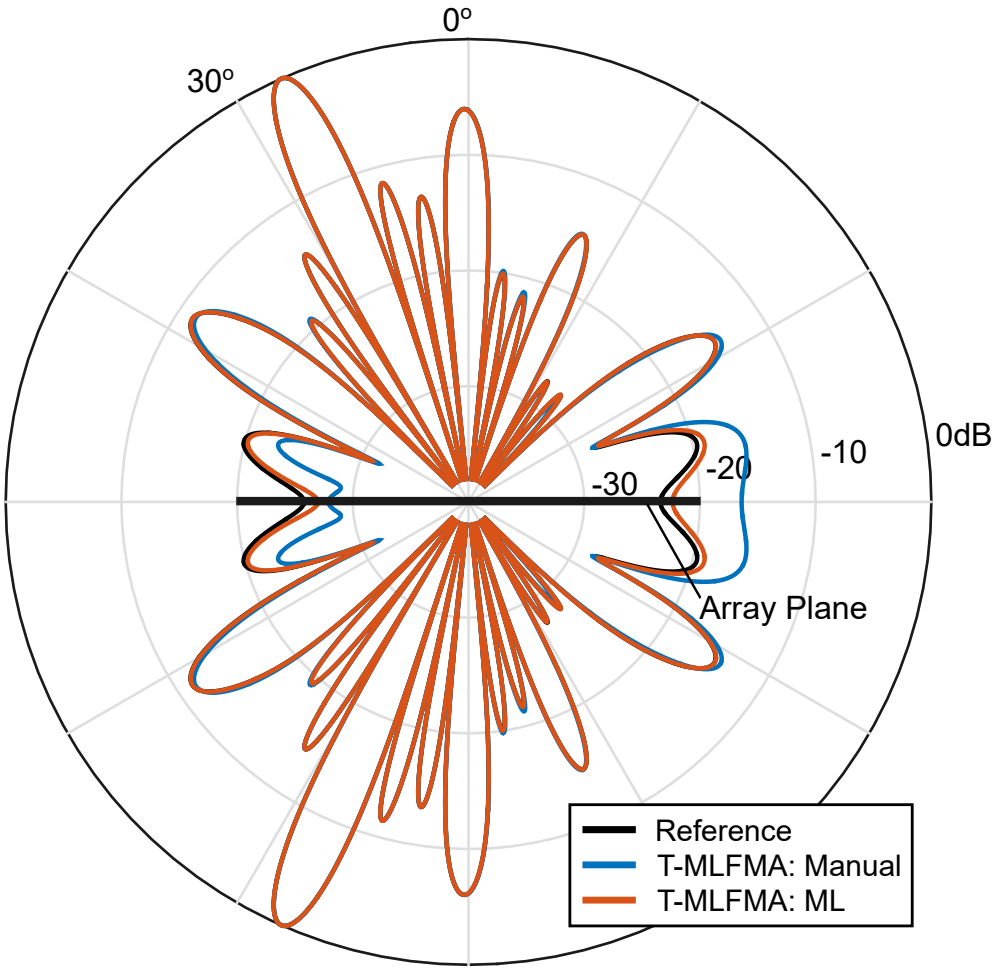

(b)

Figure 4.25: (a) Model and excitation details for the 20×20 patch array. (b) Normalized radiation pattern of the array.

Table 4.19: Details of the Simulation Results for the 20×20 patch antenna array

Method	**Current Error (%)**	**Far-Field Error (%)**	**Number of Iter.**	**Solution Time (h)**
Ref.	-	-	144	0.35
Manual	10.5	14.9	73	0.13
ML	10.3	1.66	128	0.24

prisingly, T-MLFMA versions give similar surface current error values, while the far-zone electric field errors of the ML-based and manual-based approaches are completely different. The manual-based approach gives almost nine times more field error than the ML-based method, although it is two times faster. T-MLFMA with the ML-based approach gives a small far-zone electric field error, i.e., it is only 1.66% (target error is 5%). Overall, T-MLFMA with ML-based BFEP reduces the number of iterations by 11% and the solution time by 31%.

4.7.3 Transmission Problems

As the final numerical simulation set in this section, we consider transmission problems involving an SRR array. The SRR array is inspired by the simulations considered in [98]. The details of the model is shown in Figure 4.26. Each SRR element consists of two nested oppositely slitted circular PEC rings with zero thicknesses. The width of the slits is 0.192 mm. The outer and inner radii of the larger ring are 2.87 mm and 2.19 mm, while the outer and inner radii of the smaller ring are 1.79 mm and 1.15 mm. The array contains $3 \times 20 \times 15$ SRR elements, which are periodically placed on the x-y plane with 7 mm distance and regularly arranged along the z axis with 12 mm gap. The SRR array designed with the dimensions given above exhibits a strong resonance and becomes opaque between 8.2 GHz and 9 GHz. In the rest of the frequency range, it behaves as a transparent object. We illuminate the SRR array via a Hertzian dipole source with $+y$ directed dipole moment, which is placed at 50 mm distance from the center of the array on the x axis. We use a 0.75 mm triangular mesh to discretize the geometry, leading to a square matrix equation that consists of 57,600 unknowns.

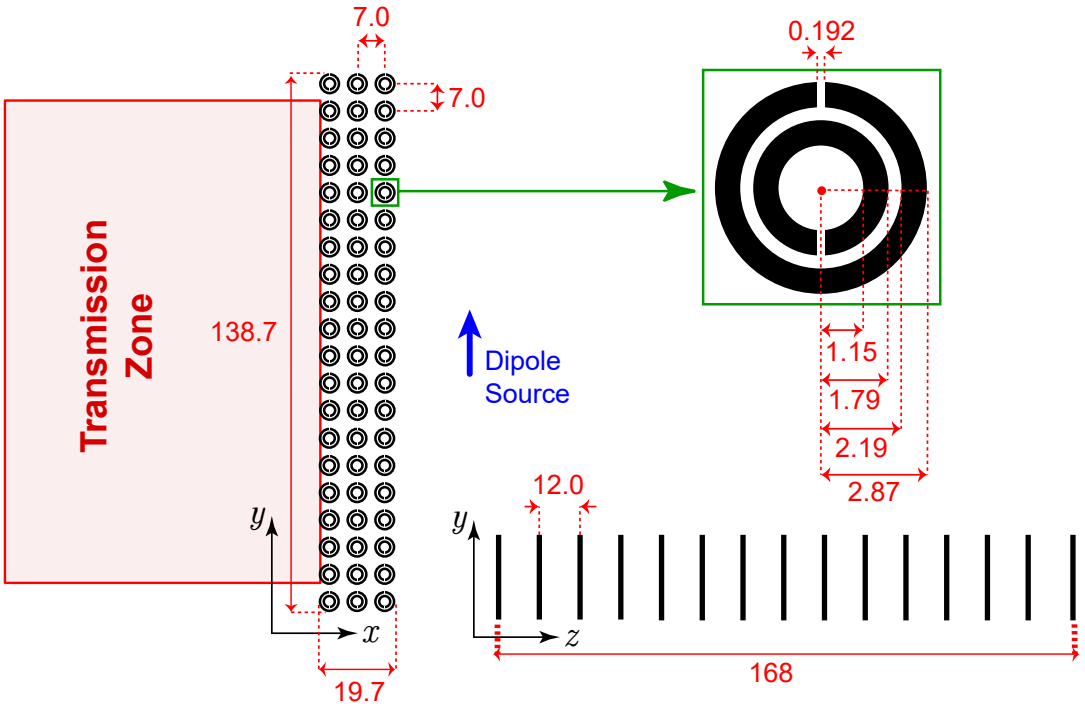

Figure 4.26: Details and dimensions (in mm) of the $3 \times 20 \times 15$ SRR array structure that is designed to resonate at around 8.5 GHz.

This problem is also formulated by using EFIE since the geometry consists of open surfaces. We illuminate the SRR array at 8.5 GHz (resonance frequency) and 9.5 GHz (off-resonance frequency). Figure 4.27 presents the near-zone electric field intensity on the x-y plane in the vicinity of the SRR array obtained by using the conventional MLFMA and the proposed T-MLFMA. We set the basis function trimming threshold α as 0.005 due to the electrically small size of the discretization and highly sensitive characteristics of the geometry. We also set the testing function trimming threshold β as 0.1 to obtain the overall electric field error below this value. The near-zone electric field error is calculated as

$$\text{Nearfield error}(\%) = \frac{\sqrt{\sum_{s=1}^{S} \left\| \boldsymbol{E}_s^{ref} - \boldsymbol{E}_s \right\|_2^2}}{\sqrt{\sum_{s=1}^{S} \left\| \boldsymbol{E}_s^{ref} \right\|_2^2}} \times 100, \tag{4.4}$$

where S is the number of near-zone samples in the transmission region, $\boldsymbol{E}_s^{ref}$ is the reference electric field, and $\boldsymbol{E}_s$ is the electric field obtained with T-MLFMA in the transmission region. As shown in Figure 4.27, the transmission region starts right after the SRR array geometry. The near-zone electric field distributions show a re-

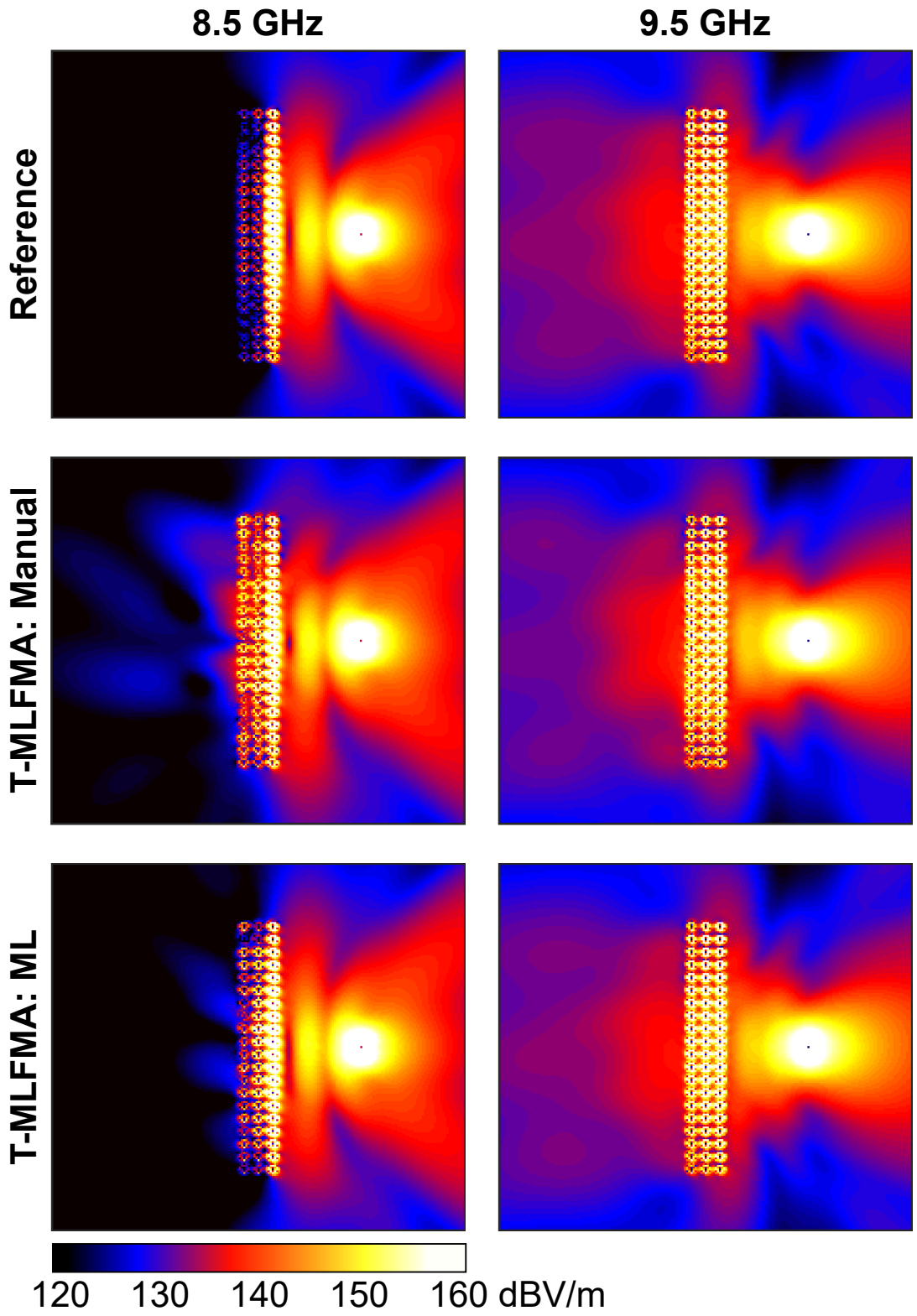

Figure 4.27: Electric field in the vicinity of the $3 \times 20 \times 15$ SRR array. The array is illuminated by a dipole.

Table 4.20: Details of the Simulation Results for the 3×20 SRR array

Method	**Freq. (GHz)**	**Current Error (%)**	**Nearfield Error (%)**	**Number of Iter.**	**Solution Time (h)**
Ref.	8.5	-	-	775	2.66
Ref.	9.5	-	-	457	1.86
Manual	8.5	37.6	30.2	736	0.65
Manual	9.5	24.1	17.6	301	0.42
ML	8.5	22.6	13.9	783	0.99
ML	9.5	8.60	7.92	349	0.67

markable match between T-MLFMA and MLFMA. T-MLFMA provides very successful results at the off-resonance frequency, while small discrepancies are observed at the resonance frequency. In Table 4.20, we present further details of the simulation results for the SRR array. ML-based T-MLFMA simulations provide near-zone electric field error below the threshold value at the off-resonating frequency, while it exceeds 10% at the resonance frequency. This is due to the numerically challenging nature of the array when SRRs resonate. The manual-based approach, on the other hand, gives more than two times larger near-zone electric field errors in comparison to the ML-based method, although it is only 30% faster. Overall, T-MLFMA with ML-based approach reduces the number of iterations by 23% and reduces the solution time by 63% at the off-resonating frequency. At the resonance frequency, however, it increases the number of iterations by 1%, while it still reduces the solution time by 62%.

4.8 T-MLFMA Preconditioner

In this section, we propose an alternative practice of the trimming scheme for preconditioning based on approximate forms of T-MLFMA. Approximate MLFMA (AMLFMA) versions are used as preconditioners in the literature [9]; so we integrate the trimming scheme in this kind of accelerated simulations. Specifically, we use the outer and inner solution scheme, where we use FGMRES for outer solutions and GMRES for inner solutions. The termination criterion for FGMRES is set as 0.001 relative resid-

ual error, while GMRES solutions are restricted to only 0.1 residual error and maximum 10 iterations. The inner-solution MVMs are performed via trimmed AMLFMA (T-AMLFMA), where AMLFMA is obtained by changing the number of harmonics, i.e., the harmonic numbers are multiplied with an approximation factor (A-Factor) at all levels of the given tree structure. The MVM scheme works as a regular MLFMA for the A-Factor value of 1, while it reduces into only near-zone interactions for the A-Factor value of 0.

We share the numerical simulations in this section in two categories, i.e., outer solutions with regular MLFMA and outer solutions with T-MLFMA. We select scattering from the aircraft geometry as the test scenario for the performance assessment of the introduced preconditioner. The aircraft geometry is illuminated via a plane wave from the nose (with propagation angle $\theta = 90^\circ$ and $\phi = 180^\circ$, and with horizontal polarization). We formulate the scattering problem with CFIE and accelerate the reference solution by using the BD preconditioner. We again consider surface current errors, far-zone electric field errors, number of iterations, and solution times to assess the performance of the preconditioner.

In the first solution set, we present the analysis of the aircraft geometry by using T-MLFMA accelerated via the T-AMLFMA preconditioner. The trimming process detects the converged basis and testing functions to omit at each iteration of the outer solution. The outer solution shares the list of the remaining basis and testing functions, as well as the trimmed tree structure with the inner solutions. Then, T-AMLFMA, in an inner solution, directly uses the trimmed structure. We test various A-Factor values for T-AMLFMA, leading to the results in Figure 4.28. The figure depicts the far-zone scattered electric field values with respect to the bistatic angle in the azimuth plane. We observe the agreement of the T-MLFMA solutions with the reference solution in the whole bistatic range. Figure 4.28 also shows the iterative convergence and gives the ratio of the included basis (solid lines) and testing (dashed lines) functions. We observe that the iterative convergence of T-MLFMA is significantly accelerated by the preconditioner. Figure 4.28 further illustrates the MVM time per iteration for FGMRES iterations, where the solid lines represent the MVM time per iteration and the dashed lines represent the inner solution time per iteration. The required time for an outer MVM and for an inner solution are both significantly reduced thanks to

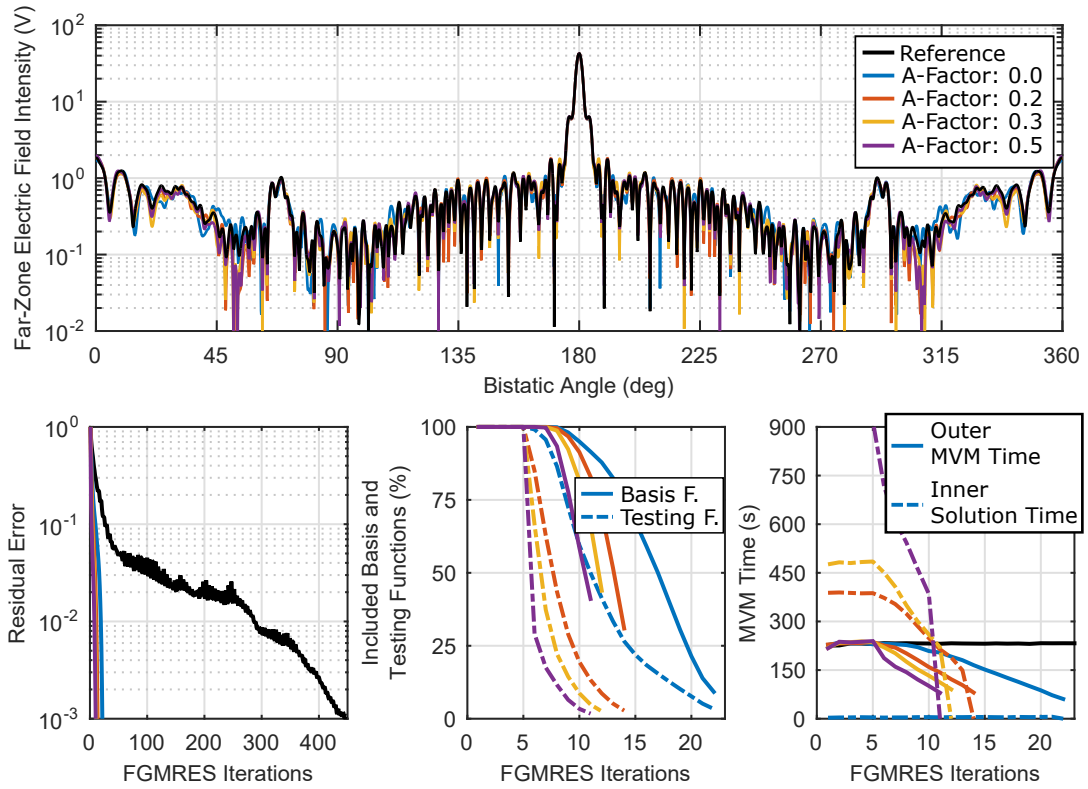

Figure 4.28: Solutions of a scattering problem involving the aircraft geometry With Electrical Size of 51.9λ by using T-MLFMA and T-AMLFMA Preconditioner.

the trimmed basis and testing functions. In Table 4.21, the details of the simulation results for this solution set are presented. All T-MLFMA solutions give the far-zone electric field error below the 5% threshold, even for the A-Factor value of 0, which offers 95% iteration reduction and 96% solution time reduction.

In the second solution set, we present the analysis of the aircraft geometry by using MLFMA as the outer solver and T-AMLFMA as the inner solver for preconditioning. We first perform solutions with the AMLFMA preconditioner, without any trimming process, for various A-Factor values. Then, we perform solutions by using T-AMLFMA for various A-Factor values and different trimming threshold values. The trimming process is the same as the one in the previous solution set. Specifically, the converged basis and testing functions are omitted at each iteration of the outer solution, and then, the trimmed layout is directly applied to the inner solution MVMs (T-AMLFMA). In Table 4.22 and Figure 4.29, the details of the simulation results

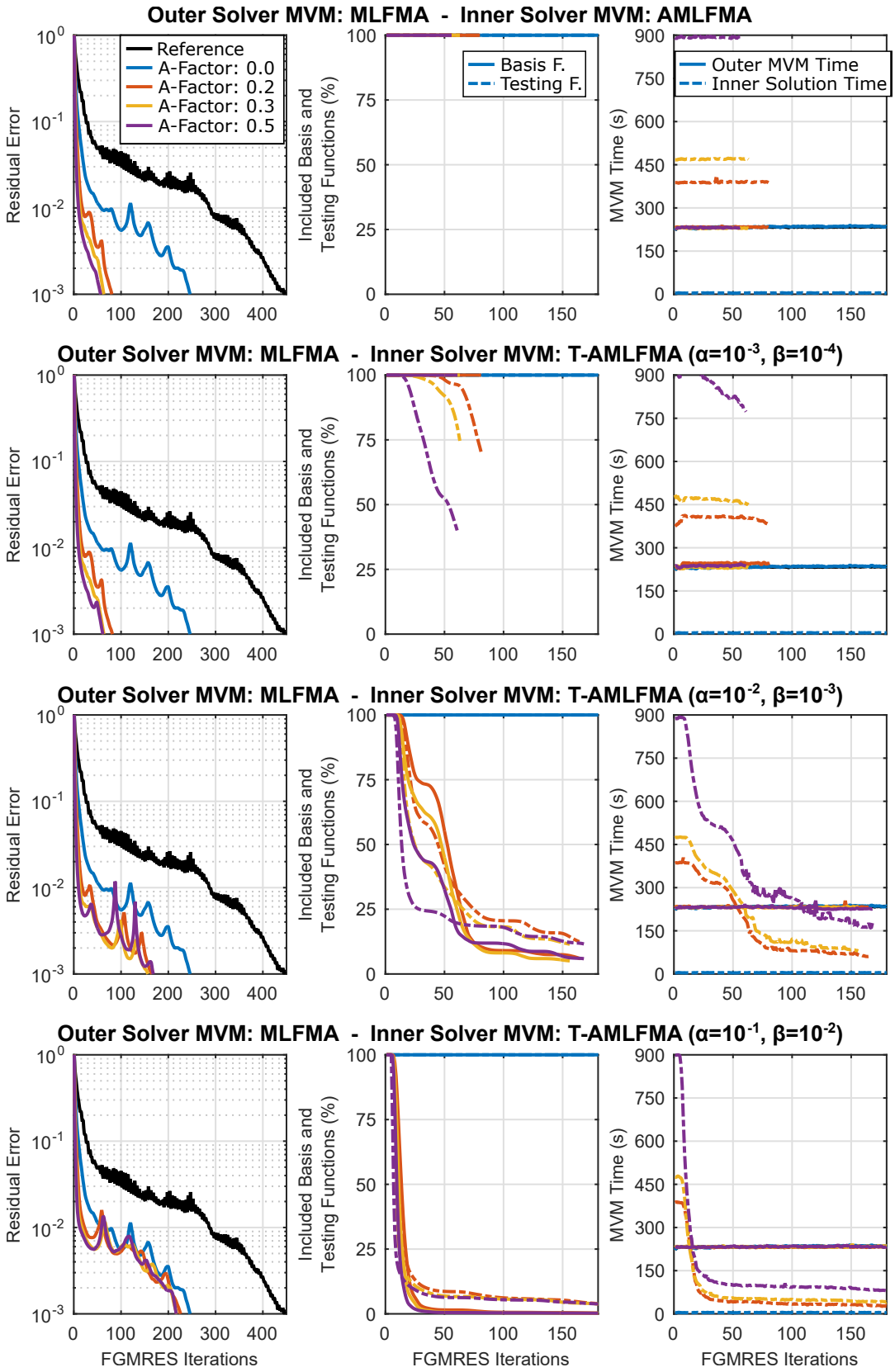

Figure 4.29: Solutions of a scattering problem involving the aircraft geometry by using regular MLFMA and T-AMLFMA.

Table 4.21: Details of the Simulations Involving the Aircraft Geometry Using T-MLFMA and T-AMLFMA Preconditioner

Method	A-Factor	Trimming Error	Current Error (%)	Far-Field Error (%)	Number of Iter.	Solution Time (h)
Ref.	-	-	-	-	448	28.6
T-MLFMA	0	0.1/0.05	31.9	4.79	22	1.10
T-MLFMA	0.2	0.1/0.05	24.2	2.97	14	1.85
T-MLFMA	0.3	0.1/0.05	23.2	3.29	12	1.85
T-MLFMA	0.5	0.1/0.05	22.5	2.19	11	2.57

Table 4.22: Details of the Simulations Involving The Aircraft Geometry With Electrical Size of 51.9λ Using Regular MLFMA (for Outer Solutions) and T-AMLFMA (for Inner Solutions)

Method	A-Factor	Trimming Error	Current Error (%)	Far-Field Error (%)	Number of Iter.	Solution Time (h)
Ref.	-	-	-	-	448	28.6
MLFMA	0	-	1.39	0.36	246	16.4
MLFMA	0.2	-	2.11	0.36	81	13.9
MLFMA	0.3	-	2.87	0.35	64	12.3
MLFMA	0.5	-	3.31	0.36	57	17.6
MLFMA	0.2	0.001/0.0001	2.14	0.37	82	14.6
MLFMA	0.3	0.001/0.0001	2.87	0.35	64	12.3
MLFMA	0.5	0.001/0.0001	3.06	0.35	62	18.8
MLFMA	0.2	0.01/0.001	1.65	0.35	166	18.5
MLFMA	0.3	0.01/0.001	1.69	0.35	157	19.2
MLFMA	0.5	0.01/0.001	1.82	0.35	169	27.6
MLFMA	0.2	0.1/0.01	1.89	0.35	226	18.2
MLFMA	0.3	0.1/0.01	1.43	0.35	219	18.6
MLFMA	0.5	0.1/0.01	1.59	0.36	217	22.0

are presented. The surface current errors and the far-zone scattering errors are all significantly small since we use regular MLFMA in the outer solver. The numbers of iterations and the solution times for the T-AMLFMA preconditioner with a low trimming threshold are similar to those obtained with the AMLFMA preconditioner with

the same A-Factor values. However, as we increase the trimming threshold, the T-AMLFMA preconditioner becomes an AMLFMA preconditioner with the A-Factor value of 0, which corresponds to using the near-zone matrix for the inner solutions. For higher trimming thresholds, the tree structure of T-AMLFMA becomes sparse quite rapidly with significant numbers of omitted far-zone interactions. Therefore, MVMs of the inner solutions only include near-zone interactions. This process can also be observed in the iterative convergence results in Figure 4.29. The T-AMLFMA preconditioner turns into the near-zone interactions, independently of the A-Factor value.

As a result, we conclude that T-AMLFMA can be used as a strong preconditioner for T-MLFMA solutions. We obtain 2.4 times acceleration in the solution time compared to T-MLFMA without preconditioning in Table 4.18, while we also obtain 11.2 times acceleration in the solution time compared to the fastest solutions with the AMLFMA preconditioner in Table 4.22. However, we observe that T-AMLFMA is not a suitable preconditioner for MLFMA.

CHAPTER 5

OTHER APPLICATIONS

In this chapter, we present two of our works in the scope of ML-aided electromagnetic simulations. The first section shows visual surface current estimations at the early stages of iterative solutions using deep CNNs. In the second section, we present error prediction for scattered electromagnetic fields from electrically large geometries using ML.

5.1 Visual Result Prediction in Electromagnetic Simulations Using Machine Learning

Simulations of electrically large geometries require long solution durations, while meaningful visual results may be obtained at the early stages of a simulation, if the available information is intelligently used. In this section, we present deep residual CNN structures that can provide visual estimations of accurate solutions, which cannot be obtained otherwise, using approximate and coarse simulations. We train CNN models to use the surface current images obtained at the early stages of iterative solutions and to estimate the corresponding images of the final solutions. The structure of the CNN model for visual result prediction, training details of the CNN model, and numerical results are shown in the following subsections.

5.1.1 Surface Current Estimation

Despite the peak technology provided by MLFMA and similar fast algorithms, solutions of large-scale problems still require excessive processing times, while industrial applications often need faster simulations and even reasonable predictions of final results, e.g., surface currents induced on metallic surfaces as focused here, before fine

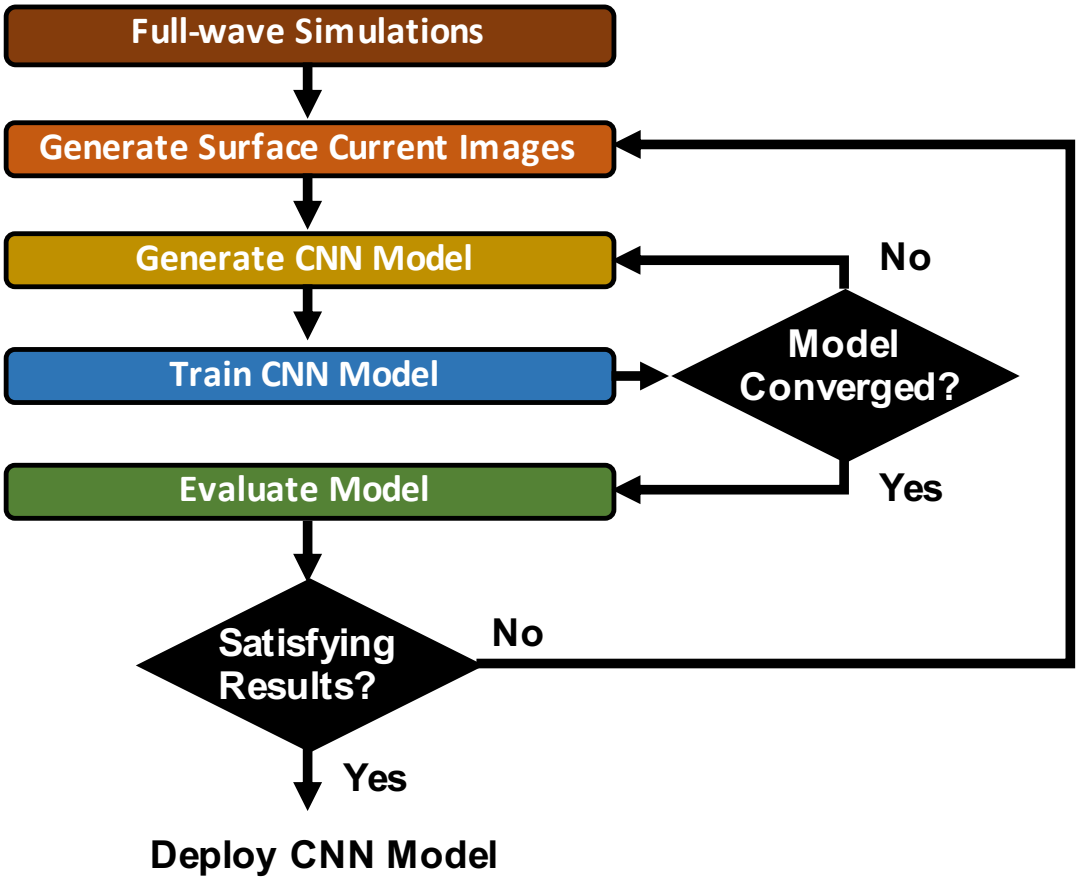

Figure 5.1: Workflow of the CNN model training for surface current estimation.

tunings in both design processes and simulations. Unavailability of this kind of information in most high-frequency techniques further necessitates the use of full-wave solvers as tools, while supporting them with new approaches like machine learning. Focusing on surface current density distributions, calculated currents at early iterations of a solution, which result in high residual errors (HREs) from the perspective of the iterative solver, can be considered as coarse and low-resolution images. On the other side, calculated surface currents at the end of an iterative solution, which gives the target low residual error (LRE), can be considered as a high-resolution image. By using the well-established concepts in the super-resolution studies, we propose a surface current estimation method to predict LRE images from HRE images.

The proposed surface current estimation method includes CNN models, which must be carefully built and trained. A workflow to obtain a successful CNN model is given

in Figure 5.1. The first step is to create a sufficiently large raw dataset for the training process, which directly affects the overall performance of the model. For this purpose, many full-wave simulations are performed to obtain HRE solutions, as well as large numbers of LRE solutions, to be saved. Then, we follow a nested loop procedure to (1) generate image dataset of surface currents for training and (2) generate and train the CNN model. In the inner loop (generating the CNN model), the network parameters, such as the length and width of the constructed layers, are determined. If the trained model cannot sufficiently validate the given dataset, the network parameters are manually changed. In the outer loop (generating image dataset), images including appropriate representations of surface currents are determined. If the trained model cannot make sufficiently successful predictions for the trials in the evaluation dataset, which are not included in the training dataset, the whole image set is reproduced by manually changing the orientation and color representation. We note that such updates do not require new electromagnetic simulations.

The operations above are carefully performed until the trained CNN model provides satisfactory image predictions. We note that the constructed CNN structures do not guarantee perfect estimations of all current distributions and they are naturally prone to mistakes particularly at difficult locations, such as sharp edges and corners; but, the quality of estimations can be improved by using larger datasets to train these networks at the cost of increased computational loads. While this trade-off between the preciseness and the efficiency can be considered depending on the application, our results show that the constructed CNN structures can be excellent to predict general aspects of current distributions rather than providing pointwise accuracy. This kind of predictions can be crucial for large-scale scatterers, particularly in radar scenarios, where geometric modifications on targets must be tested quickly before long-term detailed analyses. Specifically, the developed CNN structures can provide extremely fast but essential information on the distribution of the current density, e.g., locations for high current density values, that may allow engineers to quickly test geometric modifications.

5.1.2 Numerical Results

In this part, we present the application of the workflow described in the previous subsection via numerical examples. First, details of raw and image datasets are shared, followed by model parameters of a CNN. Then, sample results for surface current estimations by the trained CNN model are presented. All results involve electromagnetic scattering problems involving metallic objects in the frequency domain. Surfaces are discretized with λ/10 triangular elements, where λ is the wavelength of the host medium (vacuum). GMRES iterative solver is used to solve matrix equations, while the matrix-vector multiplications are performed via MLFMA with 1% maximum error.

In the constructed raw dataset, NASA Almond geometry ($16\lambda \times 128$, $32\lambda \times 64$, $64\lambda \times 64$), Flamme geometry ($16\lambda \times 128$, $32\lambda \times 64$, $64\lambda \times 64$), cube geometry ($16\lambda \times 8$, $32\lambda \times 8$), and sphere geometry ($16\lambda \times 1$, $32\lambda \times 1$, $64\lambda \times 1$) are considered. Therefore, the raw dataset consists of $256+256+16+3 = 531$ full-wave simulations. In each solution, the geometry is illuminated via a plane wave with random propagation and polarization. This way, diverse surface current distributions are obtained on the geometries. During the iterative solutions, HRE and LRE thresholds are used as 0.3 and 0.001, respectively. Absolute surface current density values are plotted using a linear scale between 0 and 15 mA/m to construct the image dataset. The surface current distributions obtained with HRE and LRE solutions are viewed from six different angles; left, right, front, back, top, and bottom. The view plots are adjusted according to the electrical sizes of the geometries by using 8 pixels per wavelength. Then, all images are divided into 64×64-pixel (smaller) RGB images to construct compact input and output data for the training stage. Empty zones that do not contain any solution information (geometry surface) are automatically discarded by assigning black color to the related pixels. As a consequence of all these operations, the final image dataset consists of 29,636 nonempty 64×64-pixel RGB images.

The general structure of the CNN model presented here is inspired by the model given in [106], whereas an overview of the model is shown in Figure 5.2. The model requires an arbitrary-sized HRE input image and provides an LRE image prediction of the same size. At each layer, 2D convolutions with 5×5 kernels are performed.

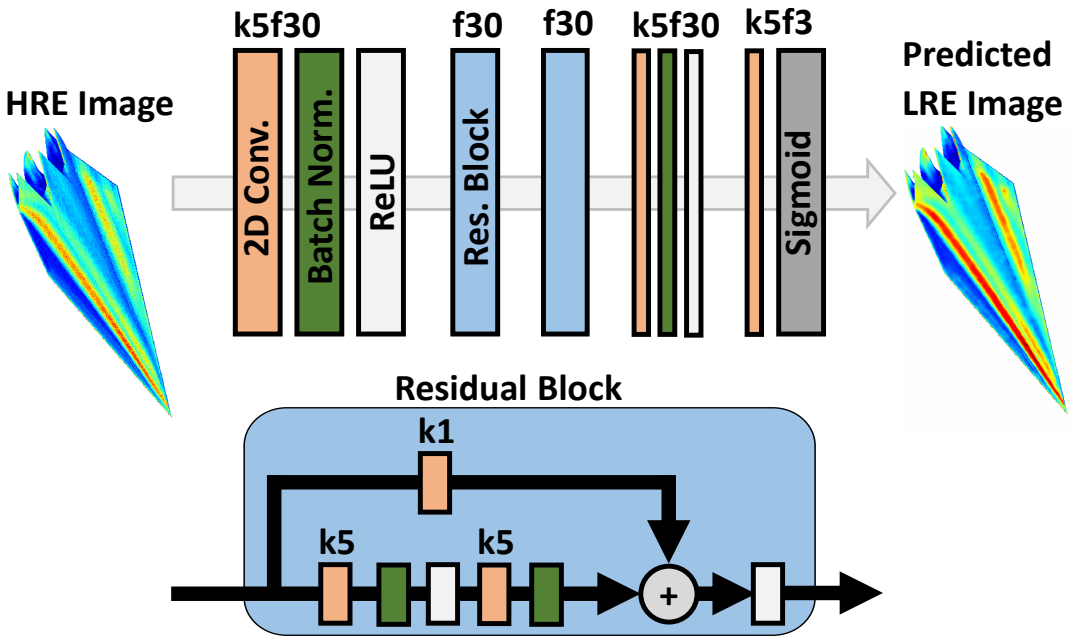

Figure 5.2: A block diagram of the CNN structure used for visual surface current estimation. Details of each layer are given as initials, i.e., k represents the size of convolution kernels and f represents the number of convolution filters.

Each convolutional layer, except the output layer, contains 30 filters. The convolution layers are followed by rectified linear unit (ReLU) activation functions. Batch normalization is applied right before each ReLU to balance the data on the main branch. At the output layer, the model is terminated by a sigmoid function to keep the output image values bounded. The residual blocks used in this model contains three convolution layers, one of which makes a shortcut. At the end of a residual block, the main and shortcut branches are added in an element-wise manner and forwarded to an ReLU. We note that the overall model, including two residual blocks, consists of seven layers. The model is trained via the Adam optimizer [104] by using mean-absolute-error loss function.

The image dataset is shuffled and split into training and validation sets. In the following results, the training set contains 90% of the dataset, whereas the remaining 10% is used for validation. The CNN model is trained for 500 epochs until the training and validation loss function values stagnate. The model is further validated on complete images after the training. We note that, although the training is performed on

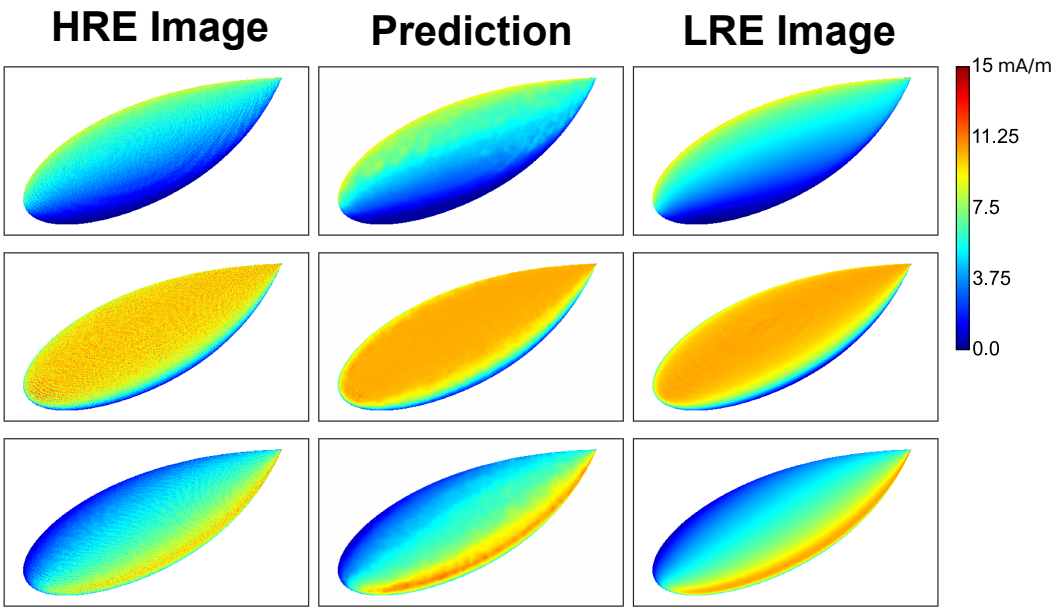

Figure 5.3: Surface current estimation for 64λ NASA Almond geometry.

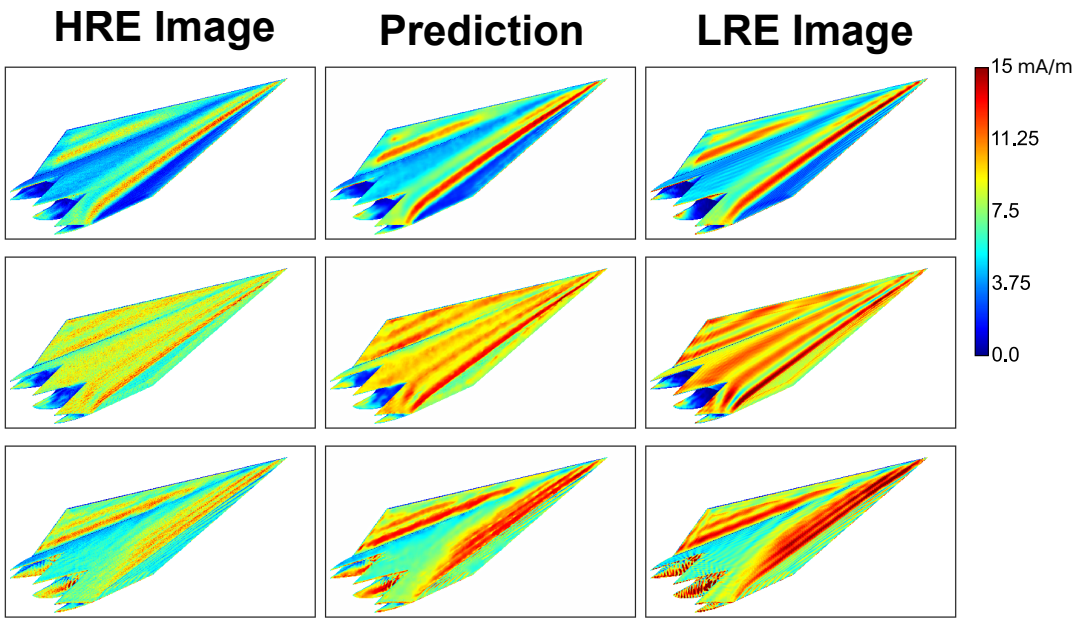

Figure 5.4: Surface current estimation for 64λ Flamme geometry.

64×64-pixel images, the deployed model can work on arbitrary image sizes. As an example to processing times, the final model evaluates a single 512×512-pixel RGB image in 880 ms using a single core of a CPU. Some prediction examples for the 64λ NASA Almond geometry are given in Figure 5.3. In this figure, the rows include solutions for different illuminations, while the columns include HRE solutions, LRE predictions, and LRE solutions, respectively. The relative tensor norm errors between LRE images and HRE images are 16.4%, 19.8%, and 20.9%, while the corresponding prediction errors are 9.8%, 7.8%, and 7.1%. The CNN model also provides visual improvements, such as better representations of the low-high current transition zones and and high-current regions, which are not clearly visible in the HRE images.

As a second set of numerical examples, 64λ Flamme geometry is considered in Figure 5.4. The relative tensor norm errors between LRE images and HRE images are 34.7%, 46.8%, and 50.5%, while the corresponding prediction errors are 18.0%, 29.4%, and 29.5%. Although the HRE images (obtained with the full-wave solver as references) are significantly different from the LRE images, the predictions provide better representations of the current distribution on the nose, at the back, and at the top of the Flamme geometry. As a comparison in terms of computational requirements, a complete full-wave simulation of the Flamme geometry requires 7.6 hours (100 iterations), whereas the corresponding HRE solution required by the CNN model can be obtained in only 18 minutes (4 iterations).

5.2 Error Prediction in Electromagnetic Simulations Using Machine Learning

In this section, we present a novel approach of using deep residual CNN structures to predict electromagnetic scattering error levels in iterative solutions of large-scale objects. We train deep residual CNN models to use the surface current images at the iterative solutions to estimate the electromagnetic far-zone scattering error levels. Therefore, we can use the result of the CNN models as an alternative error criteria for the iterative solutions. The simulation environment, the details of the training dataset, and the numerical results are presented in the following subsections.

5.2.1 Simulation Environment

In this part, machine learning is again applied within a simulation environment based on surface integral equations for metallic objects in the frequency domain. Problems are formulated by using CFIE, which is discretized by using the RWG functions on $\lambda/10$ discretizations, where λ is the wavelength in the host medium. Obtained dense matrix equations are solved iteratively using GMRES until 10^{-3} residual error is reached. Matrix-vector multiplications required for iterations are accelerated via MLFMA with 1% maximum error. Iterative convergences are further accelerated by using BDP.

5.2.2 Details of Data Set and CNN Model

Now, we briefly consider important details of dataset generation and deep CNN models, before sample training results.

In order to train a deep learning system, a considerably large data set is required. In the following results, more than 500 full-wave solutions are studied. In these solutions, NASA Almond (16λ, 32λ, 64λ), Flamme (16λ, 32λ, 64λ), and cube (16λ, 32λ) geometries are considered. In each iterative-solution stage, the coefficient vector is saved for all iterations. Thus, more than 30,000 coefficient vectors are obtained to generate the dataset. Then, these coefficient vectors are used as both input and output. For the input, surface current distributions are viewed from six different angles; top, bottom, left, right, front, and back. Then, these plots are combined in a single 256×256 pixel RGB image. Images are saved in pairs by combining the results of consecutive iterations. In order to prevent layout duplication in the input set, image pairs are randomly rotated. For the output set, forward-scattered electric field values are calculated by using coefficient vectors. Then, complex relative errors in forward scattering are calculated, by using the final forward-scattering value as reference. In order to finalize the output set, a threshold value is applied on the forward-scattering values. An error level above the threshold is set as zero, else is set as one. For the rest of this section, the threshold value is considered as 1% forward-scattering error.

The main purpose of the developed CNN model is predicting whether the forward-

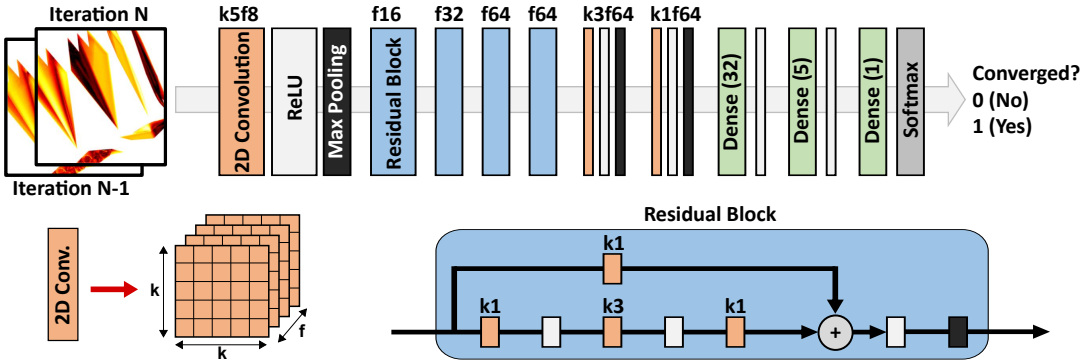

Figure 5.5: A block diagram of the deep CNN structure used for error prediction in electromagnetic simulations. Details of each layer are given as initials, i.e., k represents the size of convolution kernels and f represents the number of convolution filters.

scattering error level is below the given threshold or not by investigating surface current images of two consecutive iterations. Therefore, a classification network is required for this task. Since convolutional structures provide successful results for classification and association tasks, a deep CNN model is constructed, as described in Figure 5.5. The CNN model requires two RGB images (six frames) and gives a binary output. It starts with a 2D convolution layer, followed by four residual blocks. Then, two more 2D convolution layers and three fully connected layers are stacked consecutively, which makes a total of 18 layers in the model. Rectified linear unit (ReLU) is used as the activation function. The network is finalized with a softmax function due to the classification task. After ReLU or a residual block, maxpooling is applied to downsample the considered frame into half from both vertical and horizontal axis. The residual block in this model consists of four convolution layers. One of layers makes a shortcut branch starting from the beginning of the residual block and it is reconnected to the main branch after the third convolution layer. The frames of the main and shortcut branches are added in an element-wise manner. During training, categorical cross-entropy loss function and Adam optimizer are used.

The data set is split into two as training and validation sets. The training set consists of 90% of the data set, while the remaining 10% is used for validation to check the convergence of the model during the training. The model is trained for only 100

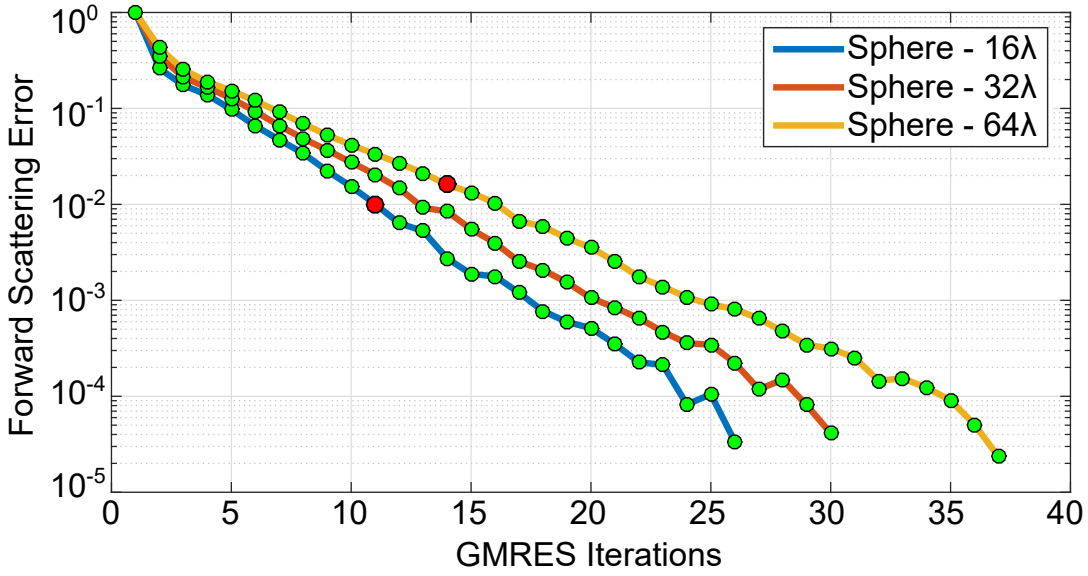

Figure 5.6: Forward-scattering error predictions with respect to GMRES iterations for sphere geometries of size 16λ, 32λ, and 64λ.

epochs to reach 95.76% training accuracy and 95.4% validation accuracy. For further validation, sphere geometry, which is not included in the training data set, is considered. Current images of surface currents on 16λ, 32λ, and 64λ spheres are given to the trained network and forward-scattering error is predicted (whether it is above 1% or not). Forward-scattering errors and predictions based on the trained model are given in Figure 5.6. Solid lines represent forward-scattering errors, while circular markers specify predictions. Green markers and red markers indicate the correct and failed predictions, respectively. We observe that the trained CNN model provides very accurate predictions, while it only mispredicts in the threshold region.

CHAPTER 6

CONCLUSION

We present novel approaches to accelerate MLFMA solutions of three-dimensional electromagnetic problems. As the major contribution, we consider the integration of an ML technique into MLFMA to generate efficient tree structures. Specifically, during iterative solutions, electromagnetic interactions are systematically eliminated, leading to faster matrix-vector multiplications as iterations continue, whereas iterative convergences are also improved as a result of the sparsification. For eliminating matrix columns, basis functions (converged current coefficients) are estimated via ML techniques that are integrated into the MLFMA solver. By also eliminating matrix rows, i.e., testing functions, based on more straightforward checks with the right-hand-side elements, impedance matrices become increasingly sparser as iterations continue. Reduced numbers of iterations and decreased MVM (per iteration) times lead to significant accelerations in terms of overall solution times. Numerical results on complex structures show that electromagnetic interactions can significantly be eliminated, and the resulting T-MLFMA implementation can provide as much as 10 times acceleration in comparison to the conventional MLFMA.

We also demonstrate a novel ML approach to visually estimate solutions of electromagnetic problems using CNN models. The models are trained to use surface current pictures obtained at the early stages of iterative solutions and predict the corresponding images of final solutions. Initial experiments show that the proposed estimation methodology provides promising results, while it is also open to improvements, particularly with new advances in ML strategies. The application of similar approaches for the estimation of scattered fields or quantities other than current distributions is also open for further research.

Finally, we show error prediction in electromagnetic simulations using deep CNN structures. As a particular example, a structure is trained by using surface current images to predict the error level in the forward scattering. Promising numerical experiments, showing successful predictions even for objects out of training sets, are obtained. This is the first time that ML is used for this kind of an error prediction to the best of our knowledge, while our initial results support the recent trend in seeking help from ML concepts in diverse ways to facilitate electromagnetic simulations.

REFERENCES

[1] W. Chew, E. Michielssen, J. M. Song, and J. M. Jin, *Fast and Efficient Algorithms in Computational Electromagnetics*. Norwood, MA, USA: Artech House, Inc., 2001.

[2] Ö. Ergül and L. Gürel, *The Multilevel Fast Multipole Algorithm (MLFMA) for Solving Large-Scale Computational Electromagnetics Problems*. Hoboken, NJ, USA: John Wiley & Sons, Ltd, 2014.

[3] J. R. Mautz and R. F. Harrington, "H-field, E-field, and combined field solutions for bodies of revolution," *Arch. Elektron. Ubertragungstech. (Electron. Commun.)*, vol. 32, pp. 157–164, 1978.

[4] S. Rao, D. Wilton, and A. Glisson, "Electromagnetic scattering by surfaces of arbitrary shape," *IEEE Trans. Antennas Propag.*, vol. 30, pp. 409–418, May 1982.

[5] K. Cools, F. P. Andriulli, D. De Zutter, and E. Michielssen, "Accurate and conforming mixed discretization of the MFIE," *IEEE Antennas Wireless Propag. Lett.*, vol. 10, pp. 528–531, 2011.

[6] Ö. Ergül and L. Gürel, "Linear-linear basis functions for MLFMA solutions of magnetic-field and combined-field integral equations," *IEEE Trans. Antennas Propag.*, vol. 55, pp. 1103–1110, Apr. 2007.

[7] E. Ubeda and J. M. Rius, "MFIE MoM-formulation with curl-conforming basis functions and accurate kernel integration in the analysis of perfectly conducting sharp-edged objects," *Microw. Opt. Technol. Lett.*, vol. 44, no. 4, pp. 354–358, 2005.

[8] M. Benzi and M. Tuma, "A sparse approximate inverse preconditioner for nonsymmetric linear systems," *SIAM Journal on Scientific Computing*, vol. 19, no. 3, pp. 968–994, 1998.

[9] Ö. Ergül, T. Malas, and L. Gürel, "Solutions of large-scale electromagnetics problems using an iterative inner-outer scheme with ordinary and approximate multilevel fast multipole algorithms," *Progress Electromagn. Res.*, vol. 106, pp. 203–223, 2010.

[10] C. Önol, A. Üçüncü, and Ö. Ergül, "Efficient multilayer iterative solutions of electromagnetic problems using approximate forms of the multilevel fast multipole algorithm," *IEEE Antennas Wireless Propag. Lett.*, vol. 16, pp. 3253–3256, 2017.

[11] Ö. Ergül and L. Gürel, "A hierarchical partitioning strategy for an efficient parallelization of the multilevel fast multipole algorithm," *IEEE Trans. Antennas Propag.*, vol. 57, pp. 1740–1750, Jun. 2009.

[12] B. Michiels, J. Fostier, I. Bogaert, and D. De Zutter, "Weak scalability analysis of the distributed-memory parallel MLFMA," *IEEE Trans. Antennas Propag.*, vol. 61, pp. 5567–5574, Nov. 2013.

[13] Y. Liu, A. C. Yücel, H. Bağcı, and E. Michielssen, "A scalable parallel PWTD-accelerated SIE solver for analyzing transient scattering from electrically large objects," *IEEE Trans. Antennas Propag.*, vol. 64, pp. 663–674, Feb. 2016.

[14] A. Krizhevsky, I. Sutskever, and G. E. Hinton, "Imagenet classification with deep convolutional neural networks," in *Proc. Adv. Neural Inf. Process. Syst*, pp. 1097–1105, 2012.

[15] J. Long, E. Shelhamer, and T. Darrell, "Fully convolutional networks for semantic segmentation," in *Proc. IEEE Conf. Comput. Vis. Pattern Recognit.*, pp. 3431–3440, Jun. 2015.

[16] C. Dong, C. C. Loy, K. He, and X. Tang, "Image super-resolution using deep convolutional networks," *IEEE Trans. Pattern Anal. Mach. Intell.*, vol. 38, pp. 295–307, Feb. 2016.

[17] B. Liu, H. Aliakbarian, Z. Ma, G. A. E. Vandenbosch, G. Gielen, and P. Excell, "An efficient method for antenna design optimization based on evolutionary computation and machine learning techniques," *IEEE Trans. Antennas Propag.*, vol. 62, pp. 7–18, Jan. 2014.

[18] J. Tak, A. Kantemur, Y. Sharma, and H. Xin, "A 3-D-printed W-band slotted waveguide array antenna optimized using machine learning," *IEEE Antennas Wireless Propag. Lett.*, vol. 17, pp. 2008–2012, Nov 2018.

[19] B. Karaosmanoğlu and Ö. Ergül, "Visual result prediction in electromagnetic simulations using machine learning," *IEEE Antennas Wireless Propag. Lett.*, vol. 18, pp. 2264–2266, 2019.

[20] H. M. Yao, W. E. I. Sha, and L. J. Jiang, "Applying convolutional neural networks for the source reconstruction," *Progress Electromagn. Res. M*, vol. 76, pp. 91–99, 2018.

[21] D. Yun, I. I. Jung, H. Jung, H. Kang, W. Yang, and I. Y. Park, "Improvement in computation time of the finite multipole method by using k-means clustering," *IEEE Antennas Wireless Propag. Lett.*, vol. 18, pp. 1814–1817, Sep. 2019.

[22] A. Khan, V. Ghorbanian, and D. Lowther, "Deep learning for magnetic field estimation," *IEEE Trans. Magn.*, vol. 55, pp. 1–4, Jun. 2019.

[23] B. Karaosmanoğlu and Ö. Ergül, "Error prediction in electromagnetic simulations using machine learning," in *Proc. IEEE Antennas and Propagation Soc. Int. Symp.*, 2019.

[24] R. F. Harrington, *Field computation by moment methods*. New York: Macmillan, 1968.

[25] W. C. Gibson, *Method of moments in electromagnetics*. Boca Raton, FL: Chapman and Hall/CRC, 2007.

[26] D. A. Dunavant, "High degree efficient symmetrical gaussian quadrature rules for the triangle," *Int. J. Numer. Meth. Eng.*, vol. 21, no. 6, pp. 1129–1148, 1985.

[27] D. R. Wilton, S. M. Rao, A. W. Glisson, D. Schaubert, O. M. Al-Bundak, and C. Butler, "Potential integrals for uniform and linear source distributions on polygonal and polyhedral domains," *IEEE Trans. Antennas Propag.*, vol. 32, pp. 276–281, Mar. 1984.

[28] R. D. Graglia, "On the numerical integration of the linear shape functions times

the 3-D green's function or its gradient on a plane triangle," *IEEE Trans. Antennas Propag.*, vol. 41, pp. 1448–1455, Oct. 1993.

[29] V. Rokhlin, "Rapid solution of integral equations of scattering theory in two dimensions," *J. Comput. Phys.*, vol. 86, pp. 414–439, Feb. 1990.

[30] R. Coifman, V. Rokhlin, and S. Wandzura, "The fast multipole method for the wave equation: A pedestrian prescription," *IEEE Antennas Propag. Mag.*, vol. 35, pp. 7–12, Jun. 1993.

[31] X. Q. Sheng, J.-M. Jin, J. Song, W. C. Chew, and C.-C. Lu, "Solution of combined-field integral equation using multilevel fast multipole algorithm for scattering by homogeneous bodies," *IEEE Trans. Antennas Propag.*, vol. 46, pp. 1718–1726, Nov. 1998.

[32] S. Koc, J. Song, and W. C. Chew, "Error analysis for the numerical evaluation of the diagonal forms of the scalar spherical addition theorem," *SIAM J. Numer. Anal.*, vol. 36, no. 3, pp. 906–921, 1999.

[33] A. Brandt, "Multilevel computations of integral transforms and particle interactions with oscillatory kernels," *Comput. Phys. Comm.*, vol. 65, pp. 24–38, Apr. 1991.

[34] B. Karaosmanoğlu and Ö. Ergül, "Modified combined tangential formulation for stable and accurate analysis of plasmonic structures," *ACES Exp.*, vol. 34, pp. 811–814, May. 2019.

[35] B. Karaosmanoğlu, A. Yılmaz, and Ö. Ergül, "A comparative study of surface integral equations for accurate and efficient analysis of plasmonic structures," *IEEE Trans. Antennas Propag.*, vol. 64, pp. 3049–3057, Jun. 2017.

[36] B. Karaosmanoğlu and Ö. Ergül, "Accuracy of the surface integral-equation formulations for large negative permittivity values," in *Proc. Progress in Electromagnetics Research Symp. (PIERS)*, pp. 926–933, 2017.

[37] B. Karaosmanoğlu and Ö. Ergül, "Modified combined tangential formulation for stable and accurate analysis of plasmonic structures," in *Proc. Int. Applied Computational Electromagnetics Soc. Symp.*, 2017.

[38] B. Karaosmanoğlu and Ö. Ergül, "On the accuracy and efficiency of surface formulations in fast analysis of plasmonic structures via MLFMA," in *Proc. Progress in Electromagnetics Research Symp. (PIERS)*, pp. 2629–2633, 2016.

[39] Y. Koyaz, H. İbili, B. Karaosmanoğlu, and Ö. Ergül, "Analysis of composite structures involving near-zero-index materials," in *Proc. Int. Conf. on Microwaves, Communications, Antennas, and Electronic Systems (IEEE COMCAS)*, 2019.

[40] B. Karaosmanoğlu, Y. Koyaz, H. İbili, and Ö. Ergül, "Fast and accurate analysis of three-dimensional structures involving near-zero-index materials," in *Proc. Int. Conf. on Electromagnetics in Advanced Applications (ICEAA)*, pp. 1019–1024, 2019.

[41] B. Karaosmanoğlu, U. Özmü, and Ö. Ergül, "Novel SIE formulations for accurate and stable analysis of near-zero-index materials," in *Proc. IEEE Antennas and Propagation Soc. Int. Symp.*, 2019.

[42] H. İbili, Y. Koyaz, U. Özmü, B. Karaosmanoğlu, and Ö. Ergül, "Novel SIE implementations for efficient and accurate electromagnetic simulations of zero-index materials," in *Proc. Progress in Electromagnetics Research Symp. (PIERS)*, 2019.

[43] B. Karaosmanoğlu and Ö. Ergül, "Generalized hybrid surface integral equations for finite periodic perfectly conducting objects," *IEEE Antennas Wireless Propag. Lett.*, vol. 16, pp. 1068–1071, 2017.

[44] B. Karaosmanoğlu, M. Tonga, and Ö. Ergül, "A broadband electromagnetic solver based on multiscale MLFMA and hybrid integral equations," in *Proc. Mediterranean Microwave Symp. (MMS)*, pp. 97–100, 2018.

[45] B. Karaosmanoğlu and Ö. Ergül, "Improving the accuracy of MFIE and CFIE by using numerically designed testing functions," in *Proc. IEEE Antennas and Propagation Soc. Int. Symp.*, pp. 317–318, 2016.

[46] Ö. Ergül, C. Önol, and B. Karaosmanoğlu, "Optimizations of EFIE and MFIE combinations in hybrid formulations of conducting bodies," in *Proc. Int.*

Conf. on Electromagnetics in Advanced Applications (ICEAA), pp. 1276–1279, 2015.

[47] B. Karaosmanoğlu and Ö. Ergül, "Hybrid surface integral equations for optimal analysis of perfectly conducting bodies," in *Proc. IEEE Antennas and Propagation Soc. Int. Symp.*, pp. 1160–1161, 2015.

[48] B. Karaosmanoğlu and Ö. Ergül, "EFIE-tuned testing functions for MFIE and CFIE," *IEEE Antennas Wireless Propag. Lett.*, vol. 16, pp. 968–970, 2017.

[49] B. Karaosmanoğlu, A. Altınoklu, and Ö. Ergül, "Numerical constructions of testing functions for improving the accuracy of MFIE and CFIE," *Prog. Electromagn. Res. M*, vol. 51, pp. 63–70, Oct. 2016.

[50] B. Karaosmanoğlu and Ö. Ergül, "Numerical design of testing functions for the magnetic-field integral equation," in *Proc. European Conf. on Antennas and Propagation (EuCAP)*, 2016.

[51] B. Karaosmanoğlu and Ö. Ergül, "Design of numerical testing functions for the magnetic-field integral equation," in *Turkish, URSI-Turkey Scientific Symp.*, 2016.

[52] Ö. Ergül and B. Karaosmanoğlu, "Broadband multilevel fast multipole algorithm based on an approximate diagonalization of the green's function," *IEEE Trans. Antennas Propag.*, vol. 63, pp. 3035–3041, Jul. 2015.

[53] Ö. Ergül and B. Karaosmanoğlu, "Approximate stable diagonalization of the green's function for low frequencies," *IEEE Antennas Wireless Propag. Lett.*, vol. 13, pp. 1054–1056, 2014.

[54] U. M. Gür, I. C. Çetin, B. Karaosmanoğlu, and Ö. Ergül, "PIE-MLFMA implementation for solving complex subwavelength electromagnetic problems," in *Proc. IEEE MTT-S Int. Conf. Numerical Electromagnetic and Multiphysics Modeling and Optimization (NEMO)*, 2018.

[55] U. M. Gür, B. Karaosmanoğlu, and Ö. Ergül, "Solutions of new potential integral equations using approximate stable diagonalization of the Green's function," in *Proc. Int. Conf. on Electromagnetics in Advanced Applications (ICEAA)*, pp. 1894–1897, 2017.

[56] U. M. Gür, B. Karaosmanoğlu, and Ö. Ergül, "Fast-multipole-method solutions of new potential integral equations," in *Proc. Fourth International EMC Conference*, 2017.

[57] B. Karaosmanoğlu, A. Yılmaz, and Ö. Ergül, "Development and application of a broadband multilevel fast multipole algorithm for challenging multiscale problems," in *Proc. Progress in Electromagnetics Research Symp. (PIERS)*, pp. 4713–4716, 2016.

[58] Ö. Ergül, B. Karaosmanoğlu, M. Takrimi, and V. B. Ertürk, "Broadband multilevel fast multipole algorithm for large-scale problems with nonuniform discretizations," in *Proc. Int. Symp. on Electromagnetic Theory (EMTS)*, pp. 284–287, 2016.

[59] Ö. Ergül and B. Karaosmanoğlu, "Broadband MLFMA based on an approximate diagonalization of the three-dimensional green's function," in *Proc. Int. Conf. on Electromagnetics in Advanced Applications (ICEAA)*, pp. 1272–1275, 2015.

[60] Ö. Ergül and B. Karaosmanoğlu, "Low-frequency multilevel fast multipole algorithm using an approximate diagonalization of the green's function," in *Proc. XXXI URSI General Assembly and Scientific Symp. of Int. Union of Radio Science*, 2014.

[61] B. Karaosmanoğlu and Ö. Ergül, "Broadband implementation of MLFMA using approximate scaled diagonalization of the green's function," in *URSI Atlantic Radio Science Conf. (URSI AT-RASC)*, May 2015.

[62] B. Karaosmanoğlu and Ö. Ergül, "A broadband multilevel fast multipole algorithm based on the scaled diagonalization of the green's function," in *Turkish, URSI-Turkey Scientific Symp.*, 2014.

[63] Ö. Ergül and B. Karaosmanoğlu, "Low-frequency fast multipole method based on multiple-precision arithmetic," *IEEE Antennas Wireless Propag. Lett.*, vol. 13, pp. 975–978, 2014.

[64] Ö. Ergül and B. Karaosmanoğlu, "Using multiple-precision arithmetic to prevent low-frequency breakdowns in the diagonalization of the green's function,"

in *Proc. Progress in Electromagnetics Research Symp. (PIERS)*, pp. 2311–2315, 2014.

[65] B. Karaosmanoğlu and Ö. Ergül, "Stabilization of the fast multipole method for low frequencies using multiple-precision arithmetic," in *Proc. XXXI URSI General Assembly and Scientific Symp. of Int. Union of Radio Science*, 2014.

[66] C. Önol, A.Üçüncü, B. Karaosmanoğlu, and Ö. Ergül, "Nested iterative solutions of electromagnetic problems using approximate forms of the multilevel fast multipole algorithm," in *Proc. European Conf. on Antennas and Propagation (EuCAP)*, pp. 1109–1112, 2017.

[67] B. Karaosmanoğlu, C. Önol, S. Güler, A. Altınoklu, and Ö. Ergül, "Full-wave electromagnetic optimizations using surface integral equations and the multilevel fast multipole algorithm," in *Proc. Progress in Electromagnetics Research Symp. (PIERS)*, pp. 262–266, 2016.

[68] Y. E. Tunçyürek, B. Karaosmanoğlu, and Ö. Ergül, "Computational design of optical couplers for bended nanowire transmission lines," *ACES J.*, vol. 32, pp. 562–568, Jul. 2017.

[69] B. Karaosmanoğlu, A. Yılmaz, U. M. Gür, and Ö. Ergül, "Solutions of plasmonic structures using the multilevel fast multipole algorithm," *Special Issue on Challenges in RF and Microwave Defense Engineering, Int. J. RF Microwave Comput.-Aided. Eng.*, vol. 26, pp. 335–341, May 2016.

[70] B. Karaosmanoğlu, A. Yılmaz, and Ö. Ergül, "Computational electromagnetic analysis of deformed nanowires using the multilevel fast multipole algorithm," *Sci. Rep.*, vol. 5, Feb. 2015.

[71] H. A. Şatana, B. Karaosmanoğlu, and Ö. Ergül, "A comparative study of nanowire arrays for maximum power transmission," in *Nanowires* (K. Maaz, ed.), pp. 233–253, InTech, 2017.

[72] A. Çekinmez, B. Karaosmanoğlu, and Ö. Ergül, "Integral-equation formulations of plasmonic problems in the visible spectrum and beyond," in *Dynamical Systems-Analytical and Computational Techniques* (M. Reyhanoglu, ed.), pp. 191–214, InTech, 2017.

[73] B. Karaosmanoğlu, H. A. Şatana, F. Dikmen, and Ö. Ergül, "Investigation of alternative array configurations of nanowires for maximum power transmission at optical frequencies," in *Proc. IEEE Antennas and Propagation Soc. Int. Symp.*, pp. 123–124, 2017.

[74] A. Yılmaz, B. Karaosmanoğlu, and Ö. Ergül, "Analysis of optical properties of nanowires using surface integral equations and the multilevel fast multipole algorithm," in *Proc. Advanced Electromagnetic Symp.*, 2016.

[75] B. Karaosmanoğlu, A. Yılmaz, and Ö. Ergül, "Full-wave analysis of three-dimensional optical metamaterials involving deformed nanowires," in *Proc. Int. Cong. on Advanced Electromagnetic Materials in Microwaves and Optics (Metamaterials)*, pp. 136–138, 2015.

[76] B. Karaosmanoğlu, A. Yılmaz, and Ö. Ergül, "Rigorous analysis of deformed nanowires using the multilevel fast multipole algorithm," in *Proc. European Conf. on Antennas and Propagation (EuCAP)*, 2015.

[77] B. Karaosmanoğlu, A. Yılmaz, and Ö. Ergül, "Fast and accurate analysis of plasmonic structures at optical frequencies using the multilevel fast multipole algorithm," in *Turkish, URSI-Turkey Scientific Symp.*, 2016.

[78] B. Karaosmanoğlu, A. Yılmaz, and Ö. Ergül, "Accurate full-wave simulations of nanowires at optical frequencies using the multilevel fast multipole algorithm," in *Nanoscience & Nanotechnology Conf. (NanoTR)*, (Ankara, Turkey), 2015.

[79] B. Karaosmanoğlu, A. Yılmaz, and Ö. Ergül, "Fast and accurate analysis of nanowires with the multilevel fast multipole algorithm," in *Turkish, URSI-Turkey Scientific Symp.*, 2014.

[80] Ş. Yazar, C. G. Sür, B. Solak, Ö. Eroğlu, A. Altınoklu, S. Güler, U. M. Gür, B. Karaosmanoğlu, and Ö. Ergül, "Computational electromagnetic analysis of deformed nanowires using the multilevel fast multipole algorithm," *Materials Science Forum*, vol. 915, pp. 202–206, Mar. 2016.

[81] H. İbili, S. Güler, B. Karaosmanoğlu, and Ö. Ergül, "Penetrable numerical

modeling of metallic nanoparticles at terahertz frequencies," in *Proc. Progress in Electromagnetics Research Symp. (PIERS)*, pp. 2273–2279, 2018.

[82] B. Karaosmanoğlu, A. Yılmaz, U. M. Gür, and Ö. Ergül, "Solutions of plasmonic structures using the multilevel fast multipole algorithm," in *Proc. Third International EMC Conference*, 2015.

[83] B. Karaosmanoğlu, U. M. Gür, and Ö. Ergül, "Investigation of nanoantennas using surface integral equations and the multilevel fast multipole algorithm," in *Proc. Progress in Electromagnetics Research Symp. (PIERS)*, pp. 2026–2030, 2015.

[84] B. Karaosmanoğlu, U. M. Gür, and Ö. Ergül, "Accurate analysis of nanoantennas with plasmonic properties using surface integral equations," in *Turkish, URSI-Turkey Scientific Symp.*, 2014.

[85] B. Karaosmanoğlu, E. Tuygar, U. Topçuoğlu, and Ö. Ergül, "Improving the efficiency of solar cells using antenna-inspired cavities," *Microw. Opt. Technol. Lett.*, vol. 61, pp. 1924–1930, Aug. 2019.

[86] B. Karaosmanoğlu, B. N. Bice, and Ö. Ergül, "Geometric improvements on solar cells for reducing reflections," in *Proc. IEEE Antennas and Propagation Soc. Int. Symp.*, 2019.

[87] B. Karaosmanoğlu, U. Topçuoğlu, S. Güler, E. Tuygar, and Ö. Ergül, "Optimal cavities to enhance freespace matching in solar cells," in *Proc. Progress in Electromagnetics Research Symp. (PIERS)*, pp. 48–52, 2018.

[88] B. Karaosmanoğlu, U. Topçuoğlu, E. Tuygar, and Ö. Ergül, "Numerical investigation of nanocavities for optimal power absorption in solar cells," in *URSI Atlantic Radio Science Meeting (AT-RASC)*, 2018.

[89] B. Karaosmanoğlu, H. Eray, and Ö. Ergül, "Full-wave optimization of three-dimensional photonic-crystal structures involving dielectric rods," *J. Opt. Soc. Am. A.*, vol. 37, pp. 1103–1113, Jul. 2018.

[90] B. Karaosmanoğlu, Ş. Yazar, and Ö. Ergül, "Design of compact nano-optical couplers involving dielectric nanorods," in *URSI Atlantic Radio Science Conf. (URSI AT-RASC)*, 2018.

[91] H. Eray, B. Karaosmanoğlu, and Ö. Ergül, "Full-wave electromagnetic optimizations of photonic crystals involving dielectric rods," in *Proc. Progress in Electromagnetics Research Symp. (PIERS)*, pp. 2871–2875, 2017.

[92] B. Karaosmanoğlu, Ş. Yazar, and Ö. Ergül, "Design of optical couplers via optimization of photonic crystal structures," in *Turkish, URSI-Turkey Scientific Symp.*, 2018.

[93] A. Altınoklu, B. Karaosmanoğlu, and Ö. Ergül, "Electromagnetic optimizations of corrugated metallic sheets for maximum power focusing," *J. Electromagn. Waves Appl.*, vol. 31, pp. 837–849, Apr. 2017.

[94] A. Altınoklu, B. Karaosmanoğlu, and Ö. Ergül, "Full-wave electromagnetic optimizations of corrugated metallic sheets," in *Proc. IEEE Antennas and Propagation Soc. Int. Symp.*, pp. 1325–1326, 2016.

[95] C. Önol, B. Karaosmanoğlu, and Ö. Ergül, "Efficient and accurate electromagnetic optimizations based on approximate forms of the multilevel fast multipole algorithm," *IEEE Antennas Wireless Propag. Lett.*, vol. 15, pp. 1113–1115, Apr. 2016.

[96] Ö. Ergül, B. Karaosmanoğlu, and C. Önol, "Electromagnetic optimizations using heuristic algorithms combined with the ordinary and approximate forms of the multilevel fast multipole algorithm," in *Proc. Int. Conf. on Matrix Methods in Mathematics and Applications (MMMA)*, pp. 37–38, 2015.

[97] C. Önol, B. Karaosmanoğlu, and Ö. Ergül, "Antenna switch optimizations using genetic algorithms accelerated with the multilevel fast multipole algorithm," in *Proc. IEEE Antennas and Propagation Soc. Int. Symp.*, pp. 1338–1339, 2015.

[98] H. İbili, B. Karaosmanoğlu, and Ö. Ergül, "Homogenization of microwave metamaterial structures using full-wave solutions and genetic algorithms," in *2018 18th Mediterranean Microwave Symposium (MMS)*, pp. 244–246, Oct. 2018.

[99] B. Karaosmanoğlu, H. İbili, and Ö. Ergül, "Homogenization of structures with

negative permeability using genetic algorithms," in *Turkish, URSI-Turkey Scientific Symp.*, 2018.

[100] B. Karaosmanoğlu, H. İbili, S. Güler, and Ö. Ergül, "Accurate solutions of electromagnetic problems involving very large targets," in *Turkish, 9th Congress of Defense Technologies*, pp. 913–917, 2018.

[101] B. Karaosmanoğlu and Ö. Ergül, "Computational electromagnetic simulations of electrically large structures," in *Workshop on Computational Science and Engineering (BEYOND)*, 2018.

[102] A. C. Woo, H. T. G. Wang, M. J. Schuh, and M. L. Sanders, "EM programmer's notebook-benchmark radar targets for the validation of computational electromagnetics programs," *IEEE Antennas and Propagation Magazine*, vol. 35, pp. 84–89, Feb. 1993.

[103] L. Gürel, H. Bağcı, J. C. Castelli, A. Cheraly, and F. Tardivel, "Validation through comparison: Measurement and calculation of the bistatic radar cross section of a stealth target," *Radio Science*, vol. 38, no. 3, 2003.

[104] D. P. Kingma and J. Ba, "Adam: A method for stochastic optimization," *arXiv preprint arXiv:1412.6980*, 2014.

[105] C. Önol and Ö. Ergül, "Optimizations of patch antenna arrays using genetic algorithms supported by the multilevel fast multipole algorithm," *Radioengineering*, vol. 23, pp. 1005–1014, Dec. 2014.

[106] C. Ledig, L. Theis, F. Huszar, J. Caballero, A. Cunningham, A. Acosta, A. Aitken, A. Tejani, J. Totz, Z. Wang, and W. Shi, "Photo-realistic single image super-resolution using a generative adversarial network," in *Proc. IEEE Conf. Comput. Vis. Pattern Recognit.*, Jul. 2017.

CURRICULUM VITAE

PERSONAL INFORMATION

Surname, Name: Karaosmanoğlu, Barışcan
Nationality: Turkish (TC)
Date and Place of Birth: 17.06.1987, İstanbul
Marital Status: Married
Phone: +90 535 2222157

EDUCATION

Degree	Institution	Year of Graduation
M.S.	Bilkent University	2013
B.S.	Doğus University	2011
High School	F.M.V Işık Lisesi	2005

PROFESSIONAL EXPERIENCE

Year	Place	Enrollment
2014–2019	CEMMETU/METU	Research Assistant
2013–2014	CEMMETU/METU	Project Engineer
2011–2013	BiLCEM/Bilkent University	Research Assistant
2011–2013	Dept. of EEE/Bilkent University	Teaching Assistant
2011–2011	BiLCEM/Bilkent University	Project Engineer

Honors & Awards

1. URSI - AT-RASC 2018 Young Scientist Award (International)
2. Council of Higher Education 100/2000 PhD Scholarship

3. METU EEE Graduate Research Workshop (GRW-2017) - 1st Place
4. URSI - Leopold B. Felsen Best Student Paper Award (National)
5. Leopold B. Felsen Award for Excellence in Electrodynamics (International)
6. IEEE AP-S Student Paper Competition Honorable Mention (International)

Projects

1. Efficient Scattering Analysis Tool for Airborne Missiles (ESATAM), ROKETSAN, Industrial Project (National)
2. Fast and Accurate RCS Analysis Software Development (FARAD), TAI, Industrial Project (National)
3. Accurate Electromagnetic Analysis and Optimizations of Photonic Crystals Involving Dielectric Rods (DEMOS), TUBITAK (National)
4. Three-Dimensional Security Radar, ASELSAN, Industrial Project (National)
5. Design of X-Band IMUX and OMUX for Satellite Communication Systems, ASELSAN, Industrial Project (National)
6. Design, Simulation and Fabrication of Reconfigurable Paper-Based Inkjet Antennas for Radio-Frequency-Identification Applications, TUBITAK (National)
7. Realistic, Fast, and Accurate Simulations of Optical Metamaterials (OMeGA), TUBITAK (National)
8. Design and Fabrication of Inkjet Antennas for Radio Frequency Identification Applications, TUBITAK (National)
9. Simulations of Microwave Systems for Reliable Diagnosis of Breast Cancer, Middle East Technical University (Institutional)
10. Overcoming Low-Frequency Breakdowns in Numerical Solutions of Electromagnetics Problems (EPSilON), TUBITAK (National)

Scientific Interests

Electromagnetic scattering and radiation, fast algorithms, parallelization, high-performance computing, iterative methods, hybrid integral formulations, broadband solvers, optimization algorithms, metamaterials, plasmonic materials, learning algorithms, deep

learning.

PUBLICATIONS

Book Chapters

1. H. Aykut Şatana B. Karaosmanoğlu, and Ö. Ergül, "A comparative study of nanowire arrays for maximum power transmission," in *Nanowires*, K. Maaz, Ed. InTech, 2017.
2. A. Çekinmez, B. Karaosmanoğlu, and Ö. Ergül, "Integral-equation formulations of plasmonic problems in the visible spectrum and beyond," in *Dynamical Systems - Analytical and Computational Techniques*, M. Reyhanoglu, Ed. InTech, 2017.

Journal Papers

1. B. Karaosmanoğlu and Ö. Ergül, "Visual Result Prediction in Electromagnetic Simulations Using Machine Learning," *IEEE Antennas Wireless Propag. Lett.*, vol. 18, pp. 2264–2266, 2019.
2. B. Karaosmanoğlu and Ö. Ergül, "Modified combined tangential formulation for stable and accurate analysis of plasmonic structures," *ACES Exp.*, vol. 34, no. 5, pp. 811–814, May 2019.
3. B. Karaosmanoğlu, E. Tuygar, U. Topçuoğlu, and Ö. Ergül, "Improving the efficiency of solar cells using antenna-inspired cavities," *Microw. Opt. Technol. Lett.*, vol. 61, no. 8, pp. 1924–1930, Aug. 2019.
4. B. Karaosmanoğlu, H. Eray, and Ö. Ergül, "Full-wave optimization of three-dimensional photonic-crystal structures involving dielectric rods," in *J. Opt. Soc. Am. A.*, vol. 37, no. 7, 1103–1113, Jul. 2018.
5. Ş. Yazar, C. G. Sür, B. Solak, Ö. Eroğlu, A. Altınoklu, S. Güler, U. M. Gür, B. Karaosmanoğlu, and Ö. Ergül, "Efficient and accurate electromagnetic analysis of three-dimensional nano-optical structures," in *Materials Science Forum*, vol. 915, pp. 202–206, Mar. 2018.
6. H. İbili, B. Karaosmanoğlu, and Ö. Ergül, "Demonstration of negative refractive index with low-cost inkjet-printed microwave metamaterials," *Microw. Opt. Technol.*

Lett., vol. 60, no. 1, pp. 187–191, Jan. 2018.

7. F. Mutlu, C. Önol, B. Karaosmanoğlu, and Ö. Ergül, "Inkjet-printed cage-dipole antennas for radio-frequency applications," *IET Microwaves, Antennas & Propagation*, vol. 11, no. 14, pp. 2016–2020, Nov. 2017.

8. B. Karaosmanoğlu, S. Küçük and Ö. Ergül, "Fine-tuning snowflake fractal antennas," *Int. J. Numer. Model. Electron.*, no. e2212, Jan. 2017.

9. Y. E. Tunçyürek, B. Karaosmanoğlu, and Ö. Ergül, "Computational design of optical couplers for bended nanowire transmission lines" *ACES J.*, vol. 32, no. 7, pp. 562–568, Jul. 2017.

10. B. Karaosmanoğlu, A. Yılmaz, and Ö. Ergül, "Accurate and efficient analysis of plasmonic structures using surface integral equations," *IEEE Trans. Antennas Propag.*, vol. 65, no. 6, pp. 3049–3057, Jun. 2017.

11. B. Karaosmanoğlu and Ö. Ergül, "Generalized hybrid surface integral equations for finite periodic perfectly conducting objects," *IEEE Antennas Wireless Propag. Lett.*, vol. 16, pp. 1068–1071, 2017.

12. B. Karaosmanoğlu and Ö. Ergül, "EFIE-tuned testing functions for MFIE and CFIE" *IEEE Antennas Wireless Propag. Lett.*, vol. 16, pp. 968–970, 2017.

13. B. Karaosmanoğlu, A. Altınoklu, and Ö. Ergül, "Electromagnetic optimizations of corrugated metallic sheets for maximum power focusing," *J. Electromagn. Waves Appl.*, vol. 31, no. 8, 837–849, Apr. 2017.

14. S. Güler, B. Karaosmanoğlu, and Ö. Ergül, "Design, simulation, and fabrication of a novel type of inkjet-printed pixel antennas," *PIER Lett.*, vol. 64, pp. 51–55, 2016.

15. B. Karaosmanoğlu, A. Altınoklu, and Ö. Ergül, "Numerical constructions of testing functions for improving the accuracy of MFIE and CFIE," *Prog. Electromagn. Res. M.*, vol. 51, pp. 63–70, Oct. 2016.

16. B. Karaosmanoğlu, A. Yılmaz, U. M. Gür, and Ö. Ergül, "Solutions of plasmonic structures using the multilevel fast multipole algorithm," *Special Issue on Challenges in RF and Microwave Defense Engineering, Int. J. RF Microwave Comput.-Aided. Eng.*, vol. 51, no. 7, pp. 1094–1108, May. 2016.

17. C. Önol, B. Karaosmanoğlu, and Ö. Ergül, "Efficient and accurate electromagnetic optimizations based on approximate forms of the multilevel fast multipole algorithm," *IEEE Antennas Wireless Propag. Lett.*, vol. 15, pp. 1113–1115, Apr. 2016.

18. Ö. Ergül, and B. Karaosmanoğlu, "Broadband Multilevel Fast Multipole Al-

gorithm Based on an Approximate Diagonalization of the Green's Function," *IEEE Trans. Antennas Propagat.*, vol. 63, no. 7, pp. 3035–3041, Jul. 2015.
19. A. Yılmaz, B. Karaosmanoğlu, and Ö. Ergül, "Computational electromagnetic analysis of deformed nanowires using the multilevel fast multipole algorithm," *Sci. Rep.*, vol. 5, no. 8469, Feb. 2015.
20. Ö. Ergül, and B. Karaosmanoğlu, "Approximate stable diagonalization of the Green's function for low frequencies,"*IEEE Antennas Wireless Propag. Lett.*, vol. 13, pp. 1054–1056, 2014.
21. Ö. Ergül, and B. Karaosmanoğlu, "Low-frequency fast multipole method based on multiple-precision arithmetic,"*IEEE Antennas Wireless Propag. Lett.*, vol. 13, pp. 975–978, 2014.

Submitted Journal Papers

1. B. Karaosmanoğlu and Ö. Ergül, "Acceleration of MLFMA Simulations Using Trimmed TreeStructures," *IEEE Trans. Antennas Propag.*, submitted.

International Conference Publications

1. Y. Koyaz, H. İbili, B. Karaosmanoğlu, and Ö. Ergül, "Analysis of composite structures involving near-zero-index materials," in *in Proc. Int. Conf. on. Microwaves, Communications, Antennas, and Electronic Systems (IEEE COMCAS)*, 2019.
2. B. Karaosmanoğlu, Y. Koyaz, H. İbili, and Ö. Ergül, "Fast and accurate analysis of three-dimensional structures involving near-zero-index materials," in *in Proc. Int. Conf. on Electromagnetics in Advanced Applications (ICEAA)*, 2019.
3. B. Karaosmanoğlu, U. Özmü, and Ö. Ergül, "Novel SIE formulations for accurate and stable analysis of near-zero-index materials," in *in Proc. IEEE Antennas and Propagation Soc. Int. Symp.*, 2019.
4. B. Karaosmanoğlu, B. N. Bice, and Ö. Ergül, "Geometric improvements on solar cells for reducing reflections," in *in Proc. IEEE Antennas and Propagation Soc. Int. Symp.*, 2019.
5. B. Karaosmanoğlu, and Ö. Ergül, "Error prediction in electromagnetic simula-

tions using machine learning," in *in Proc. IEEE Antennas and Propagation Soc. Int. Symp.*, 2019.

6. H. İbili, Y. Koyaz, U. Özmü, B. Karaosmanoğlu, and Ö. Ergül, "Novel SIE implementations for efficient and accurate electromagnetic simulations of zero-index materials," in *in Proc. Progress in Electromagnetics Research Symp. (PIERS)*, 2019.

7. M. Tonga, B. Karaosmanoğlu, and Ö. Ergül, "A broadband electromagnetic solver based on multiscale MLFMA and hybrid integral equations," in *Proc. Mediterranean Microwave Symp. (MMS)*, 2018, pp. 97–100.

8. H. İbili, B. Karaosmanoğlu, and Ö. Ergül, "Homogenization of microwave metamaterial structures using full-wave solutions and genetic algorithms," in *Proc. Mediterranean Microwave Symp. (MMS)*, 2018, pp. 244–246.

9. U. M. Gür, İ. C. Çetin, B. Karaosmanoğlu, and Ö. Ergül, "PIE-MLFMA implementation for solving complex subwavelength electromagnetic problems," in *Proc. IEEE MTT-S Int. Conf. Numerical Electromagnetic and Multiphysics Modeling and Optimization (NEMO)*, 2018.

10. B. Karaosmanoğlu, U. Topçuoğlu, S Güler, E. Tuygar, and Ö. Ergül, "Optimal cavities to enhance freespace matching in solar cells," in *Proc. Progress in Electromagnetics Research Symp. (PIERS)*, 2018.

11. H. İbili, S Güler, B. Karaosmanoğlu, and Ö. Ergül, "Penetrable numerical modeling of metallic nanoparticles at terahertz frequencies," in *Proc. Progress in Electromagnetics Research Symp. (PIERS)*, 2018.

12. B. Karaosmanoğlu, Ş. Yazar, and Ö. Ergül, "Design of compact nano-optical couplers involving dielectric nanorods," in *Proc. URSI General Assembly and Scientific Symp. (URSI-GASS)*, 2018.

13. B. Karaosmanoğlu, U. Topçuoğlu, E. Tuygar, and Ö. Ergül, "Numerical investigation of nanocavities for optimal power absorption in solar cells," in *Proc. URSI General Assembly and Scientific Symp. (URSI-GASS)*, 2018.

14. H. Eray, B. Karaosmanoğlu, and Ö. Ergül, "Full-wave electromagnetic optimizations of photonic crystals involving dielectric rods," in *Proc. Progress in Electromagnetics Research Symp. (PIERS)*, 2017.

15. U. M. Gür, B. Karaosmanoğlu, and Ö. Ergül, "Solutions of new potential integral equations using approximate stable diagonalization of the Green?s function," in *Proc. Int. Conf. on Electromagnetics in Advanced Applications (ICEAA)*, 2017, pp.

1894–1897.

16. U. M. Gür, B. Karaosmanoğlu, and Ö. Ergül, "Fast-multipole-method solutions of new potential integral equations," in *Proc. Fourth International EMC Conference*, 2017.

17. H. İbili, B. Karaosmanoğlu, and Ö. Ergül, "Design and fabrication of low-cost inkjet printed metamaterials," in *Proc. Fourth International EMC Conference*, 2017.

18. B. Karaosmanoğlu, H. A. Şatana and Ö. Ergül, "Investigation of alternative array configurations of nanowires for maximum power transmission at optical frequencies," in *Proc. IEEE Antennas and Propagation Soc. Int. Symp.*, 2017.

19. B. Karaosmanoğlu and Ö. Ergül, "Accuracy of the surface integral-equation formulations for large negative permittivity values," in *Proc. Progress in Electromagnetics Research Symp. (PIERS)*, 2017.

20. B. Karaosmanoğlu and Ö. Ergül, "Modified combined tangential formulation for stable and ac- curate analysis of plasmonic structures," in *Proc. Int. Applied Computational Electromagnetics Soc. Symp.*, 2017.

21. C. Önol, A. Üçünü, B. Karaosmanoğlu, and Ö. Ergül, "Nested iterative solutions of electromagnetic problems using approximate forms of the multilevel fast multipole algorithm," in *Proc. European Conf. on Antennas and Propagation (EuCAP)*, 2017.

22. B. Karaosmanoğlu, S. Güler, H. İbili, and Ö. Ergül, "Inkjet-printed pixel antennas with hexagonal cells," in *Proc. European Conf. on Antennas and Propagation (EuCAP)*, 2017.

23. B. Karaosmanoğlu, A. Yılmaz, and Ö. Ergül, "Development and application of a broadband multilevel fast multipole algorithm for challenging multiscale problems," in *Proc. Progress in Electromagnetics Research Symp. (PIERS)*, 2016.

24. B. Karaosmanoğlu, A. Yılmaz, and Ö. Ergül, "On the accuracy and efficiency of surface formula- tions in fast analysis of plasmonic structures via MLFMA," in *Proc. Progress in Electromagnetics Research Symp. (PIERS)*, 2016.

25. B. Karaosmanoğlu, C. Önol, S. Güler, A. Altınoklu, and Ö. Ergül, "Full-wave electromagnetic optimizations using surface integral equations and the multilevel fast multipole algorithm," in *Proc. Progress in Electromagnetics Research Symp. (PIERS)*, 2016.

26. A. Yılmaz, B. Karaosmanoğlu, and Ö. Ergül, "Analysis of optical properties of nanowires using surface integral equations and the multilevel fast multipole algo-

rithm," in *Proc. Advanced Electromagnetic Symp.*, 2016.

27. Ö. Ergül, B. Karaosmanoğlu, M. Takrimi, and V. B. Erturk, "Broadband multilevel fast multipole algorithm for large-scale problems with nonuniform discretizations," in *Proc. Int. Symp. on Electromagnetic Theory (EMTS)*, 2016.

28. A. Altınoklu, B. Karaosmanoğlu, and Ö. Ergül, "Full-wave electromagnetic optimizations of corrugated metallic sheets," in *Proc. IEEE Antennas and Propagation Soc. Int. Symp.*, 2016.

29. B. Karaosmanoğlu, and Ö. Ergül, "Improving the accuracy of MFIE and CFIE by using numerically designed testing functions," in *Proc. IEEE Antennas and Propagation Soc. Int. Symp.*, 2016.

30. B. Karaosmanoğlu, and Ö. Ergül, "Numerical design of testing functions for the magnetic-field integral equation," in *Proc. European Conf. on Antennas and Propagation (EuCAP)*, 2016.

31. T. Ciftci, B. Karaosmanoğlu, and Ö. Ergül, "Low-cost inkjet antennas for RFID applications [extended]," in *IoP Conference Series: Materials Science and Engineering*, 2016.

32. T. Ciftci, B. Karaosmanoğlu, and Ö. Ergül, "Low-cost inkjet antennas for RFID applications," in *Proc. IEEE Radio and Antenna Days of the Indian Ocean*, 2015.

33. B. Karaosmanoğlu, A. Yılmaz, and Ö. Ergül, "Full-wave analysis of three-dimensional optical metamaterials involving deformed nanowires," in *Proc. Int. Cong. on Advanced Electromagnetic Materials in Microwaves and Optics (Metamaterials)*, 2015, pp. 174–176.

34. Ö. Ergül, C. Önol, and B. Karaosmanoğlu, "Optimizations of EFIE and MFIE combinations in hybrid formulations of conducting bodies," in *Proc. Int. Conf. on Electromagnetics in Advanced Applications (ICEAA)*, 2015, pp. 1276–1279.

35. Ö. Ergül, and B. Karaosmanoğlu, "Broadband MLFMA based on an approximate diagonalization of the three-dimensional Green's function," in *Proc. Int. Conf. on Electromagnetics in Advanced Applications (ICEAA)*, 2015, pp. 1272–1275.

36. B. Karaosmanoğlu, A. Yılmaz, U. M. Gür, and Ö. Ergül, "Solutions of plasmonic structures using the multilevel fast multipole algorithm," in *Proc. Third International EMC Conference*, 2015.

37. Ö. Ergül, B. Karaosmanoğlu, and C. Önol, "Electromagnetic optimizations using heuristic al- gorithms combined with the ordinary and approximate forms of the

multilevel fast multipole algorithm," in *Proc. Int. Conf. on Matrix Methods in Mathematics and Applications (MMMA)*, 2015, pp. 37–38.

38. B. Karaosmanoğlu, and Ö. Ergül, "Hybrid surface integral equations for optimal analysis of perfectly conducting bodies," in *Proc. IEEE Antennas and Propagation Soc. Int. Symp.*, 2015, pp. 1160–1161.

39. C. Önol, B. Karaosmanoğlu, and Ö. Ergül, "Antenna switch optimizations using genetic algo- rithms accelerated with the multilevel fast multipole algorithm," in *Proc. IEEE Antennas and Propagation Soc. Int. Symp.*, 2015, pp. 1338–1339.

40. C. Önol, T. Ciftci, S. Kucuk, B. Karaosmanoğlu, and Ö. Ergül, "Design, simulation, and fab- rication of low-cost inkjet antennas," in *Proc. Progress in Electromagnetics Research Symp. (PIERS)*, 2015, pp. 2829–2833.

41. B. Karaosmanoğlu, U. M. Gür, and Ö. Ergül, "Investigation of nanoantennas using surface integral equations and the multilevel fast multipole algorithm," in *Proc. Progress in Electromagnetics Research Symp. (PIERS)*, 2015, pp. 2026–2030.

42. B. Karaosmanoğlu, A. Yılmaz, and Ö. Ergül, "Rigorous analysis of deformed nanowires using the multilevel fast multipole algorithm," in *Proc. European Conf. on Antennas and Propagation (EuCAP)*, 2015.

43. Ö. Ergül, and B. Karaosmanoğlu, "Using multiple-precision arithmetic to prevent low-frequency breakdowns in the diagonalization of the Green's function," in *Proc. Progress in Electromagnetics Research Symp. (PIERS)*, 2014, pp. 2311–2315.

44. Ö. Ergül, and B. Karaosmanoğlu, "Low-frequency multilevel fast multipole algorithm using an approximate diagonalization of the Green's function," in *Proc. XXXI URSI General Assembly and Scientific Symp. of Int. Union of Radio Science*, 2014.

45. Ö. Ergül, and B. Karaosmanoğlu, "Stabilization of the fast multipole method for low frequencies using multiple-precision arithmetic," in *Proc. XXXI URSI General Assembly and Scientific Symp. of Int. Union of Radio Science*, 2014.

Conference Abstracts

1. C. G. Sür, B. Solak, Ö. Eroğlu, Ş. Yazar, A. Altınoklu, S. Güler, U. M. Gür, B. Karaosmanoğlu, and Ö. Ergül, "Efficient and accurate analysis of three-dimensional nano-optical structures: frequency-selective surfaces, metamaterials, nanoantennas,

nanowires, and photonic crystals," in *10th Japanese-Mediterranean Workshop on Applied Electromagnetic Engineering for Magnetic, Superconducting, Multifunctional and Nanomaterials (JAPMED)*, Jul. 2017.

2. B. Karaosmanoğlu, T. Ciftci, and Ö. Ergül, "Challenges in low-cost inkjet antennas," in *IEEE Antennas and Propagation Soc. Int. Symp.*, Vancouver, BC, Canada, Jul. 2015, p. 181.

3. B. Karaosmanoğlu, and Ö. Ergül, "Broadband implementation of MLFMA using approximate scaled diagonalization of the Green's function," in *URSI Atlantic Radio Science Conf. (URSI AT-RASC)*, Gran Canaria, Canary Islands, May 2015.

National Conference Papers

1. B. Karaosmanoğlu, Ş. Yazar, and Ö. Ergül, "Design of optical couplers via optimization of photonic crystal structures," in Turkish, *URSI-Turkey Scientific Symp.*, 2018.

2. B. Karaosmanoğlu, H. İbili, and Ö. Ergül, "Homogenization of structures with negative permeability using genetic algorithms," in Turkish, *URSI-Turkey Scientific Symp.*, 2018.

3. B. Karaosmanoğlu, H. İbili, S Güler, and Ö. Ergül, "Accurate solutions of electromagnetic problems involving very large targets," in Turkish, *9th Congress of Defense Technologies*, 2018, pp. 913–917. F. Mutlu, B. Karaosmanoğlu, and Ö. Ergül, "Design and measurement of inkjet-printed antennas for radio-frequency-identification applications," in Turkish, *URSI-Turkey Scientific Symp.*, 2016.

4. B. Karaosmanoğlu and Ö. Ergül, "Design of numerical testing functions for the magnetic-field integral equation," in Turkish, *URSI-Turkey Scientific Symp.*, 2016.

5. B. Karaosmanoğlu, H. İbili, and Ö. Ergül, "Design and fabrication of low-cost metamaterials via inkjet printing technique," in Turkish, *URSI-Turkey Scientific Symp.*, 2016.

6. B. Karaosmanoğlu, A. Yılmaz, and Ö. Ergül, "Accurate full-wave simulations of nanowires at optical frequencies using the multilevel fast multipole algorithm," in Turkish, *Nanoscience & Nanotechnology Conf. (NanoTR)*, Ankara, Turkey, 2015.

7. F. A. Tunç, F. Gökçe, C. Önol, B. Karaosmanoğlu, and Ö. Ergül, "Design and

simulations of inkjet-type antennas suitable for printing on paper" in Turkish, *URSI-Turkey Scientific Symp.*, 2014.
8. B. Karaosmanoğlu, and Ö. Ergül, "A broadband multilevel fast multipole algorithm based on the scaled diagonalization of the Green's function," in Turkish, *URSI-Turkey Scientific Symp.*, 2014.
9. B. Karaosmanoğlu, U. M. Gür, and Ö. Ergül, "Accurate analysis of nanoantennas with plasmonic properties using surface integral equations," in Turkish, *URSI-Turkey Scientific Symp.*, 2014.
10. B. Karaosmanoğlu, A. Yılmaz, and Ö. Ergül, "Fast and accurate analysis of nanowires with the multilevel fast multipole algorithm," in Turkish, *URSI-Turkey Scientific Symp.*, 2014.

National Conference Abstracts

1. B. Karaosmanoğlu and Ö. Ergül, "Computational electromagnetic simulations of electrically large structures," in *Workshop on Computational Science and Engineering*, 2018.

URSI-Bulletin Contributions

1. H. İbili, B. Karaosmanoğlu, and Ö. Ergül, "SOLBOX-12," in *Radio Science Bulletin*, vol. 90, no. 2, pp. 43–47, Jun. 2018.
2. B. Karaosmanoğlu, M. Tonga, and Ö. Ergül, "SOLBOX-11," in *Radio Science Bulletin*, vol. 90, no. 2, pp. 69–74, Mar. 2018.
3. Ş. Yazar, B. Karaosmanoğlu, and Ö. Ergül, "SOLBOX-07," in *Radio Science Bulletin*, vol. 90, no. 2, pp. 71–74, Jun. 2017.
4. B. Karaosmanoğlu and Ö. Ergül, "SOLBOX-05," in *Radio Science Bulletin*, vol. 89, no. 4, pp. 43–45, Dec. 2016.
5. B. Karaosmanoğlu, A. Yılmaz, and Ö. Ergül, "SOLBOX-01," in *Radio Science Bulletin*, vol. 88, no. 2, pp. 33–36, Jun. 2015.